

**COLLECTIVE CELL MIGRATION IN SINGLE AND
DUAL CELL LAYERS**

by

Tracy L. Stepien

B.S., Mathematics, University at Buffalo, The State University of
New York, 2008

M.A., Mathematics, University of Pittsburgh, 2010

Submitted to the Graduate Faculty of
the Dietrich School of Arts & Sciences Department of Mathematics

in partial fulfillment

of the requirements for the degree of

Doctor of Philosophy

University of Pittsburgh

2013

UNIVERSITY OF PITTSBURGH
DIETRICH SCHOOL OF ARTS & SCIENCES

This dissertation was presented

by

Tracy L. Stepien

It was defended on

May 24, 2013

and approved by

David Swigon, PhD, Associate Professor, Department of Mathematics

G. Bard Ermentrout, PhD, Professor, Department of Mathematics

Ivan Yotov, PhD, Professor, Department of Mathematics

Lance A. Davidson, PhD, Associate Professor, Departments of Bioengineering and

Developmental Biology

Dissertation Director: David Swigon, PhD, Associate Professor, Department of

Mathematics

COLLECTIVE CELL MIGRATION IN SINGLE AND DUAL CELL LAYERS

Tracy L. Stepien, PhD

University of Pittsburgh, 2013

Collective cell migration plays a substantial role in maintaining the cohesion of epithelial cell layers, in wound healing, and in embryonic development. We extend a previously developed one-dimensional continuum mechanical model of cell layer migration based on an assumption of elastic deformation of the cell layer to incorporate stretch-dependent proliferation, which leads to a generalized Stefan problem for the density of the layer. The resulting partial differential equation system is solved numerically using an adaptive finite difference method and similarity solutions are studied analytically. We show the existence of traveling wave solutions with constant wave speed for a large class of constitutive equations for the dependence of proliferation on stretch.

We then extend the corresponding two-dimensional model of cell migration to incorporate two adhering cell layers. A numerical method to solve the model equations is based on a level set method for free boundary problems with a domain decomposition method to account for where the migrating cells in each layer are located. We apply the model to experimental migration of epithelial and mesenchymal cell layers during gastrulation, an early phase of development, in animal cap explants of *Xenopus laevis* embryos to analyze the mechanical properties of each cell layer. Understanding the mechanics of collective cell migration during embryonic development will aid in developing tools to perturb pathological cases such as during wound healing and to aid in the prediction and early detection of birth defects.

Keywords: cell migration, wound healing, embryology, mathematical modeling, elastic continuum, free boundary problem, traveling wave solutions.

TABLE OF CONTENTS

PREFACE	xi
1.0 INTRODUCTION	1
1.1 BIOLOGICAL MOTIVATION	3
1.1.1 Necrotizing Enterocolitis	3
1.1.2 Birth Defects	4
1.2 PREVIOUS MATHEMATICAL MODELS	5
2.0 1-D SINGLE LAYER CELL MIGRATION MODEL	8
2.1 DERIVATION OF MATERIAL FORMULATION	8
2.2 DERIVATION OF SPATIAL FORMULATION	14
2.3 EQUIVALENCE OF MODELS	18
2.3.1 Governing Equations and Elasticity Functions	18
2.3.2 Cell Proliferation Functions	20
2.3.3 Growth Gradient	21
2.3.4 Initial and Boundary Conditions	22
3.0 NUMERICAL SOLUTIONS OF 1-D SINGLE LAYER MODEL	23
3.1 ADAPTIVE FINITE DIFFERENCE METHOD	28
3.1.1 Analysis of the Numerical Method	32
3.1.1.1 Consistency	32
3.1.1.2 Stability	34
3.1.1.3 Convergence	38
3.2 TRANSVERSE METHOD OF LINES METHOD	39
4.0 ANALYTIC SOLUTIONS OF 1-D SINGLE LAYER MODEL	43

4.1	SIMILARITY SOLUTIONS FOR MODEL WITHOUT GROWTH	43
4.1.1	Spatial Formulation	43
4.1.2	Material Formulation	45
4.2	TRAVELING WAVE SOLUTIONS FOR MODEL WITH GROWTH	47
4.2.1	Stationary Waves	49
4.2.2	Traveling Waves	51
4.2.3	Stability of Traveling Waves	63
4.2.3.1	Material Formulation to Spatial Formulation	64
4.2.3.2	Spatial Formulation to Material Formulation	65
5.0	2-D DUAL LAYER CELL MIGRATION MODEL	71
5.1	DERIVATION OF MODEL EQUATIONS	71
6.0	NUMERICAL SOLUTIONS OF 2-D DUAL LAYER MODEL	78
6.1	LEVEL SET METHOD	92
6.1.1	Analysis of the Numerical Method	99
7.0	ESTIMATING MODEL PARAMETERS FROM EXPERIMENTAL DATA	103
7.1	EXPERIMENTAL SETUP	103
7.2	PARAMETER OPTIMIZATION METHOD	104
7.3	RESULTS	108
8.0	DISCUSSION	118
	BIBLIOGRAPHY	122

LIST OF TABLES

4.1	Speed of the leading edge	63
6.1	Relative change in area of the 2-D dual layer numerical solutions for varying initial geometries	83
6.2	Relative difference in area of the 2-D dual layer numerical solutions for varying parameters	92
6.3	Examples of level set functions	94
6.4	Elapsed CPU time for numerical solutions of the 2-D dual layer model for varying mesh sizes	100

LIST OF FIGURES

2.1 Schematic representation of a single cell layer as a 1-D continuum	9
2.2 Resultant forces and growth functions	11
2.3 Material vs. spatial coordinates	19
3.1 Numerical solution of the 1-D single layer model: no growth	24
3.2 Numerical solution of the 1-D single layer model: linear growth	25
3.3 Numerical solution of the 1-D single layer model: Fisher growth	26
3.4 Numerical solution of the 1-D single layer model: cubic growth	27
3.5 Stability of numerical method for the 1-D single layer model	37
3.6 Comparison of the transverse method of lines and nonadaptive finite difference methods	42
4.1 Similarity solution under scaling of the material formulation with no growth .	47
4.2 Stationary wave solutions of the spatial formulation with growth	50
4.3 The set W_c	52
4.4 Traveling waves: linear growth	53
4.5 Bifurcation diagram: linear growth	54
4.6 Traveling waves: cubic growth	56
4.7 Bifurcation diagram: cubic growth	57
4.8 Traveling waves: a three root growth function	59
4.9 Bifurcation diagram: a three root growth function	60
4.10 Bifurcation diagram: another three root growth function	60
4.11 Traveling waves: another three root growth function, limiting density = 1 . .	61
4.12 Traveling waves: another three root growth function, limiting density = 1/8 .	62

4.13 Stability of traveling waves – material to spatial formulation	64
4.14 Stability of traveling waves – spatial to material formulation: linear and Fisher growth	65
4.15 Stability of traveling waves – spatial to material formulation: cubic growth	66
4.16 Stability of traveling waves – spatial to material formulation: a three root growth function	67
4.17 Stability of traveling waves – spatial to material formulation: another three root growth function, limiting density = 1	68
4.18 Stability of traveling waves – spatial to material formulation: another three root growth function, limiting density = 1/8	69
5.1 Schematic representation of the 2-D dual layer problem	74
6.1 Numerical solution of the 2-D dual layer model: circles, ellipses, and an annulus and circle	79
6.2 Numerical solution of the 2-D dual layer model: two separated circles, two small circles inside a large circle, and rectangles	80
6.3 Numerical solution of the 2-D dual layer model: diamond and square, astroids, and roses	81
6.4 Average instantaneous normal velocity of the edge and area of the 2-D dual layer numerical solutions	82
6.5 Numerical solution of the 2-D dual layer model for varying parameters (control case)	84
6.6 Numerical solution of the 2-D dual layer model for varying parameters (F_1)	85
6.7 Numerical solution of the 2-D dual layer model for varying parameters (F_2)	87
6.8 Numerical solution of the 2-D dual layer model for varying parameters (k_1)	88
6.9 Numerical solution of the 2-D dual layer model for varying parameters (k_2)	89
6.10 Numerical solution of the 2-D dual layer model for varying parameters (b_1)	90
6.11 Numerical solution of the 2-D dual layer model for varying parameters (b_2)	91
6.12 Domain decomposition of the 2-D dual layer problem	98
6.13 Numerical solution of the 2-D dual layer model for varying mesh sizes (25×25 , 50×50 , 100×100)	101

6.14 Numerical solution of the 2-D dual layer model for varying mesh sizes (200×200 , 400×400 , 700×700)	102
7.1 Model and experiment comparison: epithelial layer only	110
7.2 Model and experiment comparison: epithelial layer only	111
7.3 Model and experiment comparison: mesenchymal layer only	112
7.4 Model and experiment comparison: mesenchymal layer only	113
7.5 Model and experiment comparison: epithelial and mesenchymal layers	114
7.6 Model and experiment comparison: epithelial and mesenchymal layers	115

LIST OF MODELS

1	Material Formulation of 1-D Single Layer Cell Migration	13
2	Spatial Formulation of 1-D Single Layer Cell Migration	16
3	2-D Dual Layer Cell Migration	75

PREFACE

This work was supported in part by an Andrew Mellon Predoctoral Fellowship and the National Science Foundation through grant EMSW21-RTG 0739261.

There are many people I would like to thank for their support and encouragement throughout the years. First and foremost, my advisor David, for guiding me through my PhD and allowing me to travel around the country and the world (especially to Poland!) to share my research and become involved with the mathematical biology community. I also could not have asked for a better committee and I would like to express my appreciation for all their help. Thank you Bard, for sharing your knowledge (and math jokes!); Ivan, for teaching and assisting me with numerics; and Lance, for welcoming me into your lab and introducing me to current issues in developmental biology.

Going back many years, I would like to thank Matt Williams, Patrick Haines, Brian Kesel, and Rob Busch for instilling in me the desire to study mathematics, biology, and physics. Your enthusiasm helped fuel my interest in science and I can only hope to inspire others a fraction of the amount that you inspired me.

I am indebted to Brian Spencer for introducing me to applied mathematics research, Scott Stevens (as well as Joe Previte and Mike Rutter) for introducing me to mathematical biology research, and Bruce Pitman for being the best research advisor an undergraduate could ask for. I am very lucky to have worked on a senior project with Bruce and to have had his long-distance support through the ups and downs of graduate school.

There are a number of people that require profuse gratitude for their help with various parts of this dissertation. Julia Arciero, for assisting with the level set method as well as other mentoring; Qi Mi, for playing a role in introducing me to the project; Mike Sussman, for pointing out a better discretization for the adaptive finite difference method; Nick Hurl, for

helping with the analysis of the adaptive finite difference method; Holley Lynch, for providing batch programs for processing experimental images (saving me a lot of time); Steve Trier and Melis Hazar for providing the experimental time-lapse images examined in this dissertation, and Joe Shawky and Deepthi Vijayraghavan for providing other experimental data. I would also like to acknowledge Al Clark's DynPac Mathematica Package which was used to create the phase portrait figures.

I have a lot of wonderful memories from times I spent with friends over the years. I would especially like to acknowledge two of my best friends who were there through the thick and thin of it all, Matt Wheeler and Katie Smolnycki. Also, thank you to the other team owners in my league for being good sports when my fantasy team completely dominated this season (thank you Adrian, Peyton, Alfred, Stevan, LeSean, Bryce, and Sebastian!).

Last, but certainly not least, I owe an immense amount of gratitude to my parents, Pamela and Francis Stepien. You have been there for me always, allowed me to enrich my life with opportunities, and supported me no matter what. I am truly blessed to have you as my parents.

I dedicate my dissertation in loving memory of my grandparents, Margaret and Howard Kranz. I owe a lot to both of you for helping shape me into who I am today.

1.0 INTRODUCTION

Beginning momentarily after we are conceived through to our final days, cells migrate within our bodies. Near the beginning of embryonic development, cells migrate to form the germ layers of the embryo, the ectoderm, mesoderm and endoderm. These layers eventually form into tissues and organs, which are shaped and vascularized through cell migration. Our immune systems rely heavily on cell migration daily. Leukocytes such as macrophages and neutrophils migrate to locations of infection and epithelial cells close gaps during wound healing. Migration also plays a significant role in the progression of many diseases including cancer, arthritis, osteoporosis, atherosclerosis, mental retardation, and multiple sclerosis (Ridley et al. [56], Rørth [57], Trinkaus [75]).

Much work has been done to study how cells move on an individual basis, see for example the review papers by Ridley et al. [56] and Van Haastert and Devreotes [77] and references therein. To migrate, an individual cell first morphologically polarizes so that there is a clear distinction between the cell front and the cell rear. Then, lamellipodia or filopodia protrude from the cell and attach to the substrate. Following this, the cell body is translocated forward. Lastly, the cell rear is detached and the cycle continues (Lauffenburger and Horwitz [38], Mogilner [44]).

Another principal mode of migration is collective cell migration, which is the migration of cells in loosely or closely associated groups (Friedl and Gilmour [20], Rørth [57]). Cells remain physically and functionally connected to one another as they move via adherens junction proteins (including cadherins), desmosomal proteins, integrins, tight junctions, and gap junctions (Ilina and Friedl [31]). The features of collective migration include those of individual migrating cells with the effects of the entire group of cells, so the movement of one cell moving collectively depends on the behavior of itself and of the cells in its cohort.

For example, if a mechanical force is applied locally to the cadherins on a cell that normally moves collectively, polarized lamellipodia are formed and migration is persistent, typical of individually moving cells (Weber et al. [81]). Many epithelial tissues move collectively as a sheet of cells, including during wound healing and during embryonic development.

There are many factors that influence the speed of migrating cells which includes the surrounding cells and environment. The stiffer the substrate on top of which cells are located, the larger the traction forces, cell spreading area, and sizes of focal adhesions (Ghibaudo et al. [25]). Furthermore, cells migrate in the direction of the stiffest parts of anisotropic substrates. Cell speed also depends on the substrate extracellular matrix concentration, expression of cell integrins, and the affinity of integrin–ligand binding (Palecek et al. [51]). The dependence of cell speed on cell–substrate adhesiveness is biphasic such that there is an optimal adhesiveness for maximizing speed. In wound closure, cell proliferation does not contribute to the closure of gaps; rather, damaged cells are replaced in part to restore the original cell layer density (Farooqui and Fenteany [16]).

There has been a lot of discussion over the past hundred years regarding how cells near the edge of a migrating group, termed “leader” cells, move compared to how cells in the interior, termed “follower” cells, move. Do the leader cells actively pull along the passively moving follower cells? Do the follower cells move actively too? Is there another mechanism responsible for the motion? Vitorino and Meyer [78] found that while the morphological polarization of cells to initiate migration is dependent on growth factor signals, migration several cell diameters away from the moving edge is not dependent on these signals. The leader cells distinctively form lamellipodia and have directed motion while it was theorized that cell–cell adhesion forces in part convert random migration of the follower cells into a coordinated directed migration response. Farooqui and Fenteany [16] observed that follower cells form lamellipodia and do actively move but their direction is not as highly correlated as for the leader cells, and the velocity of cells within a layer is inversely proportional to the distance from the edge. Trepal et al. [74] showed by direct measurement that traction forces applied by cells on the substrate arise predominately many cell rows behind the edge and extend across immense distances. “Waves” of increasing velocity and stress forces were shown to propagate from the leading edge toward the interior in Serra-Picamal et al. [61],

establishing a mechanism of long-range cell guidance. Evidence hence implies that all cells throughout a migrating group actively contribute to the movement of the group in the direction toward a gap, and mechanical coupling and chemical signaling dynamically affect the movement.

1.1 BIOLOGICAL MOTIVATION

There are two principal motivations for our studying collective cell migration, namely, necrotizing enterocolitis and birth defects.

1.1.1 Necrotizing Enterocolitis

Necrotizing enterocolitis (NEC) is an intestinal inflammatory disease that is a major cause of death in premature infants. It is the most common cause of surgical emergency in the neonatal intensive care unit, and it affects 2000–4000 newborns in the United States each year. 27–63% of these newborns require surgical intervention, but despite over three decades of research, surgical mortality associated with NEC is 20–50% (Feng et al. [17], Henry and Moss [29]).

NEC results from injury to the mucosal lining of the intestine, which leads to translocation of bacteria and endotoxins such as lipopolysaccharide (LPS) from the intestine into general circulation (Cetin et al. [10]). Injury to the intestinal lining is repaired initially via rapid migration of intestinal epithelial cells from the wound edge, termed intestinal restitution. However, LPS increases integrin function and cell–matrix adhesion, which impairs the ability of intestinal epithelial cells to migrate effectively (Cetin et al. [9], Qureshi et al. [55]). If left untreated, NEC will lead to multisystem organ failure and death from systemic sepsis, though the clinical management of infants with NEC is very challenging for doctors since the patients are small and the timing and choice of surgical procedure must be attentively decided (Anand et al. [2]). Understanding the mechanisms that govern intestinal epithelial collective cell migration is essential to gain insights into the regulation of intestinal

physiology during conditions of health and NEC.

Experiments examining epithelial cell sheet migration during wound healing often involve scratch wound assays. This technique involves allowing epithelial cells to grow to confluence, and then some cells are mechanically scraped away to form a gap which represents a wound. To study whether damage to the cells at the edge triggers movement or whether the release of spatial constraints initiates it, Block et al. [6] and Poujade et al. [53], among others, allowed cells to grow to confluence around a barrier or within a microstencil that is subsequently removed. In these types of experiments, collective cell migration is triggered as well. Scratch wound assays of intestinal epithelial cells will be the basis of our studies on single layer cell migration.

1.1.2 Birth Defects

In 2006, birth defects were the number one cause of infant deaths in the United States, affecting approximately 1 in 33 newborns (Heron et al. [30]). There are many possible causes of birth defects and it is very hard to identify which factors are primarily responsible. Studies have investigated how molecular regulatory pathways and the mechanics of embryonic development cope, or fail to cope, with variation, but these are ongoing (von Dassow and Davidson [79]). Development is a complex, multi-step process during which any number of processes can go astray, and one phase that researchers focus on is gastrulation.

Gastrulation is arguably one of the most important parts of a living being's life. This is a phase during embryonic development in which the embryo transforms from a ball of cells, termed the blastula, to a structure with a gut, termed the gastrula. This is accomplished by the coordinated migration of cells to form the endoderm, an inner layer of cells that forms the epithelial lining of the gut (which includes the pharynx, esophagus, stomach, and intestines), the ectoderm, an outer layer of cells that forms the epidermis and the nervous system (including the sensory cells of the nose, ears, and eyes), and the mesoderm, a middle layer of cells that forms embryonic connective tissue which later becomes cartilage, bone, muscles, and the vascular system (including the heart, blood vessels, and blood cells) (Alberts et al. [1]). Understanding the mechanics of collective cell migration during gastrulation will

aid in developing tools to aid in the prediction and early detection of birth defects.

Amphibians, insects, reptiles, fish, birds, and mammals have all been used as animal models for embryonic development, and in any particular species, gastrulation seems to occur in the same way in most individuals (Trinkaus [75]). The African claw-toed frog, *Xenopus laevis*, has been a research animal since 1930, so it has a well-characterized life cycle (Gurdon and Hopwood [26]). Furthermore, *Xenopus* is a vertebrate that undergoes external development, the eggs are relatively large in size (the diameter is 1–1.3mm), it is easy to obtain a large number of eggs, and the eggs are suitable for microsurgery, which are all benefits for biomedical research. John Gurdon recently won the 2012 Nobel Prize in Physiology or Medicine for his work with *Xenopus*, which indicates the frogs' immense influence. Experiments involving animal cap explants of *Xenopus* embryos will be the basis of our studies on dual layer cell migration.

1.2 PREVIOUS MATHEMATICAL MODELS

To mathematically model collective cell migration, it is appropriate to model cells as a continuum as long as the characteristic length of cell movement is much larger than the size of a cell (Callaghan et al. [7]). Many existing continuum-based models of cell migration are based on the Fisher-Kolmogorov equation

$$\frac{\partial u}{\partial t} = \mathcal{D} \frac{\partial^2 u}{\partial x^2} + \alpha u(1 - u), \quad (1.1)$$

a reaction-diffusion equation where u is a concentration, \mathcal{D} is the diffusion coefficient, and α is a growth rate (Fisher [18], Kolmogorov et al. [36]). These models assume cells move randomly, they are appropriate for non-adhering cells, and they are not based on mechanics. For example, Sherratt and Murray [65, 66] modeled the closure of epidermal wounds with two governing equations describing the conservation of cell density per unit area, which depends on cell migration, proliferation, and death, and conservation of proliferation-regulating chemical concentration, which depends on diffusion, production by cells, and decay. In this setting,

the moving edge of a cell layer is represented as a traveling wave of cell concentration, verified experimentally by Maini et al. [39, 40]. This seems natural since the Fisher-Kolmogorov equation on an infinite domain is a classic example of a problem with a traveling wave.

Other reaction-diffusion continuum models of cell migration include Dale et al. [14, 15], Javierre et al. [32], Murray [46], Murray and Oster [47], Oster et al. [50], Sheardown and Cheng [62], Sherratt [64], Tranquillo and Murray [71, 72], Tremel et al. [73], and Wearing and Sherratt [80], among others.

Free boundary formalism has been introduced in various models to account for the influence of physiological electrical fields on wound closure. Across the boundary of a wound, a physiological electric field arises due to the healed region maintaining a normal potential and the wounded region having a short-circuited potential. Gaffney et al. [23] developed a model with a free boundary which examines corneal epithelial wound healing. Chen and Friedman [12] analyzed this model to show that the equations have a unique solution, complete healing is achieved in finite time, and traveling waves exist. Later, Chen and Friedman [13] analyzed a free boundary problem that applied to tumor growth based on a model by Pettet et al. [52]. Xue et al. [82] developed a model with a free boundary problem for ischemic dermal wounds that was used to predict how ischemic conditions may impair wound closure.

In this dissertation, we will focus on the collective cell migration models of Mi et al. [43] and Arciero et al. [3], in which a single cell layer is represented by an elastic continuum capable of deformation, motion, and material growth. These models can be applied to wound healing and cell colony growth to investigate epithelial sheet migration. The model of Mi et al. [43] uses a material, or Lagrangian, coordinate system in which the reference configuration is the initial configuration, while the model of Arciero et al. [3] uses a spatial, or Eulerian, coordinate system in which the reference configuration is the current configuration. In Chapter 2, we derive both of these models in one dimension based on principles of mechanics with an assumption of stretch-dependent cell proliferation and show the equivalence between them. The main open question is to what extent different choices of constitutive functions for the elasticity and cell proliferation rate affect the motion of the cell layer and whether it is possible to determine such functions by observing that motion.

In Chapter 3, we give evidence for the existence of traveling waves based on numerical

solutions of the material formulation for a single cell layer in one dimension for various elasticity and cell proliferation rate functions. An adaptive finite difference numerical method is developed, and the consistency, stability, and convergence of the method is discussed. Another numerical method, a transverse method of lines method, is also presented.

We analyze the existence of a similarity solution under scaling in the absence of cell proliferation and the existence and uniqueness of traveling wave solutions when there is cell proliferation for a single layer in one dimension in Chapter 4. We find a familiar explicit formula for a similarity solution under scaling in the spatial formulation for one specific elasticity function, while more general elasticity functions are examined in the material formulation. We also show in Chapter 4 that for a broad class of elasticity and nonzero cell proliferation rate functions, the motion of the layer converges to a traveling wave and the velocity and shape of that wave is not particularly sensitive to those functions. We also study the stability of traveling waves using numerical solutions. The traveling wave solutions are stable if the solution trajectory in phase space does not cross the horizontal axis.

To model the migration of epithelial and mesenchymal cells during gastrulation, we extend the two-dimensional model of Arciero et al. [3] to incorporate two adhering layers of cells in Chapter 5. The resulting equations are characterized by the adhesion between the substrate and the bottom layer, the adhesion between the two layers, the stretching modulus of each layer, and the net external force of each layer. In Chapter 6, we present a level set method with a domain decomposition method to numerically solve the model equations and show results of the simulations.

In Chapter 7, model parameters for the two-dimensional dual layer cell migration model are estimated using experimental data from time-lapse images of animal cap explants of *Xenopus laevis* embryos. Our method of extracting experimental cell layer edge positions and densities is discussed along with our strategy to find optimal parameters. The parameters are used to shed light on how the mechanical properties of the layers differ when the layers are together or separated.

2.0 1-D SINGLE LAYER CELL MIGRATION MODEL

In this chapter, we derive the material and spatial formulations of a continuum mechanical model of one-dimensional movement of a single layer of cells in which the cell proliferation rate depends on stretch. We also show equivalence between the two models.

These models are based on time-lapse images of migrating small intestinal epithelial (IEC-6) cell layers provided by the Hackam Lab at the University of Pittsburgh. In the experiment, the cells were cultured on a glass coverslip, grown to confluence, and then scraped with a pipette or cell scraper to create a gap that represents a wound. The coverslip was mounted on the stage of an Olympus 1X71 (Tokyo, Japan) inverted microscope warmed to 37°C, and fresh medium was continuously perfused across the cells. Every 5 minutes, differential interference contrast images were obtained. The cell layer is one cell thick and it was observed that during migration the cells do not separate from the edge and holes were not formed in the interior.

2.1 DERIVATION OF MATERIAL FORMULATION

A continuum mechanical model for one-dimensional cell migration in material, or Lagrangian, coordinates was originally derived by Mi et al. [43], and we summarize the derivation here.

The cell layer is represented by a one-dimensional elastic continuum capable of deformation, motion, and material growth. The motion of the cell layer is assumed to be driven by the cells at the leading edge through the formation of lamellipodia (Sheetz et al. [63]). Interior cells are tightly connected to the cells at the boundary, and tight junctions prevent separation between neighboring cells (Anand et al. [2]). The cell layer stretches because of

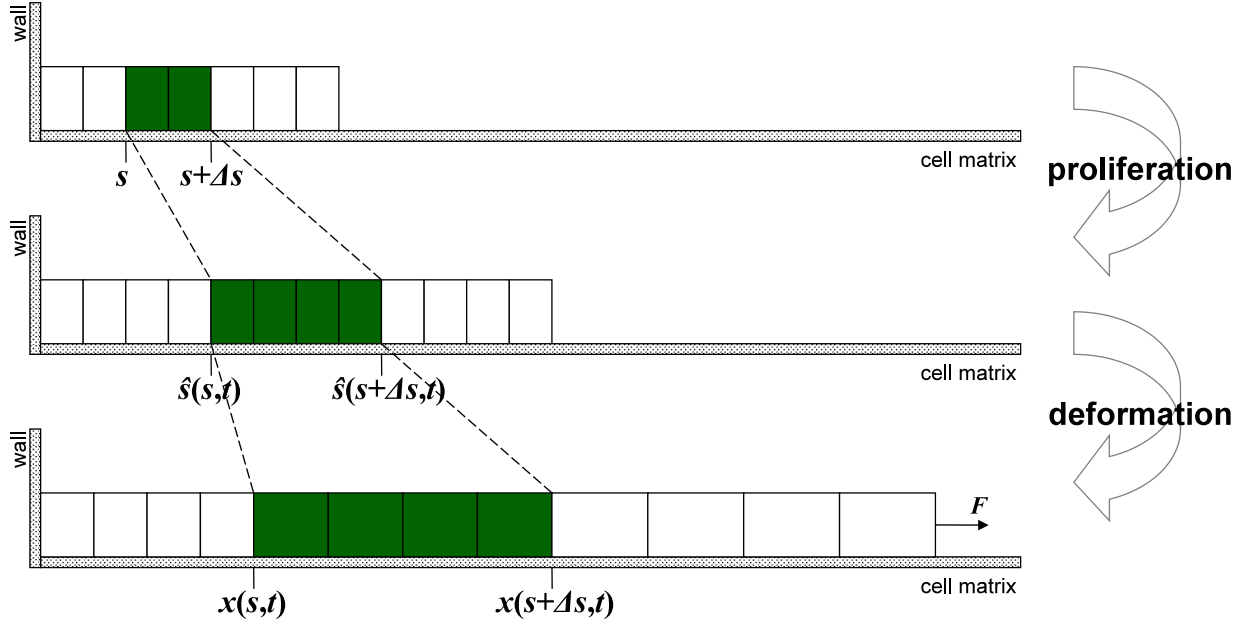


Figure 2.1: Schematic representation of a single cell layer as a 1-D continuum: (Top) Initial state, (Middle) Hypothetical state at time t accounting for proliferation but not deformation, (Bottom) True configuration of the layer at time t .

the tension applied by the edge cells, and the motion of the cells is slowed down by the adhesion between cells and the substrate.

The main interactions considered are the force of the lamellipodia, adhesion of the cell layer to the substrate, and elasticity of the cell layer. Elasticity of the substrate is ignored since the model describes in vitro scratch wound assay experiments which studied cells on glass coverslips.

The motion of cells is described using independent variable s which describes the position of a cell in the original layer and dependent variable $x(s, t)$ which describes the position of cell s at time t . The additional variable $\hat{s}(s, t)$ describes the hypothetical position of cell s at time t if all deformation in the layer was instantaneously removed, thus, $\hat{s}(s, t)$ describes purely the local growth of the layer at the position s . See Figure 2.1.

Consider a segment of cells that are the offspring of cells between s and $s + \Delta s$ of the original layer where Δs is small. At time t , this segment extends between $x(s, t)$ and

$x(s + \Delta s, t)$, and the velocity is $\dot{x}(s, t) = \frac{\partial x(s, t)}{\partial t}$ while the acceleration is $\ddot{x}(s, t) = \frac{\partial^2 x(s, t)}{\partial t^2}$. We will use the notation $v(t) = \dot{x}(1, t)$ to denote the velocity of the leading edge at time t ($s = 1$ is the right boundary of the original cell layer in dimensionless units). Balance of momentum implies

$$M(s, t)\ddot{x}(s, t) + B(s, t)\dot{x}(s, t) = f(s + \Delta s, t) - f(s, t), \quad (2.1)$$

where $M(s, t)$ is the time-dependent mass of the segment, $B(s, t)$ is the coefficient describing the sliding resistance due to adhesion of the cells to the substrate, and $f(s, t)$ is the resultant force on a cross section of the cell layer.

Deformation of a cell is accompanied by an active remodeling of the cytoskeleton, generally resulting in a viscoelastic stress-strain response (Fung [22]). The resultant force f describes the stress-strain relationship of the cell layer. f is a function of the strain (displacement gradient), ϵ , defined as

$$\epsilon(s, t) = \frac{\partial x(s, t)}{\partial \hat{s}} - 1, \quad (2.2)$$

where $\epsilon > 0$ corresponds to stretch and $-1 < \epsilon < 0$ corresponds to compression. Various constitutive functions can be employed to relate f to the strain; examples (see Figure 2.2A) include

$$\text{logarithmic:} \quad f = \phi(\epsilon) = k \ln(\epsilon + 1), \quad (2.3a)$$

$$\text{Hooke's law:} \quad f = \phi(\epsilon) = k\epsilon, \quad (2.3b)$$

$$\text{ideal gas law:} \quad f = \phi(\epsilon) = k \left(1 - \frac{1}{\epsilon + 1} \right), \quad (2.3c)$$

where k is the residual stretching modulus of the cell layer after cytoskeleton relaxation. The timescale of the motion of the cell layer, which is on the order of hours, is slow compared to the relaxation time of single-cell deformation, which is on the order of tens of seconds (Canetta et al. [8]), so it is assumed that k is time-independent. Thus, the cell layer responds instantaneously and passively to the forces generated on it. k has units of force, since the cell layer thickness is assumed to be constant. Of the constitutive functions (2.3), only the logarithmic relation allows for an infinite magnitude of stress for both $\epsilon \rightarrow -1$ and $\epsilon \rightarrow \infty$,

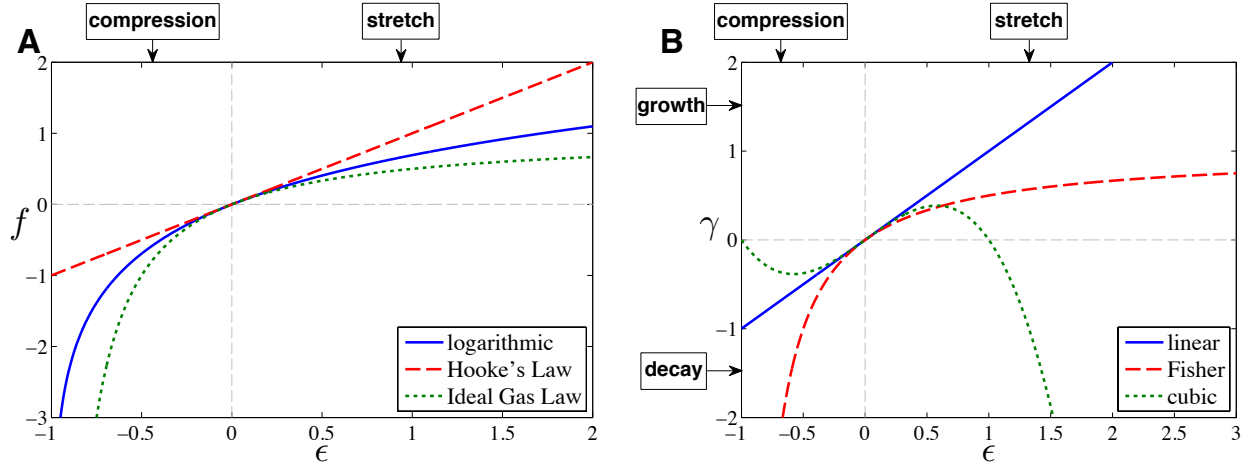


Figure 2.2: (A) Resultant forces f (2.3) that will be analyzed as a function of ϵ . Here, $k = 1$. $\epsilon > 0$ corresponds to stretching of the cell layer and $-1 < \epsilon < 0$ corresponds to compression of the cell layer. (B) Growth functions γ (2.9) that will be analyzed as a function of ϵ . $\epsilon > 0$ corresponds to stretching of the cell layer and $-1 < \epsilon < 0$ corresponds to compression of the cell layer. $\gamma > 0$ corresponds to cell proliferation and $\gamma < 0$ corresponds to cell apoptosis.

giving a physiologically appropriate behavior at both large and small densities. We derive our results for a general function ϕ but restrict our attention to cases in which ϕ is monotone increasing in ϵ and $\phi(0) = 0$.

Let b be the adhesion constant between the cell layer and the substrate, which has units of force times time divided by length squared. Assuming that the coefficient $B(s, t)$ is proportional to the extent of contact of the segment with the substrate (Cetin et al. [9], Qureshi et al. [55]),

$$B(s, t) = (x(s + \Delta s, t) - x(s, t))b, \quad (2.4)$$

and assuming acceleration is negligible since the motion is slow, (2.1) becomes

$$(x(s + \Delta s, t) - x(s, t))b\dot{x}(s, t) = f(s + \Delta s, t) - f(s, t). \quad (2.5)$$

Taking the limit as $\Delta s \rightarrow 0$ results in the governing equation for the motion of the layer

$$b \frac{\partial x}{\partial s} \frac{\partial x}{\partial t} = \frac{\partial f}{\partial s}. \quad (2.6)$$

Material growth and decay of the cell layer can be described using the growth gradient, g , defined as

$$g(s, t) = \frac{\partial \hat{s}(s, t)}{\partial s}, \quad (2.7)$$

which obeys

$$\frac{\partial g}{\partial t} = \gamma g, \quad (2.8)$$

where γ is the cell proliferation rate given by a constitutive assumption that may depend on s , t , g , and/or ϵ . In this dissertation we analyze the dependence of proliferation on stress and strain within the layer, and hence we assume that γ is dependent solely on ϵ , i.e. $\gamma = \gamma(\epsilon)$. We assume that a stretched cell layer is more likely to proliferate than a compressed layer (Bindschadler and McGrath [5]). Examples of possible growth functions that will be analyzed in this dissertation (see Figure 2.2B) include

$$\text{linear: } \quad \gamma(\epsilon) = \epsilon, \quad (2.9a)$$

$$\text{Fisher: } \quad \gamma(\epsilon) = \frac{\epsilon}{\epsilon + 1}, \quad (2.9b)$$

$$\text{cubic: } \quad \gamma(\epsilon) = -\epsilon(\epsilon^2 - 1). \quad (2.9c)$$

The set of equations (2.6) and (2.8) will be further called the *material formulation* of the one-dimensional single layer cell migration model. These two equations are coupled through the resultant force f .

To see how equations (2.6) and (2.8) are coupled, for example assume that f is the logarithmic elasticity function (2.3a). From the definitions (2.2) and (2.7),

$$\epsilon = \frac{\partial x}{\partial \hat{s}} - 1 = \frac{\partial x}{\partial s} \left(\frac{\partial \hat{s}}{\partial s} \right)^{-1} - 1 = \frac{\partial x}{\partial s} \frac{1}{g} - 1, \quad (2.10)$$

and then f can be written as

$$f = \phi(\epsilon) = k \ln(\epsilon + 1) = k \ln \left(\frac{\partial x}{\partial s} \frac{1}{g} \right) = k \left(\ln \left(\frac{\partial x}{\partial s} \right) - \ln(g) \right). \quad (2.11)$$

Substituting (2.11) into (2.6), we obtain

$$\frac{\partial x}{\partial t} = \frac{k}{b} \left(\frac{\frac{\partial^2 x}{\partial s^2}}{\left(\frac{\partial x}{\partial s} \right)^2} - \frac{\frac{\partial g}{\partial s}}{g \frac{\partial x}{\partial s}} \right), \quad (2.12)$$

and then the material formulation consists of (2.12) and (2.8), which are clearly coupled.

We note that the equations of the slowly varying continuum approximation of the agent-based model of Fozard et al. [19], neglecting internal cell viscosity, are the same as the material formulation with no cell proliferation ($\gamma(\epsilon) = 0$) and Hooke's law elasticity function (2.3b).

In all cases studied in this dissertation, we assume that the cell layer is initially uniform and free from internal stresses, the location of the left boundary of the cell layer (at $s = 0$) is fixed while the right boundary (at $s = 1$ in dimensionless units) is free to move, and the force applied at the right boundary is constant and equal to F , a parameter which represents the net external force that develops as a result of lamellipodia formation. Thus, the initial and boundary conditions are

$$x(s, 0) = s, \quad 0 \leq s \leq 1, \quad (2.13a)$$

$$g(s, 0) = 1, \quad 0 \leq s \leq 1, \quad (2.13b)$$

$$x(0, t) = 0, \quad 0 \leq t, \quad (2.13c)$$

$$f(1, t) = F, \quad 0 < t. \quad (2.13d)$$

In summary, the equations, initial and boundary conditions, variables, constitutive functions, and parameters for the material formulation of the one-dimensional single layer cell migration model are as follows.

Model 1. Material Formulation of 1-D Single Layer Cell Migration	
Governing Equations	
$b \frac{\partial x}{\partial s} \frac{\partial x}{\partial t} = \frac{\partial f}{\partial s},$	$0 \leq s \leq 1, 0 < t$
$\frac{\partial g}{\partial t} = \gamma(\epsilon)g,$	$0 \leq s \leq 1, 0 < t$
Initial Conditions	
$x(s, 0) = s,$	$0 \leq s \leq 1$
$g(s, 0) = 1,$	$0 \leq s \leq 1$

Boundary Conditions

$$\begin{aligned}x(0, t) &= 0, & 0 \leq t \\f(1, t) &= F, & 0 < t\end{aligned}$$

Variables

- t = time
- s = position of a cell in the original cell layer
- $\hat{s}(s, t)$ = hypothetical position of cell s at time t if all deformation in the layer was instantaneously removed
- $\epsilon(s, t) = \frac{\partial x(s, t)}{\partial \hat{s}} - 1$ = strain (displacement gradient)
- $x(s, t)$ = position of cell s at time t
- $g(s, t) = \frac{\partial \hat{s}(s, t)}{\partial s}$ = growth gradient

Constitutive Functions

- f = resultant force on a cross section of the cell layer (describes the stress-strain relationship of the cell layer)
- γ = cell proliferation rate

Parameters

- b = adhesion constant between the cell layer and the substrate
- F = net external force that develops as a result of lamellipodia formation
- k = residual stretching modulus of the layer after cytoskeleton relaxation

2.2 DERIVATION OF SPATIAL FORMULATION

Though the model of Arciero et al. [3] describes two-dimensional cell layer movement in spatial, or Eulerian, coordinates, we will summarize it here in terms of one-dimensional movement. The most significant difference between this model and the model described in the previous section is the coordinate system. In the material formulation, each cell in the

layer is considered individually. In the spatial formulation, the density of cells in the layer is considered as a whole. We will derive the equivalence between the two formulations in the subsequent section.

The cell layer is represented as a compressible fluid, and the variable $\rho(x, t)$ describes the cell density as a function of position x and time t . The law of conservation of cell number (mass),

$$\frac{\partial \rho(x, t)}{\partial t} = -\frac{\partial}{\partial x} \left(\rho(x, t) \frac{\partial x}{\partial t} \right) + q(\rho(x, t)), \quad (2.14)$$

where $\frac{\partial x}{\partial t}$ is the velocity of the cell layer, includes the growth term $q(\rho)$ that describes the density-dependent net rate of change in the number of cells within the layer due to proliferation and apoptosis. The relation between q and γ will be shown in the next section.

Balance of linear momentum implies

$$\rho(x, t) \frac{\partial^2 x}{\partial t^2} + \rho(x, t) \frac{\partial x}{\partial t} \frac{\partial^2 x}{\partial t^2} = \widehat{B}(x, t) + \frac{\partial T(x, t)}{\partial x}, \quad (2.15)$$

where the tensor $T(x, t)$ represents the stresses within the cell layer and $\widehat{B}(x, t)$ accounts for the force of adhesion of the cell layer to the substrate. \widehat{B} is the result of the action exerted on a material element by the substrate, i.e. the negative of traction force. As in the previous section, it is assumed that \widehat{B} is negatively proportional to the cell layer velocity,

$$\widehat{B}(x, t) = -b \frac{\partial x}{\partial t}. \quad (2.16)$$

The cell layer is assumed to behave as a compressible inviscid fluid with the constitutive equation

$$T = -p(\rho), \quad (2.17)$$

where p is the pressure within the cell layer. The pressure depends on the cell density and is taken to be positive when cells are compressed and negative when cells are stretched. It

is related to the resultant force f , which will be stated in the next section. Defining ρ_0 as the constant density of the initial relaxed (unstressed) cell layer, this corresponds to

$$p(\rho) > 0, \quad \text{if } \rho > \rho_0, \quad (2.18a)$$

$$p(\rho) < 0, \quad \text{if } \rho < \rho_0, \quad (2.18b)$$

$$p(\rho_0) = 0, \quad (2.18c)$$

$$p'(\rho) > 0. \quad (2.18d)$$

Assuming acceleration is negligible and substituting equations (2.16) and (2.17) into (2.15), we obtain

$$\frac{\partial x}{\partial t} = -\frac{1}{b}p'(\rho)\frac{\partial \rho}{\partial x}, \quad (2.19)$$

which is the relation between the velocity of cells and the gradient of cell density; it resembles Darcy's law describing the flow of fluid through a porous medium.

Substituting (2.19) into (2.14) results in the governing equation that describes the evolution of cell density,

$$\frac{\partial \rho}{\partial t} = \frac{1}{b}\frac{\partial}{\partial x}\left(\rho p'(\rho)\frac{\partial \rho}{\partial x}\right) + q(\rho), \quad (2.20)$$

which we term the *spatial formulation* of the one-dimensional single layer cell migration model.

As we will see in Section 2.3.4, one of the boundary conditions in the spatial formulation describes the speed of the moving edge, which is called a Stefan condition. The spatial formulation is thus a generalized free boundary problem, or Stefan problem. The Stefan problem was first derived for the transfer of heat during solidification or melting processes, where ρ would represent the temperature and the moving edge would represent the boundary where phase transitions occur. Classical solutions in small time intervals for smooth domains was shown by Hanzawa [28] and global existence and uniqueness of weak solutions were shown by Kamenomostskaja [34], Oleinik [48], and Friedman [21].

In summary, the equations; initial, boundary, and Stefan conditions (which will be derived in Section 2.3.4); variables; constitutive functions; and parameters for the spatial formulation of the one-dimensional single layer cell migration model are as follows.

Model 2. Spatial Formulation of 1-D Single Layer Cell Migration

Governing Equation

$$\frac{\partial \rho}{\partial t} = \frac{1}{b} \frac{\partial}{\partial x} \left(\rho p'(\rho) \frac{\partial \rho}{\partial x} \right) + q(\rho), \quad 0 \leq x \leq X(0), 0 < t$$

Initial Condition

$$\rho(x, 0) = \rho_0, \quad 0 \leq x \leq X(0)$$

Boundary Conditions

$$\begin{aligned} \frac{\partial \rho(0, t)}{\partial x} &= 0, & 0 \leq t \\ p(\rho(X(t), t)) &= -F, & 0 < t \end{aligned}$$

Stefan Condition

$$X'(t) = -\frac{1}{b} p'(\rho(X(t), t)) \frac{\partial \rho(X(t), t)}{\partial x}, \quad 0 < t$$

Variables

- t = time
- x = spatial position of cells
- $X(t)$ = position of the leading edge in spatial coordinates
- $\rho(x, t)$ = cell density

Constitutive Functions

- p = pressure within the cell layer (describes the stress-strain relationship of the cell layer)
- q = growth term describing the density-dependent net rate of change in the number of cells within the layer due to proliferation and apoptosis

Parameters

- b = adhesion constant between the cell layer and the substrate

- F = net external force that develops as a result of lamellipodia formation
- k = residual stretching modulus of the layer after cytoskeleton relaxation
- ρ_0 = constant density of the initial relaxed (unstressed) cell layer

2.3 EQUIVALENCE OF MODELS

There is an equivalence between material and spatial coordinates through point-particle interchangeability (see Figure 2.3). In the material coordinates description, $x = x(s, t)$, and in the spatial coordinates description, $s = s(x, t)$, and therefore we have $x(s(x, t), t) = x$ and $s(x(s, t), t) = s$. We will also use the notation $\tilde{\rho}(s, t) = \rho(x(s, t), t)$, where $\tilde{\rho}$ is the density of cells in material coordinates defined as

$$\tilde{\rho}(s, t) = \rho_0 \left(\frac{\partial x(s, t)}{\partial \hat{s}} \right)^{-1}. \quad (2.21)$$

Note that (2.21) and (2.2) imply

$$\epsilon(s, t) = \frac{\rho_0}{\tilde{\rho}(s, t)} - 1. \quad (2.22)$$

In this section, we will show that the material formulation of the one-dimensional single layer model (Model 1) is equivalent to the spatial formulation (Model 2).

2.3.1 Governing Equations and Elasticity Functions

Evaluating the equation relating the velocity of cells and the gradient of cell density in the spatial formulation, equation (2.19), at $x = x(s, t)$, we obtain

$$\frac{\partial x}{\partial t} = -\frac{1}{b} p'(\tilde{\rho}) \frac{\partial \tilde{\rho}}{\partial x} = -\frac{1}{b} \frac{\partial}{\partial x} (p(\tilde{\rho})) = -\frac{1}{b} \frac{\partial s}{\partial x} \frac{\partial}{\partial s} (p(\tilde{\rho})) = -\frac{1}{b} \frac{\partial p(\tilde{\rho}) / \partial s}{\partial x / \partial s}. \quad (2.23)$$

This is the same equation as the material formulation governing equation (2.6) since, by definition,

$$f(s, t) = -p(\tilde{\rho}(s, t)), \quad (2.24)$$

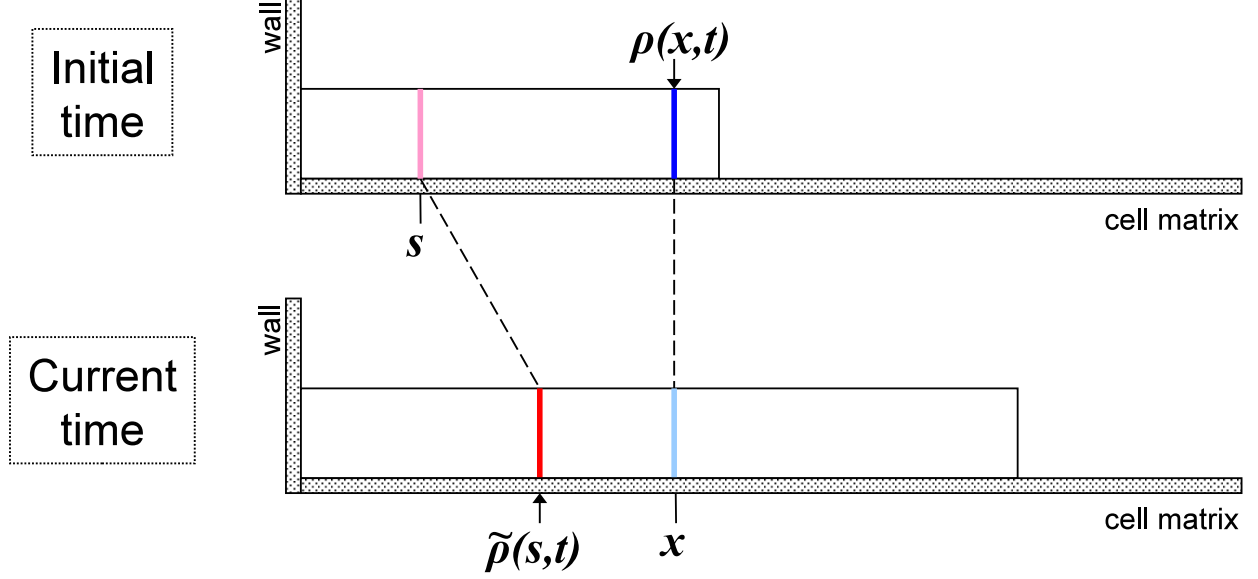


Figure 2.3: *Material vs. spatial coordinates: The red and pink bars illustrate the material (Lagrangian) description of motion, where the current density $\tilde{\rho}(s,t)$ depends on initial point s and time t . The blue and light blue bars illustrate the spatial (Eulerian) description of motion, where the initial density $\rho(x,t)$ depends on current point x and time t .*

implying that we have equivalence between the governing equations of the two models.

From (2.24), we obtain conversion formulas for the elasticity functions

$$\phi(\epsilon) = -p \left(\frac{\rho_0}{\epsilon + 1} \right), \quad (2.25a)$$

$$p(\rho) = -\phi \left(\frac{\rho_0}{\rho} - 1 \right). \quad (2.25b)$$

Note that the case when ϕ is monotone increasing on $\epsilon \in (-1, \infty)$ implies that p is monotone increasing on $\rho \in (0, \infty)$.

The equivalent spatial coordinates logarithmic (2.3a), Hooke's law (2.3b), and ideal gas law (2.3c) cell layer stress-strain relationships are, respectively,

$$p(\rho) = k \ln \left(\frac{\rho}{\rho_0} \right), \quad (2.26a)$$

$$p(\rho) = k \left(1 - \frac{\rho_0}{\rho} \right), \quad (2.26b)$$

$$p(\rho) = k \left(\frac{\rho}{\rho_0} - 1 \right). \quad (2.26c)$$

2.3.2 Cell Proliferation Functions

To derive the relation between the growth functions γ and q , we note that the material derivative

$$\frac{\partial \rho(x(s, t), t)}{\partial t} = \frac{\partial \rho(x, t)}{\partial x} \Big|_{x=x(s, t)} \frac{\partial x(s, t)}{\partial t} + \frac{\partial \rho(x, t)}{\partial t} \Big|_{x=x(s, t)}, \quad (2.27)$$

is equivalent, by notation, to

$$\frac{\partial \tilde{\rho}(s, t)}{\partial t} = \rho_0 \left(\frac{\partial x(s, t)}{\partial s} \right)^{-1} \frac{\partial^2 \hat{s}(s, t)}{\partial s \partial t} - \rho_0 \frac{\partial \hat{s}(s, t)}{\partial s} \left(\frac{\partial x(s, t)}{\partial s} \right)^{-2} \frac{\partial^2 x(s, t)}{\partial s \partial t}. \quad (2.28)$$

Equating the right hand sides of the last two equations (2.27) and (2.28),

$$\begin{aligned} \frac{\partial \rho(x, t)}{\partial t} \Big|_{x=x(s, t)} &= \rho_0 \left(\frac{\partial x(s, t)}{\partial s} \right)^{-1} \frac{\partial^2 \hat{s}(s, t)}{\partial s \partial t} - \rho_0 \frac{\partial \hat{s}(s, t)}{\partial s} \left(\frac{\partial x(s, t)}{\partial s} \right)^{-2} \frac{\partial^2 x(s, t)}{\partial s \partial t} \\ &\quad - \frac{\partial \rho(x, t)}{\partial x} \Big|_{x=x(s, t)} \frac{\partial x(s, t)}{\partial t}, \end{aligned} \quad (2.29)$$

which is the left hand side of the conservation of mass equation (2.14) evaluated at $x = x(s, t)$.

The right hand side of (2.14) evaluated at $x = x(s, t)$ is

$$\begin{aligned} - \rho(x, t) \Big|_{x=x(s, t)} \left(\frac{\partial x(s, t)}{\partial s} \right)^{-1} \frac{\partial}{\partial s} \left(\frac{\partial x(s, t)}{\partial t} \right) \\ - \frac{\partial x(s, t)}{\partial t} \frac{\partial \rho(x, t)}{\partial x} \Big|_{x=x(s, t)} + q(\rho(x, t)) \Big|_{x=x(s, t)}, \end{aligned} \quad (2.30)$$

which is equal to

$$- \rho_0 \left(\frac{\partial x(s, t)}{\partial s} \right)^{-2} \frac{\partial \hat{s}(s, t)}{\partial s} \frac{\partial^2 x(s, t)}{\partial s \partial t} - \frac{\partial x(s, t)}{\partial t} \frac{\partial \rho(x, t)}{\partial x} \Big|_{x=x(s, t)} + q(\rho(x, t)) \Big|_{x=x(s, t)}. \quad (2.31)$$

Thus, equating (2.29) and (2.31) and evaluating at $x = x(s(x, t), t)$, we conclude that

$$q(\tilde{\rho}(s, t)) = \rho_0 \left(\frac{\partial x(s, t)}{\partial s} \right)^{-1} \frac{\partial^2 \hat{s}(s, t)}{\partial s \partial t}. \quad (2.32)$$

Since $g(s, t) = \frac{\partial \hat{s}(s, t)}{\partial s}$ by definition (recall (2.7)), then $\frac{\partial g(s, t)}{\partial t} = \frac{\partial^2 \hat{s}(s, t)}{\partial s \partial t}$, and in view of the growth gradient equation (2.8), we have

$$\frac{\partial^2 \hat{s}(s, t)}{\partial s \partial t} = \gamma(\epsilon(s, t))g(s, t). \quad (2.33)$$

Substituting (2.33) into (2.32) and recalling the strain equation (2.22), we thus obtain conversion formulas for the growth functions

$$\gamma(\epsilon) = \frac{\epsilon + 1}{\rho_0} q \left(\frac{\rho_0}{\epsilon + 1} \right), \quad (2.34a)$$

$$q(\rho) = \rho \gamma \left(\frac{\rho_0}{\rho} - 1 \right). \quad (2.34b)$$

The spatial coordinates equivalents to the material coordinates linear (2.9a), Fisher (2.9b), and cubic (2.9c) growth functions are, respectively,

$$q(\rho) = \rho_0 - \rho, \quad (2.35a)$$

$$q(\rho) = \rho \left(1 - \frac{\rho}{\rho_0} \right), \quad (2.35b)$$

$$q(\rho) = -\frac{\rho_0}{\rho^2} (\rho_0 - \rho) (\rho_0 - 2\rho). \quad (2.35c)$$

2.3.3 Growth Gradient

The spatial coordinates model of Arciero et al. [3] does not include an expression for the growth gradient. Let us introduce the notation

$$g(s, t) = \widehat{g}(x(s, t), t), \quad (2.36)$$

where \widehat{g} is the growth gradient in spatial coordinates. Taking the partial derivative of both sides of (2.36) with respect to t , from the growth gradient equation (2.8) and the material derivative we obtain

$$\gamma(\epsilon(s, t))g(s, t) = \frac{\partial \widehat{g}(x, t)}{\partial x} \Big|_{x=x(s, t)} \frac{\partial x(s, t)}{\partial t} + \frac{\partial \widehat{g}(x, t)}{\partial t} \Big|_{x=x(s, t)}. \quad (2.37)$$

From the conversion formulas (2.34), we derive

$$\gamma(\epsilon(s, t)) = \frac{1}{\tilde{\rho}(s, t)} q(\tilde{\rho}(s, t)). \quad (2.38)$$

From the material formulation governing equation (2.6) and by definitions,

$$\begin{aligned} \frac{\partial x}{\partial t} &= \frac{1}{b} \left(\frac{\partial x}{\partial s} \right)^{-1} \frac{\partial f}{\partial s} = -\frac{1}{b} \left(\frac{\partial x}{\partial \hat{s}} \frac{\partial \hat{s}}{\partial s} \right)^{-1} \frac{\partial}{\partial s} (p(\tilde{\rho})) = -\frac{1}{b} \left(\frac{\partial x}{\partial \hat{s}} \frac{\partial \hat{s}}{\partial s} \right)^{-1} \frac{dp(\tilde{\rho})}{d\tilde{\rho}} \frac{\partial \tilde{\rho}}{\partial x} \frac{\partial x}{\partial \hat{s}} \frac{\partial \hat{s}}{\partial s} \\ &= -\frac{1}{b} \frac{dp(\tilde{\rho})}{d\tilde{\rho}} \frac{\partial \tilde{\rho}}{\partial x}. \end{aligned} \quad (2.39)$$

Substituting (2.38) and (2.39) into (2.37) and evaluating at $s = s(x, t)$, we obtain the following partial differential equation for \widehat{g} ,

$$\frac{\partial \widehat{g}}{\partial t} - \frac{1}{b} p'(\rho) \frac{\partial \widehat{g}}{\partial x} - \frac{q(\rho)}{\rho} \widehat{g} = 0. \quad (2.40)$$

2.3.4 Initial and Boundary Conditions

To derive the equivalent initial and boundary conditions for the spatial formulation compared to the conditions for the material formulation (2.13), define $X(t)$ as the position of the leading edge in spatial coordinates. Assuming the cell layer is initially uniform and free from internal stresses, initial condition (2.13a), via (2.21), is equivalent to

$$\rho(x, 0) = \rho_0, \quad 0 \leq x \leq X(0). \quad (2.41)$$

Note that this assumption is contrary to Arciero et al. [3]. Assuming the left boundary of the cell layer is fixed, boundary condition (2.13c) is equivalent to a no flux Neumann condition

$$\frac{\partial \rho(0, t)}{\partial x} = 0, \quad 0 \leq t. \quad (2.42)$$

Assuming the force applied at the right boundary is equal to F , boundary condition (2.13d), via (2.24), is equivalent to

$$p(\rho(X(t), t)) = -F, \quad 0 < t. \quad (2.43)$$

Lastly, the speed of the leading edge $X(t)$ satisfies (2.19), so we have the Stefan boundary condition

$$X'(t) = -\frac{1}{b} p'(\rho(X(t), t)) \frac{\partial \rho(X(t), t)}{\partial x}, \quad 0 < t. \quad (2.44)$$

3.0 NUMERICAL SOLUTIONS OF 1-D SINGLE LAYER MODEL

The material formulation of the one-dimensional single layer model ([Model 1](#)) describes the current configuration of cells with respect to the variable s that is defined on a fixed domain, so it is straightforward to step through time to solve the model equations at each time step. The spatial formulation ([Model 2](#)) includes a free boundary making it significantly more difficult to solve numerically. Thus, for numerical solutions of the one-dimensional single layer model we will utilize the material formulation, but as we will see in [Chapter 4](#), there are advantages of using the spatial formulation instead for some analytic solutions.

A numerical solution of the material formulation model equations for a given cell proliferation function γ , elasticity function f , and parameters k , b , and F can be found using an adaptive finite difference method based on the method of Mi et al. [[43](#)]. Using a nonadaptive mesh results in exponential growth at the leading edge, an unrealistic result. By adaptively refining the mesh at positions of largest growth, we inhibit numerical errors. Please see [Section 3.1](#) for details of the solution method and [Section 3.1.1](#) for details on the consistency, stability, and convergence of the method. Parameter values used were chosen based on estimates from Mi et al. [[43](#)].

[Figures 3.1–3.4](#) show the evolution of the cell layer for zero, linear ([2.9a](#)), Fisher ([2.9b](#)), and cubic ([2.9c](#)) cell proliferation functions and logarithmic ([2.3a](#)), Hooke’s law ([2.3b](#)), and ideal gas law ([2.3c](#)) elasticity functions.

In [Figure 3.1](#), we observe that the velocity of the leading edge converges to 0 and the cells move a finite distance to the right for the logarithmic and Hooke’s law elasticity functions, as well as the ideal gas law elasticity function although the convergence is much slower in this case. This is a limiting case of the time-dependent solution and there is a maximum

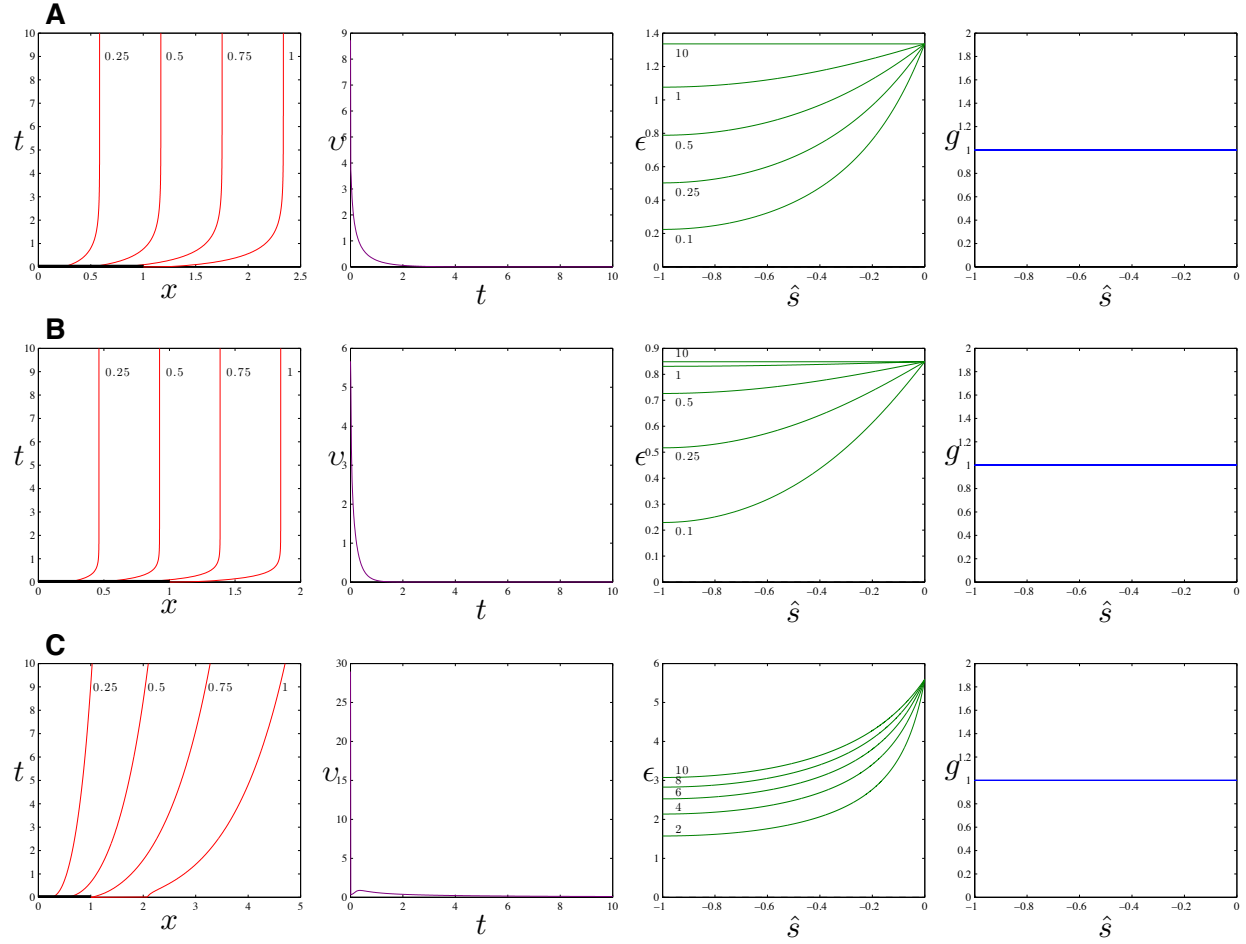


Figure 3.1: Numerical solution of the 1-D single layer model: no growth $\gamma(\epsilon) = 0$, $k = 2.947$, $b = 1$, and $F = 2.5$. Here, as in Figures 3.2–3.4 below, the first column shows the position x of cells with $s = 0.25, 0.5, 0.75, 1$, as time (in hours) increases. Each curve is labeled by its initial position between $[0, 1]$ on the x -axis and represents the path of one cell from where it begins initially to how far right it moves as time increases along the t -axis. The second column shows the velocity of the leading edge v as a function of time (in hours). The third column shows the strain ϵ as a function of position \hat{s} . Each curve is labeled by the time (in hours) and represents the solution translated to the left so that the largest value of \hat{s} for each time shown is 0. The last column shows the growth gradient g as a function of position \hat{s} . Each curve is labeled by the time (in hours) and represents the solution translated to the left so that the largest value of \hat{s} for each time shown is 0. (A) Logarithmic elasticity function (2.3a), (B) Hooke's law elasticity function (2.3b), (C) ideal gas law elasticity function (2.3c).

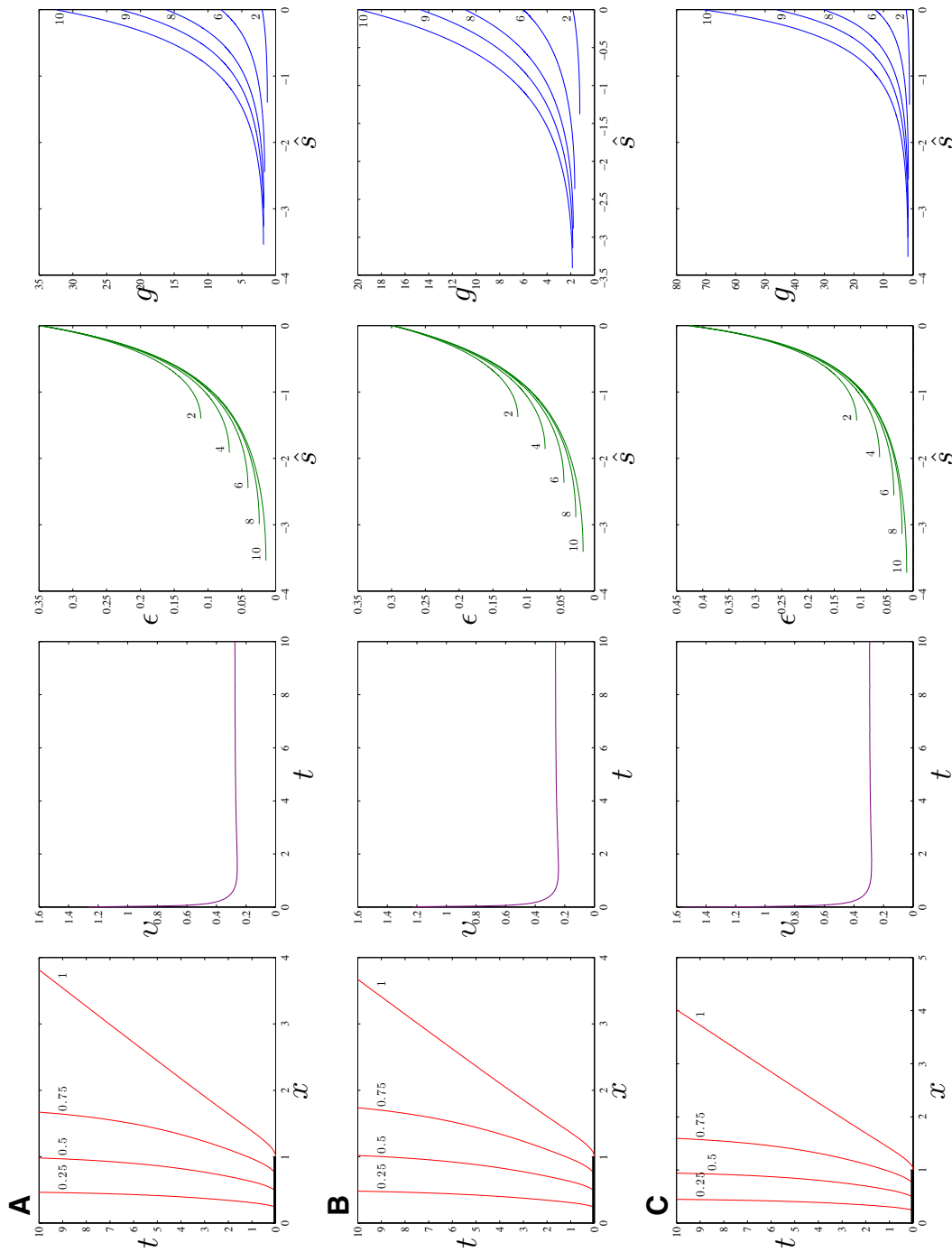


Figure 3.2: Numerical solution of the 1-D single layer model: linear growth function (2.9a), $k = 0.838$, $b = 1$, and $F = 0.25$. (A) Logarithmic elasticity function (2.3a), (B) Hooke's law elasticity function (2.3b), (C) ideal gas law elasticity function (2.3c). See Figure 3.1 for a description of each column.

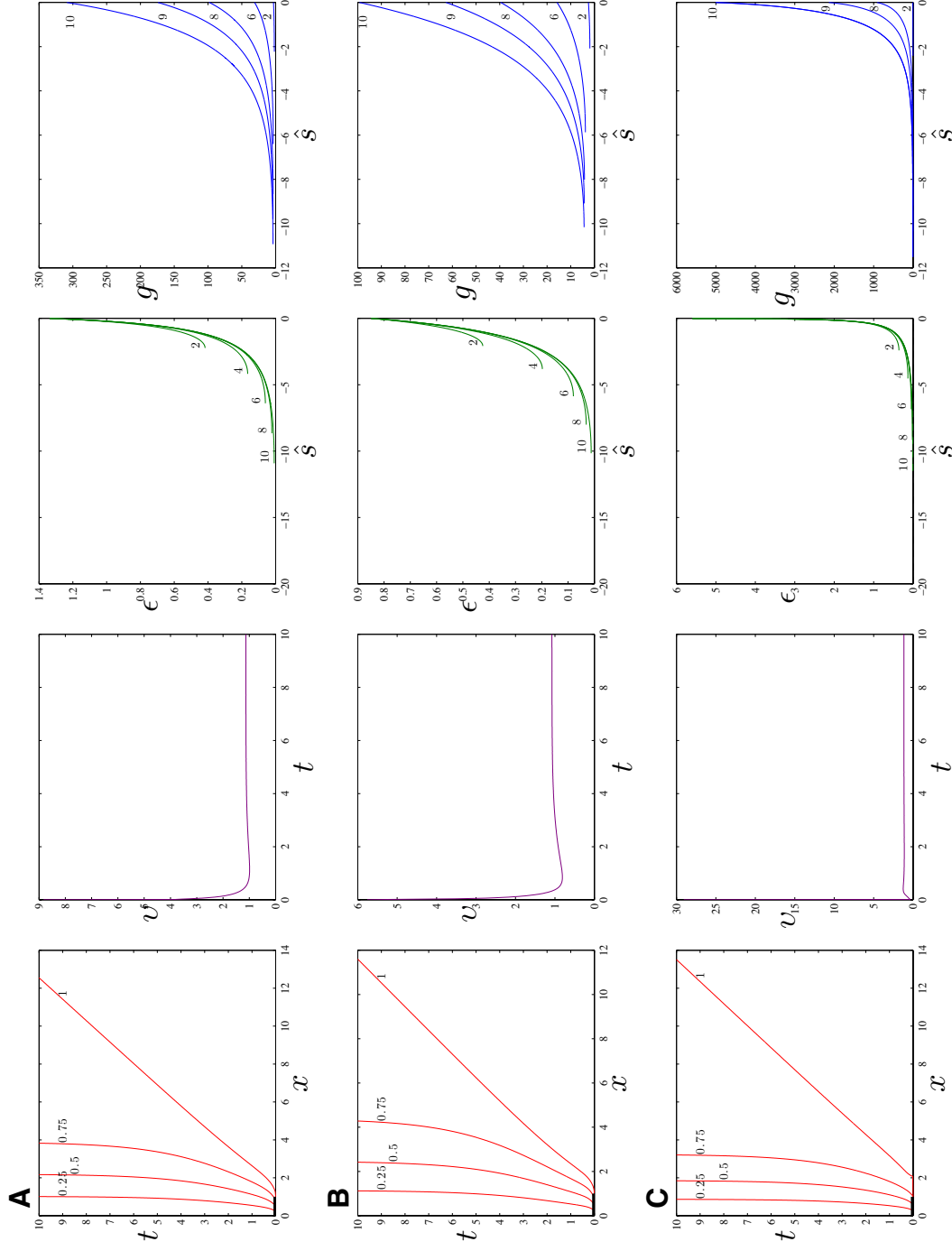


Figure 3.3: Numerical solution of the 1-D single layer model: Fisher growth function (2.9b), $k = 2.947$, $b = 1$, and $F = 2.5$. (A) Logarithmic elasticity function (2.3a), (B) Hooke's law elasticity function (2.3b), (C) ideal gas law elasticity function (2.3c). See Figure 3.1 for a description of each column.

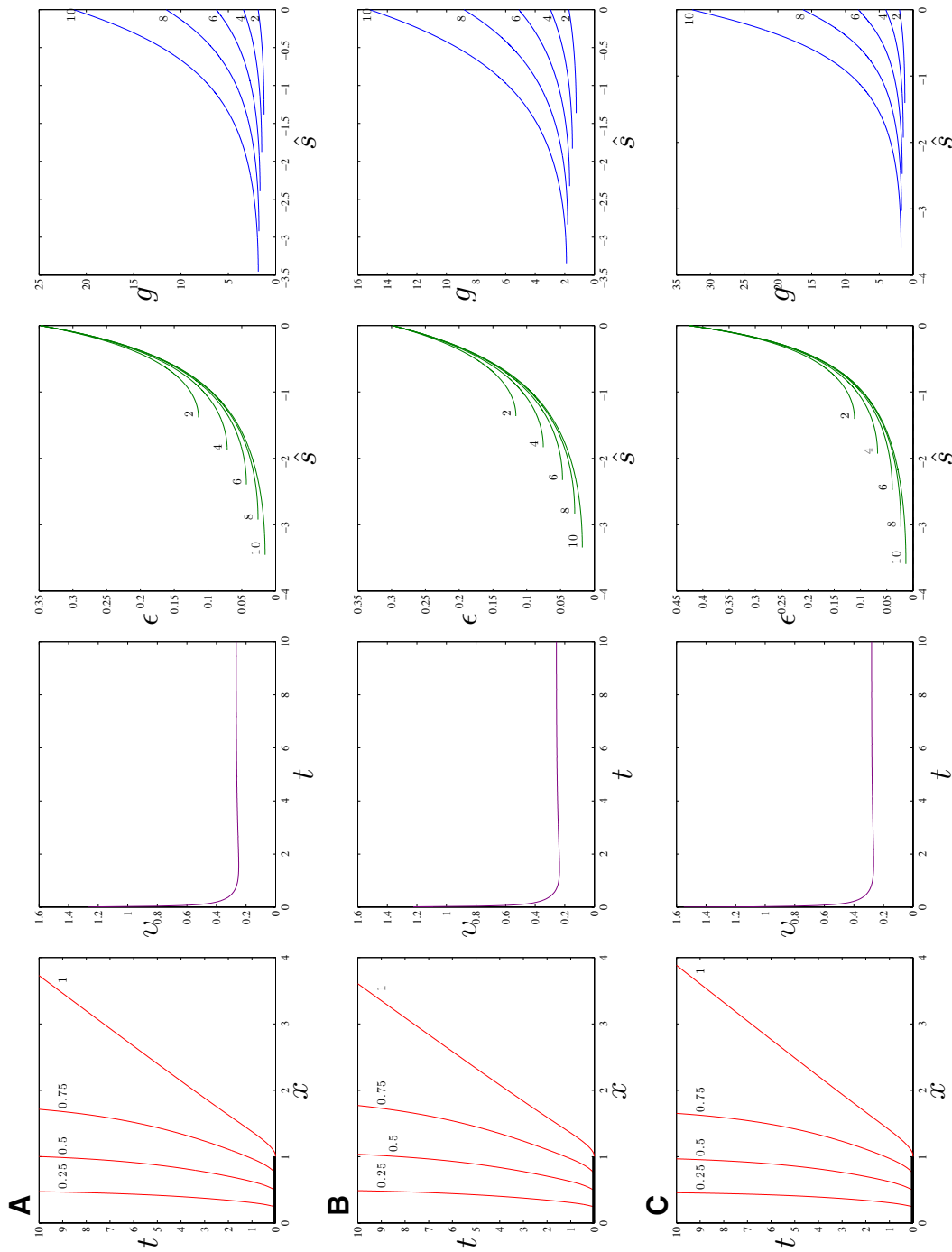


Figure 3.4: Numerical solution of the 1-D single layer model: cubic growth function (2.9c), $k = 0.838$, $b = 1$, and $F = 0.25$. (A) Logarithmic elasticity function (2.3a), (B) Hooke's law elasticity function (2.3b), (C) ideal gas law elasticity function (2.3c). See Figure 3.1 for a description of each column.

distance the right edge of the cell layer can reach, which is

$$\phi^{-1}(F) + 1, \tag{3.1}$$

where $^{-1}$ denotes the inverse. This phenomenon of large wounds being unable to close was described by Mi et al. [43] and verified experimentally. The initial evolution of the finite size layer and the evolution of a layer that is semi-infinite (extending to infinity on the left side) is governed by a similarity solution. We analyze the existence of similarity under scaling solutions in Section 4.1 in the absence of cell proliferation.

In Figures 3.2–3.4, we observe that the velocity of the leading edge converges to a positive constant and the curves in the plots of ϵ versus \hat{s} converge to a similar shape. This behavior occurs for the logarithmic, Hooke’s law, and ideal gas law elasticity functions. It is indicative of a traveling wave, a wave that travels at constant velocity without change of shape. In Section 4.2, we analyze the existence of traveling wave solutions using phase plane and bifurcation analysis.

We point out that, for the zero, linear, Fisher, and cubic growth functions, the range of the numerically realized ϵ is the largest for the ideal gas law elasticity function and smallest for the Hooke’s law elasticity function. The nonzero growth functions behave similarly within the numerically realized ϵ ranges for the logarithmic and Hooke’s law elasticity functions (see Figure 2.2B).

3.1 ADAPTIVE FINITE DIFFERENCE METHOD

A numerical solution of the material formulation (Model 1) can be found using an adaptive finite difference method based on the method of Mi et al. [43] for a given cell proliferation function γ , elasticity function f , and parameters k , b , and F .

Let $\Delta t > 0$ be a given step size and $t_i = (i - 1)\Delta t$, $i = 1, 2, 3, \dots$. Let

$$0 = s_1 < s_2 < \dots < s_j < s_{j+1} < \dots < s_{N_1} = 1$$

be the initial uniform or nonuniform mesh of $[0, 1]$, where N_i denotes the number of space steps in the mesh at a given time step t_i . Let x_i^j denote the numerical approximation of the cell position $x(s_j, t_i)$, and let g_i^j denote the numerical approximation of the growth gradient $g(s_j, t_i)$.

A nonadaptive finite difference method results in erroneous exponential growth at the cell layer gap edge due to the moving boundary and expanding mesh (see Section 3.1.1). Let TOL denote a maximum allowed distance between any two cells. At time step t_i , if any two cells at positions x_i^j and x_i^{j+1} for some j are further apart than TOL , we add a new mesh point halfway between s_j and s_{j+1} and linearly interpolate the position x and growth gradient g at the new mesh point. The new mesh is used for time step t_{i+1} .

Various resultant forces f can be assumed, but for a concrete example assume $f = \phi(\epsilon) = k \ln(\epsilon + 1)$, and define parameters $\kappa = \frac{k}{b}$ and $\varphi = \frac{F}{k}$. Recall from (2.2) and (2.7) that $\epsilon = \frac{\partial x}{\partial s} - 1 = \frac{\partial x}{\partial s} \frac{1}{g} - 1$.

The initial conditions imply, for $1 \leq j \leq N_i$,

$$x_1^j = s_j, \quad g_1^j = 1, \quad \epsilon_1^j = 0. \quad (3.2)$$

Equation (2.8) is solved first using explicit difference with a mixed discretization for the right hand side, for $1 \leq j \leq N_i$,

$$g_{i+1}^j = \frac{g_i^j}{1 - \Delta t \gamma(\epsilon_i^j)}. \quad (3.3)$$

Centered difference is used for ϵ in the interior and explicit difference for the boundaries, and because the right boundary is constant, for $i \geq 2$ and $2 \leq j \leq N_i - 1$,

$$\epsilon_i^j = \left(\frac{x_i^{j+1} + (\alpha^2 - 1)x_i^j - \alpha^2 x_i^{j-1}}{(\alpha + 1)(s_{j+1} - s_j)} \right) \frac{1}{g_i^j} - 1, \quad \alpha = \frac{s_{j+1} - s_j}{s_j - s_{j-1}}, \quad (3.4a)$$

$$\epsilon_i^1 = \left(\frac{x_i^2 - x_i^1}{s_2 - s_1} \right) \frac{1}{g_i^1} - 1, \quad (3.4b)$$

$$\epsilon_i^{N_i} = e^\varphi - 1. \quad (3.4c)$$

Equation (2.6) is solved next, and assuming f is of the form stated above, it becomes (see (2.12))

$$\frac{\partial x}{\partial t} = \kappa \left(\frac{\frac{\partial^2 x}{\partial s^2}}{\left(\frac{\partial x}{\partial s}\right)^2} - \frac{\frac{\partial g}{\partial s}}{g \frac{\partial x}{\partial s}} \right). \quad (3.5)$$

Using implicit difference in the numerator and explicit difference in the denominator to discretize the governing equation, we obtain a method that is first-order accurate in time and second-order accurate in space (see Section 3.1.1.1). For $i \geq 2$ and $2 \leq j \leq N_i - 1$,

$$x_{i+1}^j - x_i^j = \kappa \Delta t \left(\frac{\frac{2(s_{j+1} - s_{j-1})x_{i+1}^{j+1}}{s_{j+1} - s_j} - \frac{2(s_{j+1} - s_{j-1})^2 x_{i+1}^j}{(s_{j+1} - s_j)(s_j - s_{j-1})} + \frac{2(s_{j+1} - s_{j-1})x_{i+1}^{j-1}}{s_j - s_{j-1}}}{(x_i^{j+1} - x_i^{j-1})^2} - \frac{g_{i+1}^{j+1} - g_{i+1}^{j-1}}{g_i^j (x_i^{j+1} - x_i^{j-1})} \right), \quad (3.6)$$

which, after rearranging, becomes

$$\eta_j M_i^j x_{i+1}^{j+1} - (\sigma_j M_i^j + 1)x_{i+1}^j + \mu_j M_i^j x_{i+1}^{j-1} = -x_i^j + u_i^j, \quad (3.7)$$

where we have defined

$$M_i^j = \kappa \Delta t \left(\frac{2}{(x_i^{j+1} - x_i^{j-1})^2} \right), \quad (3.8a)$$

$$u_i^j = \kappa \Delta t \left(\frac{g_{i+1}^{j+1} - g_{i+1}^{j-1}}{g_i^j (x_i^{j+1} - x_i^{j-1})} \right), \quad (3.8b)$$

$$\eta_j = \frac{s_{j+1} - s_{j-1}}{s_{j+1} - s_j}, \quad (3.8c)$$

$$\sigma_j = \frac{(s_{j+1} - s_{j-1})^2}{(s_{j+1} - s_j)(s_j - s_{j-1})}, \quad (3.8d)$$

$$\mu_j = \frac{s_{j+1} - s_{j-1}}{s_j - s_{j-1}}. \quad (3.8e)$$

The boundary conditions imply, for $i \geq 2$,

$$x_i^1 = 0, \quad (3.9a)$$

$$x_i^{N_i} = x_i^{N_i-1} + (s_{N_i} - s_{N_i-1})g_i^{N_i}e^\varphi, \quad (3.9b)$$

and the solution x_{i+1}^j at the time step t_{i+1} can be found by solving the linear system

$$A \begin{pmatrix} x_{i+1}^2 \\ x_{i+1}^3 \\ \vdots \\ x_{i+1}^{N_i-2} \\ x_{i+1}^{N_i-1} \end{pmatrix} = \begin{pmatrix} -x_i^2 + u_i^2 \\ -x_i^3 + u_i^3 \\ \vdots \\ -x_i^{N_i-2} + u_i^{N_i-2} \\ -x_i^{N_i-1} + u_i^{N_i-1} - \eta_{N_i-1}(s_{N_i} - s_{N_i-1})M_i^{N_i-1}g_{i+1}^{N_i}e^\varphi \end{pmatrix}, \quad (3.10)$$

where A is the tridiagonal matrix

$$\begin{pmatrix} -(\sigma_2 M_i^2 + 1) & \eta_2 M_i^2 & 0 & \cdots & 0 \\ \mu_3 M_i^3 & -(\sigma_3 M_i^3 + 1) & \eta_3 M_i^3 & \cdots & 0 \\ \vdots & \ddots & \ddots & \ddots & \vdots \\ 0 & \cdots & \mu_{N_i-2} M_i^{N_i-2} & -(\sigma_{N_i-2} M_i^{N_i-2} + 1) & \eta_{N_i-2} M_i^{N_i-2} \\ 0 & \cdots & 0 & \mu_{N_i-1} M_i^{N_i-1} & -(\sigma_{N_i-1} M_i^{N_i-1} + 1) \\ & & & & +\eta_{N_i-1} M_i^{N_i-1} \end{pmatrix}. \quad (3.11)$$

3.1.1 Analysis of the Numerical Method

Investigating the consistency, stability, and convergence of the adaptive finite difference method will give insights on how close the numerical solution is to the exact solution. We will analyze the method on a nonadaptive uniform mesh, and switch to an adaptive mesh as necessary. We assume, for a concrete example, that $f = \phi(\epsilon) = k \ln(\epsilon + 1)$.

Letting Δs denote the spatial step size, the discretization of x on a uniform mesh is

$$x_{i+1}^j - x_i^j = \kappa \Delta t \left(\frac{4(x_{i+1}^{j+1} - 2x_{i+1}^j + x_{i+1}^{j-1}))}{(x_i^{j+1} - x_i^{j-1})^2} - \frac{g_{i+1}^{j+1} - g_{i+1}^{j-1}}{g_i^j (x_i^{j+1} - x_i^{j-1})} \right), \quad (3.12)$$

the discretization of ϵ on a uniform mesh is

$$\epsilon_i^j = \left(\frac{x_i^{j+1} - x_i^{j-1}}{2\Delta s} \right) \frac{1}{g_i^j} - 1, \quad (3.13)$$

and the discretization of g on a uniform mesh is the same as in (3.3). Note that the nonuniform discretizations of the previous section do reduce to these discretizations on a uniform mesh.

3.1.1.1 Consistency A way of examining how closely the discretization approximates the exact differential operator is to look at the local truncation error, which is the residual of the difference operator when it is applied to the exact solution. If a numerical method is consistent, then the discretization should become exact as the mesh size, and thus the local truncation error, tends to zero. For our finite difference method, the local truncation error is

$$d_i^j = \frac{x(s_j, t_{i+1}) - x(s_j, t_i)}{\Delta t} - \kappa \left(4 \frac{x(s_{j+1}, t_{i+1}) - 2x(s_j, t_{i+1}) + x(s_{j-1}, t_{i+1}))}{(x(s_{j+1}, t_i) - x(s_{j-1}, t_i))^2} - \frac{g(s_{j+1}, t_{i+1}) - g(s_{j-1}, t_{i+1})}{g(s_j, t_i)(x(s_{j+1}, t_i) - x(s_{j-1}, t_i))} \right). \quad (3.14)$$

Taylor expanding the local truncation error (3.14) about the point (s_j, t_i) , the first fraction is

$$\frac{x(s_j, t_{i+1}) - x(s_j, t_i)}{\Delta t} = \frac{\partial x}{\partial t} + \frac{\Delta t}{2} \frac{\partial^2 x}{\partial t^2} + \text{h.o.t.}, \quad (3.15)$$

where all unspecified evaluations are at the point (s_j, t_i) and “h.o.t.” stands for “higher order terms.” Taylor expanding the numerator of the second fraction in (3.14) we obtain

$$x(s_{j+1}, t_{i+1}) - 2x(s_j, t_{i+1}) + x(s_{j-1}, t_{i+1}) = (\Delta s)^2 \frac{\partial^2 x}{\partial s^2} + \Delta t (\Delta s)^2 \frac{\partial^3 x}{\partial t \partial s^2} + \frac{(\Delta t)^2 (\Delta s)^2}{2} \frac{\partial^4 x}{\partial t^2 \partial s^2} + \frac{(\Delta s)^4}{12} \frac{\partial^4 x}{\partial s^4} + \text{h.o.t.}, \quad (3.16)$$

and the denominator is

$$x(s_{j+1}, t_i) - x(s_{j-1}, t_i) = 2\Delta s \frac{\partial x}{\partial t} + \text{h.o.t.}, \quad (3.17)$$

and thus the second fraction becomes

$$4 \frac{x(s_{j+1}, t_{i+1}) - 2x(s_j, t_{i+1}) + x(s_{j-1}, t_{i+1})}{(x(s_{j+1}, t_i) - x(s_{j-1}, t_i))^2} = \frac{1}{\left(\frac{\partial x}{\partial t}\right)^2} \left(\frac{\partial^2 x}{\partial s^2} + \Delta t \frac{\partial^3 x}{\partial t \partial s^2} + \frac{(\Delta t)^2}{2} \frac{\partial^4 x}{\partial t^2 \partial s^2} + \frac{(\Delta s)^2}{12} \frac{\partial^4 x}{\partial s^4} \right) + \text{h.o.t.} \quad (3.18)$$

Taylor expanding the numerator of the third fraction in (3.14) we obtain

$$g(s_{j+1}, t_{i+1}) - g(s_{j-1}, t_{i+1}) = 2\Delta s \frac{\partial g}{\partial s} + 2\Delta t \Delta s \frac{\partial^2 g}{\partial t \partial s} + (\Delta t)^2 \Delta s \frac{\partial^3 g}{\partial t^2 \partial s} + \frac{(\Delta s)^3}{3} \frac{\partial^3 g}{\partial s^3} + \text{h.o.t.}, \quad (3.19)$$

and using the expansion (3.17) for the denominator, the third fraction becomes

$$\frac{g(s_{j+1}, t_{i+1}) - g(s_{j-1}, t_{i+1})}{g(s_j, t_i) (x(s_{j+1}, t_i) - x(s_{j-1}, t_i))} = \frac{1}{g \frac{\partial x}{\partial t}} \left(\frac{\partial g}{\partial s} + \Delta t \frac{\partial^2 g}{\partial t \partial s} + \frac{(\Delta t)^2}{2} \frac{\partial^3 g}{\partial t^2 \partial s} + \frac{(\Delta s)^2}{6} \frac{\partial^3 g}{\partial s^3} \right) + \text{h.o.t.} \quad (3.20)$$

Substituting the fractions (3.15), (3.18), and (3.20) into the local truncation error (3.14), we obtain

$$\begin{aligned}
d_i^j &= \frac{\partial x}{\partial t} - \underbrace{\kappa \left(\frac{\partial^2 x / \partial s^2}{(\partial x / \partial s)^2} - \frac{\partial g / \partial s}{g(\partial x / \partial t)} \right)}_{= 0 \text{ by (3.5)}} + \frac{\Delta t}{2} \frac{\partial^2 x}{\partial t^2} \\
&\quad - \kappa \left[\frac{1}{\left(\frac{\partial x}{\partial t}\right)^2} \left(\Delta t \frac{\partial^3 x}{\partial t \partial s^2} + \frac{(\Delta t)^2}{2} \frac{\partial^4 x}{\partial t^2 \partial s^2} + \frac{(\Delta s)^2}{12} \frac{\partial^4 x}{\partial s^4} \right) \right. \\
&\quad \left. - \frac{1}{g \frac{\partial x}{\partial t}} \left(\Delta t \frac{\partial^2 g}{\partial t \partial s} + \frac{(\Delta t)^2}{2} \frac{\partial^3 g}{\partial t^2 \partial s} + \frac{(\Delta s)^2}{6} \frac{\partial^3 g}{\partial s^3} \right) \right] + \text{h.o.t.} \\
&= O(\Delta t) + O(\Delta s^2). \tag{3.21}
\end{aligned}$$

This implies that the finite difference method is first-order accurate in time and second-order accurate in space. Hence, the method is consistent because the local truncation error $d_i^j \rightarrow 0$ as $\Delta t \rightarrow 0$ and $\Delta s \rightarrow 0$.

3.1.1.2 Stability A numerical method is stable if small perturbations in the data correspond to small perturbations in the solution, so that numerical errors do not increase unboundedly over time. Most techniques for showing stability are only applicable to linear numerical methods, but we will apply the Fourier Series Method to our nonlinear numerical method to see approximately what behavior we should expect of the numerical solutions. We briefly discuss the Fourier Series Method before applying it; please see, for example, Hall and Porsching [27] for more details.

Any $x \in L_2(0, 2\pi)$ has a unique Fourier series representation in terms of complex exponentials, i.e.,

$$x(s) = \sum_{m=-\infty}^{\infty} \hat{x}(m) e^{ims}, \tag{3.22}$$

where

$$\hat{x}(m) = \frac{1}{2\pi} \int_0^{2\pi} e^{-ims} x(s) ds, \quad m = 0, \pm 1, \dots, \tag{3.23}$$

is its m^{th} Fourier coefficient. Then for $x(\cdot, t) \in L_2(0, 2\pi)$, we can write

$$x(s, t) = \sum_{m=-\infty}^{\infty} \hat{x}(m, t) e^{ims}. \tag{3.24}$$

Let J be a finite nonnegative integer and let a_j , $j = 0, \pm 1, \dots, \pm J$, be $2J + 1$ complex constants. Regarding Δs as a function of Δt , the amplification factors are defined as

$$G(m, \Delta t) = \sum_{j=-J}^J a_j e^{imj\Delta s}, \quad m = 0, \pm 1, \dots, \quad (3.25)$$

and thus

$$\hat{x}(m, t + \Delta t) = G(m, \Delta t) \hat{x}(m, t). \quad (3.26)$$

Characterization of the stability of a numerical method in terms of amplification factors arises from the following theorem.

Theorem 3.1 (von Neumann condition). *A difference method is stable if and only if as $\Delta t \rightarrow 0$, $|G(m, \Delta t)| \leq 1 + O(\Delta t)$, $m = 0, \pm 1, \dots$.*

We will now apply the Fourier Series Method to our nonlinear finite difference method. First consider our numerical method when there is no growth ($\gamma(\epsilon) = 0$), therefore, g is constant so the numerical method is only (3.12) where the second fraction on the right hand side is 0. Let $r = \frac{\Delta t}{(\Delta s)^2}$. Using the notation $x_{i+n}^{j+l} = (s + l\Delta s, t + n\Delta t)$ for $l, n = -1, 0, 1$, and fixing the denominator $A := \left(\frac{x_i^{j+1} - x_i^{j-1}}{\Delta s}\right)^2$, (3.12) becomes

$$x(s, t + \Delta t) - x(s, t) = \frac{4\kappa r}{A} \left(x(s + \Delta s, t + \Delta t) - 2x(s, t + \Delta t) + x(s - \Delta s, t + \Delta t) \right). \quad (3.27)$$

Substituting $x(s, t) = e^{ims}$ and $x(s, t + \Delta t) = G(m, \Delta t)e^{ims}$ into the equation above so that we may solve for $G(m, \Delta t)$, we obtain

$$\begin{aligned} G(m, \Delta t)e^{ims} - e^{ims} &= \frac{4\kappa r}{A} G(m, \Delta t) (e^{im(s+\Delta s)} - 2e^{ims} + e^{im(s-\Delta s)}) \\ \implies G(m, \Delta t) - 1 &= \frac{8\kappa r}{A} G(m, \Delta t) (\cos(m\Delta s) - 1) \\ \implies G(m, \Delta t) &= \frac{1}{1 - \frac{8\kappa r}{A} (\cos(m\Delta s) - 1)}. \end{aligned} \quad (3.28)$$

Noting that $\kappa, r, A > 0$, for any m and Δs we have $|\cos(m\Delta s)| \leq 1$, and thus

$$\begin{aligned} 0 &\leq -\frac{8\kappa r}{A}(\cos(m\Delta s) - 1) \leq \frac{16\kappa r}{A} \\ \implies 1 &\leq 1 - \frac{8\kappa r}{A}(\cos(m\Delta s) - 1) \leq 1 + \frac{16\kappa r}{A} \\ \implies 1 &\geq \frac{1}{1 - \frac{8\kappa r}{A}(\cos(m\Delta s) - 1)} \geq \frac{1}{1 + \frac{16\kappa r}{A}} > 0. \end{aligned} \quad (3.29)$$

This implies that

$$|G(m, \Delta t)| \leq 1, \quad (3.30)$$

for any r , which means that we should expect the numerical method to be unconditionally stable by the von Neumann condition (recalling that our method is nonlinear and the condition only applies to linear methods). Figure 3.5A indicates that the numerical solutions have no instabilities for $\Delta t = 0.0125$ and $\Delta s = 0.0125, 0.00125$.

However, once we add any amount of cell proliferation, we no longer have unconditional stability. Assume for the sake of simplicity that $\gamma(\epsilon) = c$, where $c \in \mathbb{R}$ is a constant. Again, let $r = \frac{\Delta t}{(\Delta s)^2}$, and fix the denominators $A := \left(\frac{x_i^{j+1} - x_i^{j-1}}{\Delta s}\right)^2$ and $B := \frac{g_i^j(x_i^{j+1} - x_i^{j-1})}{(\Delta s)^2}$. Using the notation $x_{i+n}^{j+l} = (s + l\Delta s, t + n\Delta t)$ for $l, n = -1, 0, 1$, (3.12) becomes

$$\begin{aligned} x(s, t + \Delta t) - x(s, t) &= \\ &\frac{4\kappa r}{A} \left(x(s + \Delta s, t + \Delta t) - 2x(s, t + \Delta t) + x(s - \Delta s, t + \Delta t) \right) \\ &\quad - \frac{\kappa r}{B} \left(g(s + \Delta s, t + \Delta t) - g(s - \Delta s, t + \Delta t) \right), \end{aligned} \quad (3.31)$$

and (3.3) becomes

$$g(s, t + \Delta t) = \frac{1}{1 - c\Delta t} g(s, t). \quad (3.32)$$

Substituting $x(s, t) = e^{ims}$, $x(s, t + \Delta t) = G_1(m, \Delta t)e^{ims}$, $g(s, t) = e^{ims}$, and $g(s, t + \Delta t) = G_2(m, \Delta t)e^{ims}$ into the equations above so that we may solve for $G_1(m, \Delta t)$ and $G_2(m, \Delta t)$, we obtain

$$G_1(m, \Delta t) = \frac{1 - \frac{2i\kappa r}{B} \sin(m\Delta s) G_2(m, \Delta t)}{1 - \frac{8\kappa r}{A} (\cos(m\Delta s) - 1)}, \quad (3.33a)$$

$$G_2(m, \Delta t) = \frac{1}{1 - c\Delta t}. \quad (3.33b)$$

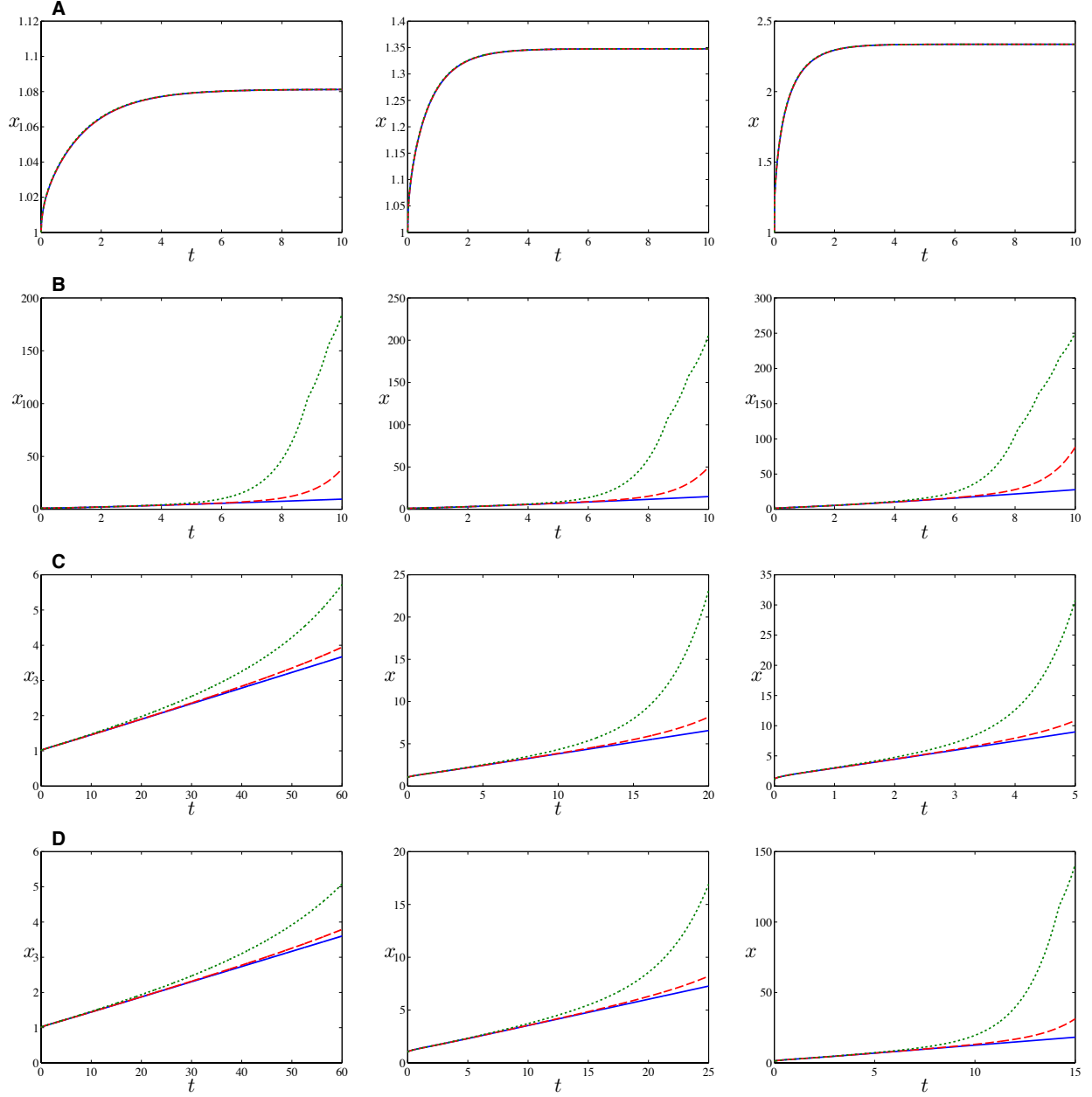


Figure 3.5: *Stability of numerical method for the 1-D model: The position x of the leading edge of cells ($s = 1$) with $\Delta t = 0.0125$ for all plots. The green dotted line is the numerical solution for a uniform mesh with $\Delta s = 0.0125$, the red dashed line is the numerical solution for a uniform mesh with $\Delta s = 0.00125$, and the blue solid line is the numerical solution for an initially uniform mesh with $\Delta s = 0.00125$ and adaptive mesh refinement with the tolerance $TOL = 1.5\Delta s$. In the first column, $k = 0.32$, $b = 1$, $F = 0.025$, in the second column, $k = 0.838$, $b = 1$, $F = 0.25$, and in the third column, $k = 2.947$, $b = 1$, $F = 2.5$. (A) No growth $\gamma(\epsilon) = 0$, (B) constant growth $\gamma(\epsilon) = 1$, (C) linear growth (2.9a), and (D) Fisher growth (2.9b).*

We see that as long as $|c|\Delta t < 1$, approximating by a geometric power series,

$$|G_2(m, \Delta t)| = 1 + c\Delta t + \text{h.o.t.} \leq 1 + O(\Delta t). \quad (3.34)$$

For G_1 we have

$$|G_1(m, \Delta t)|^2 = \frac{1 + \frac{4\kappa^2 r^2 \sin^2(m\Delta s)}{B^2 (1-c\Delta t)^2}}{\left(1 - \frac{8\kappa r}{A} (\cos(m\Delta s) - 1)\right)^2}, \quad (3.35)$$

and this will be less than or equal to 1 if

$$r \geq \frac{\frac{4}{A} (\cos(m\Delta s) - 1)}{\frac{16\kappa}{A^2} (\cos(m\Delta s) - 1)^2 - \frac{\kappa}{B^2} \frac{\sin^2(m\Delta s)}{(1-c\Delta t)^2}}. \quad (3.36)$$

Since the numerator is nonpositive and the denominator can approach zero from the negative side, the lower bound on r could become infinitely large and positive, depending on A and B , parameter $\kappa = \frac{k}{b}$, and growth function γ . This means that we should expect the numerical method to be conditionally stable by the von Neumann condition. However, since A and B are not fixed constants, a uniform mesh may not suffice because the inequality may cease to be satisfied after integrating long enough. Figure 3.5B–D indicates that for various growth functions γ , if the numerical solution is allowed to integrate for a sufficient amount of time, for any uniform spatial mesh, the leading edge of cells will appear to have exponentially increasing velocity. With adaptive mesh refinement as described in Section 3.1, the erroneous exponential movement is eliminated. Hence, adaptive mesh refinement is necessary for stability for the numerical method with nonzero proliferation.

3.1.1.3 Convergence A numerical method is convergent if the numerical solution tends to the exact solution and converges to it as the mesh size goes to zero, and can be shown with the following equivalence theorem.

Theorem 3.2 (Lax equivalence). *If a method is consistent, then it is convergent if and only if it is stable.*

Similar to the Fourier Series Method in the previous section for stability, the Lax equivalence theorem only applies to linear numerical methods. However, even though our method is nonlinear, from the previous two sections we should expect our method without adaptive mesh refinement to be convergent when there is no proliferation since it is consistent and expected to be unconditionally stable. For nonzero proliferation, with adaptive mesh refinement we should expect our method to be convergent since it is consistent and expected to be conditionally stable.

3.2 TRANSVERSE METHOD OF LINES METHOD

We developed an alternative numerical method, a transverse method of lines (TMOL) method, for solving the material formulation ([Model 1](#)) with the intent of focusing on the weaknesses of the nonadaptive finite difference method discussed in the previous section. The TMOL method is a variant of the method of lines in that the semidiscretization is in time first, not space, and the resulting ordinary differential equation is solved in space. The TMOL method is a backward scheme, and since the nonadaptive finite difference method is not truly backward, it is likely that the issues with the step size in time would be avoided. Using the TMOL method results in needing to solve a boundary value problem.

As in the previous section, assume $f = \phi(\epsilon) = k \ln(\epsilon + 1)$, and define parameters $\kappa = \frac{k}{b}$ and $\varphi = \frac{F}{k}$. Let $\Delta t > 0$ be a given step size and $t_i = (i - 1)\Delta t$, $i = 1, 2, 3, \dots$. We first discretize the time derivatives in (2.6) and (2.8) by the forward difference approximations

$$\frac{\partial x(s, t_i)}{\partial t} = \frac{x(s, t_{i+1}) - x(s, t_i)}{\Delta t}, \quad (3.37a)$$

$$\frac{\partial g(s, t_i)}{\partial t} = \frac{g(s, t_{i+1}) - g(s, t_i)}{\Delta t}. \quad (3.37b)$$

Substituting these approximations into the left hand sides of the governing equations (2.6)

and (2.8), and evaluating the right hand sides at the future time step t_{i+1} , we have

$$\frac{x(s, t_{i+1}) - x(s, t_i)}{\Delta t} = \kappa \left(\frac{\frac{\partial^2 x(s, t_{i+1})}{\partial s^2}}{\left(\frac{\partial x(s, t_{i+1})}{\partial s}\right)^2} - \frac{\frac{\partial g(s, t_{i+1})}{\partial s}}{g(s, t_{i+1}) \left(\frac{\partial x(s, t_{i+1})}{\partial s}\right)} \right), \quad (3.38a)$$

$$\frac{g(s, t_{i+1}) - g(s, t_i)}{\Delta t} = \gamma \left(\frac{\partial x(s, t_{i+1})}{\partial s} \frac{1}{g(s, t_{i+1})} - 1 \right) g(s, t_{i+1}). \quad (3.38b)$$

We rewrite x and g as functions of s only, and relabel their time dependence. At time step t_{i+1} , we use the notation $x(s, t_{i+1}) = x_{n+1}(s)$ and $g(s, t_{i+1}) = g_{n+1}(s)$, and at time step t_i , we use the notation $x(s, t_i) = x_n(s)$ and $g(s, t_i) = g_n(s)$. Thus, (3.38) becomes

$$\frac{x_{n+1}(s) - x_n(s)}{\Delta t} = \kappa \left(\frac{x''_{n+1}(s)}{(x'_{n+1}(s))^2} - \frac{g'_{n+1}(s)}{g_{n+1}(s)x'_{n+1}(s)} \right), \quad (3.39a)$$

$$\frac{g_{n+1}(s) - g_n(s)}{\Delta t} = \gamma \left(\frac{x'_{n+1}(s)}{g_{n+1}(s)} - 1 \right) g_{n+1}(s), \quad (3.39b)$$

and rearranging terms we obtain

$$x''_{n+1}(s) - \frac{1}{\kappa \Delta t} (x'_{n+1}(s))^2 (x_{n+1}(s) - x_n(s)) - \frac{g'_{n+1}(s)x'_{n+1}(s)}{g_{n+1}(s)} = 0, \quad (3.40a)$$

$$g_{n+1}(s) \left(1 - \Delta t \gamma \left(\frac{x'_{n+1}(s)}{g_{n+1}(s)} - 1 \right) \right) - g_n(s) = 0. \quad (3.40b)$$

We now rewrite x and g again. At time step n , we rewrite x and g as functions that depend on the previous time step using the notation $x_n(s) = v(t)$ and $g_n(s) = z(t)$. At time step $n+1$, we rewrite x and g as functions that depend on s using the notation $x_{n+1}(s) = y(s)$ and $g_{n+1}(s) = h(s)$. Then (3.40) becomes

$$y''(s) - \frac{1}{\kappa \Delta t} (y'(s))^2 (y(s) - v(t)) - \frac{h'(s)y'(s)}{h(s)} = 0, \quad (3.41a)$$

$$h(s) \left(1 - \Delta t \gamma \left(\frac{y'(s)}{h(s)} - 1 \right) \right) - z(t) = 0, \quad (3.41b)$$

which is a differential algebraic equation.

Writing the second-order differential equation (3.41a) as a system of first-order differential equations with the initial conditions (2.13a) and (2.13b), left boundary condition (2.13c),

right boundary condition (2.13d), and setting $y_3 := h$ to simplify notation, the full differential algebraic equation system is

$$y_1' = y_2, \quad 0 \leq s \leq 1, \quad (3.42a)$$

$$y_2' = \frac{1}{\kappa \Delta t} y_2^2 (y_1 - v) + \frac{y_3'}{y_3} y_2, \quad 0 \leq s \leq 1, \quad (3.42b)$$

$$0 = y_3 \left(1 - \Delta t \gamma \left(\frac{y_2}{y_3} - 1 \right) \right) - z, \quad 0 \leq s \leq 1, \quad (3.42c)$$

$$v(0) = s, \quad z(0) = 1, \quad 0 \leq s \leq 1, \quad (3.42d)$$

$$y_1(0) = 0, \quad y_2(1) = e^\varphi y_3(1), \quad 0 < t. \quad (3.42e)$$

At each time step we numerically solve this system of ordinary differential equations in s in MATLAB using `ode15s`, a function that can be used to solve differential algebraic equations. We rewrite system (3.42) with a singular mass matrix as follows

$$\begin{pmatrix} 1 & 0 & 0 \\ 0 & 1 & -\frac{y_2}{y_3} \\ 0 & 0 & 0 \end{pmatrix} \begin{pmatrix} y_1' \\ y_2' \\ y_3' \end{pmatrix} = \begin{pmatrix} y_2 \\ \frac{1}{\kappa \Delta t} y_2^2 (y_1 - v) \\ y_3 \left(1 - \Delta t \gamma \left(\frac{y_2}{y_3} - 1 \right) \right) - z \end{pmatrix}. \quad (3.43)$$

Recall that $v(t_i) = y_1(s, t_{i-1})$ and $z(t_i) = y_3(s, t_{i-1})$.

A shooting method is implemented to incorporate both boundary conditions. We transform the boundary value problem into an initial value problem by changing boundary conditions (3.42e) to

$$y_1(0) = 0, \quad y_2(0) = \alpha, \quad (3.44)$$

where $\alpha \in \mathbb{R}$ is a value we seek such that the boundary conditions (3.42e) are satisfied within a certain tolerance. To find such an α , at each time step we solve the system of equations for various α and use the secant method to determine if the corresponding solution gives that $y_2(1) - e^\varphi y_3(1)$ is sufficiently close to zero. If the secant method fails after a certain fixed number of iterations, we then use the bisection method which is generally slower but guaranteed to converge to a root.

Unfortunately, the system becomes stiff as $\Delta t \rightarrow 0$. At each time step, `ode15s` solves the system of equations multiple times depending on how many α 's are tested during shooting.

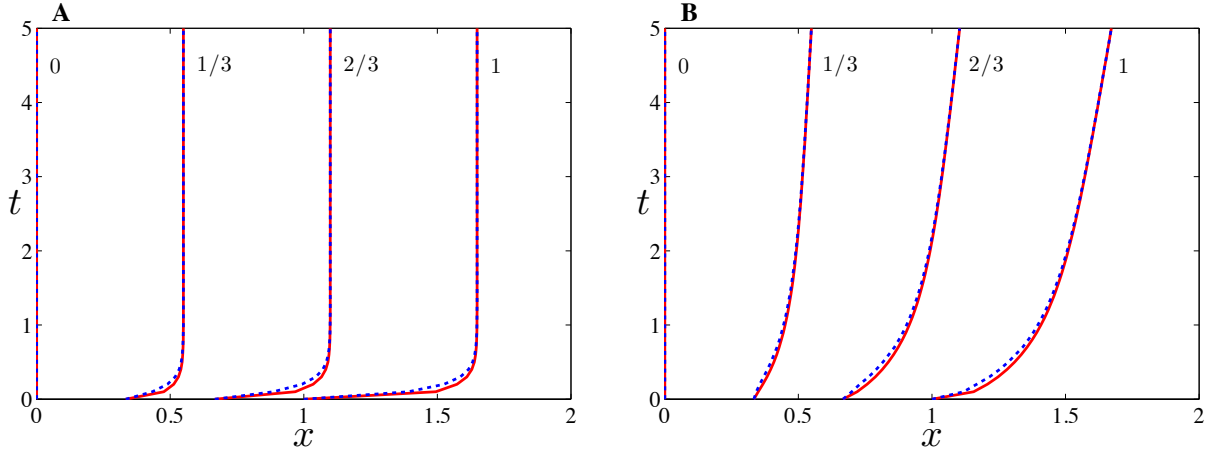


Figure 3.6: Comparison of the transverse method of lines and nonadaptive finite difference methods. Numerical solution of the 1-D one layer model with $\Delta t = 0.1$. The dotted blue curves are the solutions obtained using the transverse method of lines method, and the solid red curves are the solutions obtained using the adaptive finite difference method. Each curve is labeled by its initial position between $[0, 1]$ on the x -axis and represents the path of one cell from where it begins initially to how far right it moves as time increases along the t -axis. (A) $\gamma(\epsilon) = 0$, $\kappa = \frac{k}{b} = 10$, $\varphi = \frac{F}{k} = 0.5$, and (B) $\gamma(\epsilon) = 0.02(\epsilon + 1)$, $\kappa = \frac{k}{b} = 1$, $\varphi = \frac{F}{k} = 0.4$.

For larger Δt , MATLAB issues no warnings but as Δt decreases (the rate of decrease depends on the parameters k , b , and F and the growth function γ), MATLAB outputs the error “Unable to meet integration tolerances without reducing the step size below the smallest value allowed at time t” more often at more time steps, which means that the system is stiff. This implies that parameter choices are limited, in particular since, in effect, Δt is rescaled if k or b is rescaled. Therefore, it is not practical to use the TMOL method. Figure 3.6 shows a comparison of the results that we obtain with the TMOL method and the nonadaptive finite difference method. Both methods give the same qualitative behavior. Thus, the adaptive finite difference method is the best suited for numerically solving the material formulation.

4.0 ANALYTIC SOLUTIONS OF 1-D SINGLE LAYER MODEL

In the previous chapter, numerical solutions of the one-dimensional single layer model gave evidence of a similarity solution under scaling for the model equations without cell proliferation and a traveling wave solution for the model equations with cell proliferation. We first analyze the existence of similarity solutions and then the existence and uniqueness of traveling wave solutions.

4.1 SIMILARITY SOLUTIONS FOR MODEL WITHOUT GROWTH

Although the leading edge eventually stops moving in cell layers of finite size in the absence of proliferation, it continues in semi-infinite layers. In this section, we derive similarity under scaling solutions for such cases. These solutions can be explicitly written in the spatial formulation for one specific elasticity function, and results can be extended to more general elasticity functions in the material formulation.

4.1.1 Spatial Formulation

For analysis of similarity solutions, we consider the spatial formulation ([Model 2](#)) without growth ($q(\rho) = 0$) with logarithmic elasticity function ([2.26a](#)) on a semi-infinite domain $x \in (-\infty, X(t)]$ instead of on a finite domain $x \in [0, X(t)]$, where the original left bound

$x = 0$ identifies with the new left bound $x \rightarrow -\infty$. The system of equations in this case is

$$\frac{\partial \rho(x, t)}{\partial t} = \kappa \frac{\partial^2 \rho}{\partial x^2}, \quad x \leq X(t), 0 \leq t, \quad (4.1a)$$

$$\rho(x, 0) = \rho_0, \quad x \leq X(0), \quad (4.1b)$$

$$\rho(X(t), t) = e^{-\varphi} \rho_0, \quad 0 < t, \quad (4.1c)$$

$$X'(t) = -\kappa \frac{1}{\rho_0} e^{\varphi} \frac{\partial \rho(X(t), t)}{\partial x}, \quad 0 < t, \quad (4.1d)$$

$$\lim_{x \rightarrow -\infty} \rho(x, t) = \bar{\rho}, \quad 0 \leq t, \quad (4.1e)$$

where $\bar{\rho}$ is a limiting density and, as in Section 3.1, we have defined the parameters $\kappa = \frac{k}{b}$ and $\varphi = \frac{F}{k}$.

There is a familiar similarity solution, for example as shown in Section 10.5 of Mattheij et al. [42]. Assuming the scalings $X(t) = \alpha\sqrt{t}$ and $\rho = \rho\left(\frac{x}{\sqrt{t}}\right)$, we find

$$\rho(x, t) = (e^{-\varphi} \rho_0 - \bar{\rho}) \frac{\operatorname{erf}\left(\frac{x}{2\sqrt{\kappa t}}\right) + 1}{\operatorname{erf}\left(\frac{\alpha}{2\sqrt{\kappa}}\right) + 1} + \bar{\rho}, \quad (4.2)$$

where α solves

$$\alpha e^{\alpha^2/(4\kappa)} \left(\operatorname{erf}\left(\frac{\alpha}{2\sqrt{\kappa}}\right) + 1 \right) = \frac{4\kappa(e^{\varphi} \bar{\rho} - \rho_0)}{\rho_0 \sqrt{\pi}}. \quad (4.3)$$

We note that finding the similarity solution under scaling (4.2) required solving an uncoupled system of first-order ordinary differential equations. If we chose a different elasticity function instead of the logarithmic elasticity function (2.26a), then (4.1) would consist of a coupled system of equations. This increases the difficulty of finding a similarity under scaling solution drastically. Thus we turn to the material formulation to analyze the existence of similarity solutions under scaling for more general elasticity functions.

4.1.2 Material Formulation

Consider the material formulation (Model 1) without growth ($\gamma(\epsilon) = 0$) on a semi-infinite domain $s \in (-\infty, 0]$, instead of on the finite domain $s \in [0, 1]$, where the original left bound $s = 0$ identifies with the new left bound $s \rightarrow -\infty$ and the original right bound $s = 1$ identifies with the new right bound $s = 0$. In the absence of cell proliferation, $\hat{s} = s$. The system of equations in this case is

$$\frac{\partial x(s, t)}{\partial s} \frac{\partial x(s, t)}{\partial t} = \frac{1}{b} \frac{\partial f(s, t)}{\partial s}, \quad s \leq 0, 0 \leq t, \quad (4.4a)$$

$$x(s, 0) = s, \quad s \leq 0, \quad (4.4b)$$

$$\lim_{s \rightarrow -\infty} \frac{\partial x(s, t)}{\partial s} = 1, \quad 0 \leq t, \quad (4.4c)$$

$$f(0, t) = F, \quad 0 < t. \quad (4.4d)$$

We look for a similarity solution under scaling of the form

$$x(s, t) = t^\alpha w(z), \quad z = t^{-\beta} s. \quad (4.5)$$

Since the elasticity function ϕ depends on $\epsilon = \frac{\partial x}{\partial s} - 1$ (recall (2.2)) and $\frac{\partial x}{\partial s} = t^{\alpha-\beta} w'$, then

$$\frac{\partial f}{\partial s} = t^{\alpha-2\beta} w'' \Phi(t^{\alpha-\beta} w'), \quad (4.6)$$

where we denote $\Phi(\epsilon) = \frac{d}{d\epsilon} \phi(\epsilon)$ and $' = \frac{d}{dz}$. Plugging the ansatz (4.5) into the governing equation (4.4a), we obtain the second-order ordinary differential equation

$$t^{\alpha-1+\beta} \left(\alpha w(z) - \beta z w'(z) \right) w'(z) = \frac{1}{b} w''(z) \Phi(t^{\alpha-\beta} w'(z)). \quad (4.7)$$

The right boundary condition (4.4d) implies $t^{\alpha-\beta} w'(0) = \phi^{-1}(F) + 1$. Since both $w'(0)$ and $\phi^{-1}(F)$ are constants and $w'(0) \neq 0$ by (4.4b), then $t^{\alpha-\beta}$ must be a constant and hence $\alpha = \beta$. Then (4.7) becomes

$$\alpha t^{2\alpha-1} \left(w(z) - z w'(z) \right) w'(z) = \frac{1}{b} w''(z) \Phi(w'(z)). \quad (4.8)$$

To remove t -dependence, no matter the constitutive assumption for ϕ , either $w'(z) = 0$, $w(z) = z w'(z)$, or $\alpha = \frac{1}{2}$. If $w'(z) = 0$, then the solution x does not depend on s , and if

$w(z) = zw'(z)$, then the solution x does not depend on t . Therefore, $\alpha = \frac{1}{2}$ and the system (4.4) has a similarity solution under scaling of the form

$$x(s, t) = \sqrt{t}w(z), \quad z = \frac{s}{\sqrt{t}}, \quad (4.9)$$

where $w(z)$ is a solution of the second-order ordinary differential equation

$$w''(z) + \frac{b}{2\Phi(w'(z))} (zw'(z) - w(z)) = 0. \quad (4.10)$$

Setting $y := w'$, this becomes a nonautonomous system of first-order ordinary differential equations

$$w' = y, \quad (4.11a)$$

$$y' = \frac{b}{2\Phi(y)} (w - zy)y, \quad (4.11b)$$

subject to the boundary conditions

$$y(0) = \phi^{-1}(F), \quad (4.12a)$$

$$\lim_{z \rightarrow -\infty} y(z) = 1. \quad (4.12b)$$

Figure 4.1A shows a numerical solution of (4.11)–(4.12) with logarithmic elasticity function (2.3a), solved via XPPAUT. Figure 4.1B shows this solution compared to the solution obtained using the adaptive finite difference method as described in Section 3.1. Since the solution using the adaptive finite difference method is on a finite domain but the similarity under scaling solution is on a semi-infinite domain, the solutions match for t not too large.

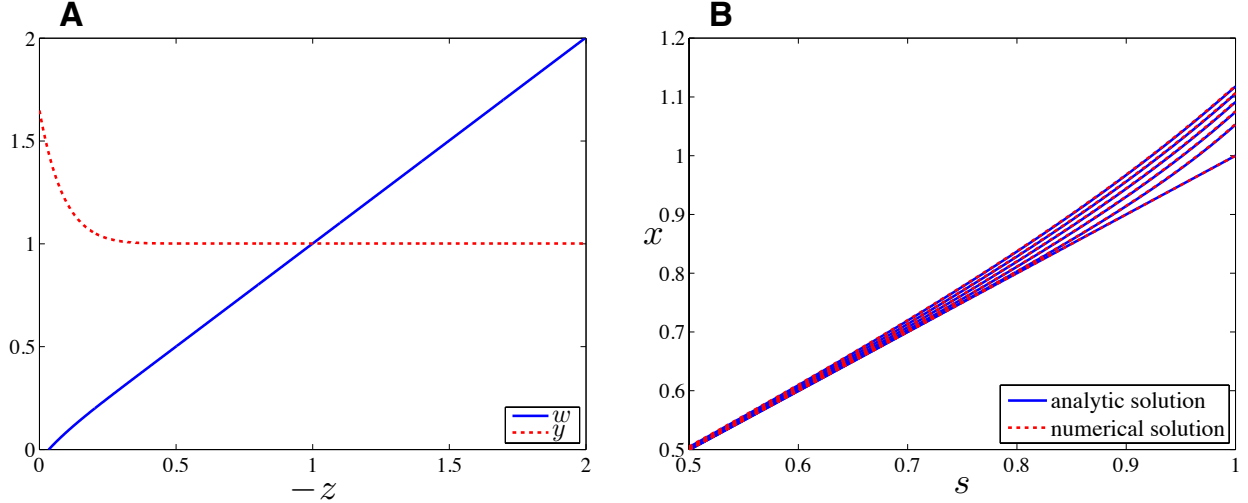


Figure 4.1: Similarity solution under scaling of the material formulation with no growth $\gamma(\epsilon) = 0$, $k = 0.01$, $b = 1$, and $F = 0.005$. (A) Solution of the boundary value problem (4.11)–(4.12) in the z coordinate. (B) The numerical solution of (2.6), (2.9), and (2.13), using the adaptive finite difference method, is plotted against the analytic solution of the boundary value problem (4.11)–(4.12) for $t = 0, 1, 2, 3, 4, 5$ hours.

4.2 TRAVELING WAVE SOLUTIONS FOR MODEL WITH GROWTH

The classical example of a problem with a traveling wave solution is the Fisher-Kolmogorov equation on an infinite domain. We observe that with logarithmic elasticity function (2.26a) and Fisher growth function (2.35b), the governing equation of the spatial formulation (2.20) is the same as the Fisher-Kolmogorov equation. However, the spatial formulation is a free boundary problem and we cannot identify its finite domain with an infinite domain, so the results from the classical Fisher-Kolmogorov traveling wave analysis do not apply. In this section, we analyze the existence and uniqueness of traveling wave solutions for the spatial formulation for general elasticity and nonzero cell proliferation rate functions. Due to the nonlinearity of the governing equation, traveling wave analysis for the material formulation is very difficult.

Consider the spatial formulation (Model 2) on a semi-infinite domain $x \in (-\infty, X(t)]$

instead of on a finite domain $x \in [0, X(t)]$. The system of equations in this case is

$$\frac{\partial \rho}{\partial t} = \frac{1}{b} \frac{\partial}{\partial x} \left(\rho p'(\rho) \frac{\partial \rho}{\partial x} \right) + q(\rho), \quad x \leq X(0), 0 \leq t \quad (4.13a)$$

$$\rho(x, 0) = \rho_0, \quad x \leq X(0), \quad (4.13b)$$

$$p(\rho(X(t), t)) = -F, \quad 0 < t, \quad (4.13c)$$

$$X'(t) = -\frac{1}{b} p'(\rho(X(t), t)) \frac{\partial \rho(X(t), t)}{\partial x}, \quad 0 < t, \quad (4.13d)$$

$$\lim_{x \rightarrow -\infty} \rho(x, t) = \bar{\rho}, \quad 0 \leq t, \quad (4.13e)$$

where $\bar{\rho}$ is a limiting density and a root of q , and thus a density at which there is no growth.

In our analysis, we assume the condition

$$q'(\bar{\rho}) < 0. \quad (4.14)$$

Recall that $X(t)$ is the position of the leading edge and condition (4.13d) is the Stefan condition for the speed of the propagation of the free boundary.

We look for a traveling wave solution of the form

$$\rho(x, t) = \rho(z), \quad z = x - ct, \quad (4.15)$$

where c is the speed of the traveling wave. We assume $c \geq 0$ to examine the closure of a cell layer gap. Substituting (4.15) into the governing equation (4.13a), we obtain the second-order ordinary differential equation

$$(\rho p'(\rho) \rho')' + cb\rho' + bq(\rho) = 0, \quad (4.16)$$

where $' = \frac{d}{dz}$. Setting $y := \rho'$, this becomes a system of first-order ordinary differential equations

$$\rho' = y, \quad (4.17a)$$

$$y' = \frac{-1}{p'(\rho)\rho} \left((p'(\rho)\rho)' y + cby + bq(\rho) \right), \quad (4.17b)$$

which is subject to the conditions

$$\rho(0) = \rho_F = p^{-1}(-F), \quad (4.18a)$$

$$y(0) = y_F = \frac{-cb}{p'(\rho_F)}, \quad (4.18b)$$

$$\lim_{z \rightarrow -\infty} (\rho(z), y(z)) = (\bar{\rho}, 0), \quad (4.18c)$$

where $^{-1}$ denotes the inverse.

The limit point $(\bar{\rho}, 0)$ in (4.18c) is a fixed point of the system (4.17). Recalling the inequalities (2.18d) and (4.14), the determinant of the Jacobian evaluated at $(\bar{\rho}, 0)$ is $\frac{bq'(\bar{\rho})}{p'(\bar{\rho})\bar{\rho}} < 0$, which implies that $(\bar{\rho}, 0)$ is a saddle point, and hence the boundary value problem (4.17)–(4.18) has a solution. Note that if $q'(\bar{\rho}) > 0$ instead of condition (4.14), the point $(\bar{\rho}, 0)$ is a center or an attractor and no traveling wave solution exists.

We will use phase plane analysis to identify traveling wave solutions. In particular, a traveling wave solution is given by the portion of the unstable manifold connecting the saddle point $(\bar{\rho}, 0)$ and its intersection with the curves $\{\rho = \rho_F\}$ and $\left\{y = \frac{-cb}{p'(\rho)}\right\}$ in the ρy -plane for a particular wave speed c . We first examine stationary waves, which occur when $c = 0$, before examining the case when $c > 0$.

4.2.1 Stationary Waves

To find stationary wave solutions of (4.17)–(4.18), we set $c = 0$. System (4.17) with $c = 0$ is conservative with energy

$$E(\rho, y) = \frac{y^2}{2} - \frac{b}{(p'(\rho)\rho)^2} \int_{\rho}^{\bar{\rho}} \alpha p'(\alpha) q(\alpha) d\alpha, \quad (4.19)$$

which is constant along any trajectory. In view of the boundary conditions (4.18), we seek the level set through the points $(\bar{\rho}, 0)$ and $(\rho_F, 0)$ for which $E(\bar{\rho}, 0) = 0$. It follows that we require

$$E(\rho_F, 0) = \frac{b}{(p'(\rho_F)\rho_F)^2} \int_{\bar{\rho}}^{\rho_F} \alpha p'(\alpha) q(\alpha) d\alpha = 0. \quad (4.20)$$

Another way to state this condition is as follows. Let $\hat{\rho}$ be the largest number smaller than $\bar{\rho}$ such that $E(\hat{\rho}, 0) = 0$. Also assume there exists a trajectory of (4.17) that terminates at

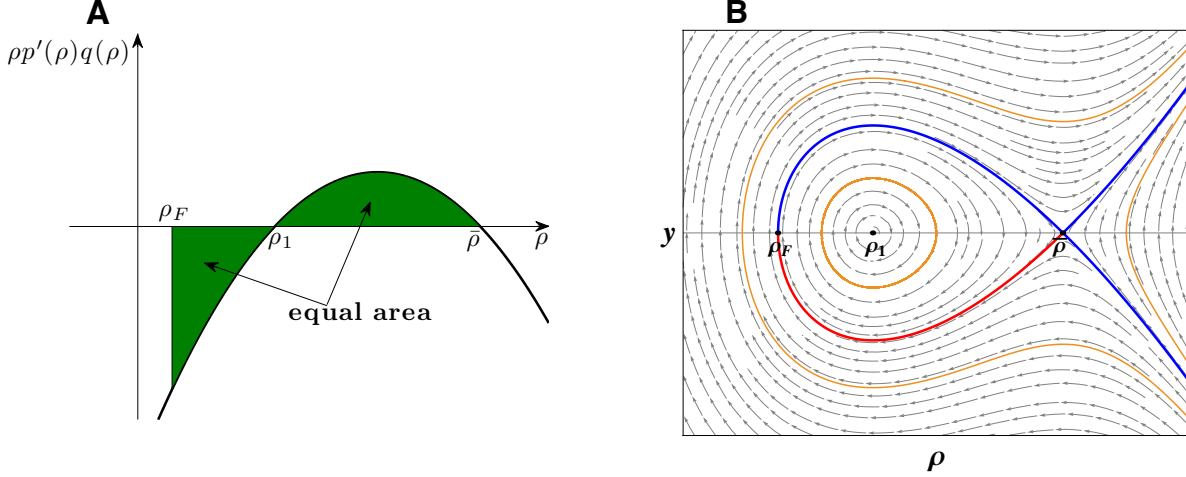


Figure 4.2: *Stationary wave solutions of the spatial formulation with growth: (A) In order to have stationary waves, the plot of $\rho p'(\rho)q(\rho)$ must be of this form, where there is equal area under the curve on the intervals $[\rho_F, \rho_1]$ and $[\rho_1, \bar{\rho}]$ and the slope is positive at ρ_1 and negative at $\bar{\rho}$. (B) The phase portrait for (4.17) with $c = 0$ has a center at $(\rho_1, 0)$. The blue lines denote the stable and unstable manifolds of the saddle point $(\bar{\rho}, 0)$. The orange lines denote sample trajectories. The red line denotes the stationary wave solution, which is the portion of the unstable manifold between the points $(\bar{\rho}, 0)$ and $(\rho_F, 0)$.*

$(\hat{\rho}, 0)$ and converges to $(\bar{\rho}, 0)$ as $z \rightarrow -\infty$. Then the boundary value problem (4.17)–(4.18) has a stationary solution if $p(\hat{\rho}) = -F$.

Suppose that $0 < \rho_F < \bar{\rho}$. One example for which (4.20) is satisfied, assuming (2.18d), is when there exists another fixed point of q , say ρ_1 , such that

$$\rho_F < \rho_1 < \bar{\rho}, \quad (4.21a)$$

$$q(\rho_1) = 0, \quad (4.21b)$$

$$q(\rho_F) < 0, \quad (4.21c)$$

$$-\int_{\rho_F}^{\rho_1} \alpha p'(\alpha)q(\alpha) d\alpha = \int_{\rho_1}^{\bar{\rho}} \alpha p'(\alpha)q(\alpha) d\alpha. \quad (4.21d)$$

In such a case, the graph of $\rho p'(\rho)q(\rho)$ is of the form in Figure 4.2A. Furthermore, in the phase portrait of the system, $(\rho_1, 0)$ is a center, and a sketch looks like Figure 4.2B.

4.2.2 Traveling Waves

To find traveling wave solutions of (4.17)–(4.18), we set $c > 0$, which corresponds to the direction of motion toward a cell layer gap, i.e. the direction of positive x . The solution is a segment of the unstable manifold of the saddle point $(\bar{\rho}, 0)$ that terminates at the point (ρ_F, y_F) given by (4.18a)–(4.18b). We find this solution by varying the wave speed c , which affects both the unstable manifold and y_F . Let $y^u(\rho, c)$ be a function describing such a manifold, defined for $\rho \in [\hat{\rho}, \bar{\rho}]$ and $c \geq 0$, where $\hat{\rho}(c)$ is the value of ρ at which the unstable manifold first intersects the ρ -axis (if the unstable manifold does not intersect the ρ -axis, then we set $\hat{\rho}(c) = 0$).

For $c = 0$, we have an explicit formula for y^u , in view of (4.19),

$$y^u(\rho, 0) = \frac{-1}{p'(\rho)\rho} \sqrt{2b \int_{\rho}^{\bar{\rho}} \alpha p'(\alpha) q(\alpha) d\alpha}. \quad (4.22)$$

For $c > 0$, the unstable manifold function y^u is a solution of the integral equation

$$y^u(\rho, c) = \int_{\rho}^{\bar{\rho}} \frac{1}{p'(\alpha)\alpha} \left((p'(\alpha)\alpha)' + b \frac{q(\alpha)}{y^u(\alpha, c)} \right) d\alpha. \quad (4.23)$$

Of course, such a solution may not exist for all wave speeds c , so we examine the conditions for existence and uniqueness of solutions and their dependence on the elasticity function $p(\rho)$, growth function $q(\rho)$, and parameter F . The parameter $b > 0$ is assumed fixed.

First, consider when $q(\rho) > 0$ for $0 < \rho < \bar{\rho}$. In this case, there is no homoclinic orbit in the phase portrait of the system when $c = 0$, and hence the boundary value problem (4.17)–(4.18) has no stationary solutions.

Theorem 4.1. *Let $\bar{\rho}$ be such that $q(\bar{\rho}) = 0$, $q'(\bar{\rho}) < 0$, and $q(\rho) > 0$ for $\rho \in [0, \bar{\rho})$. Then for any $F > 0$ such that $\rho_F = p^{-1}(-F) \in (0, \bar{\rho})$, there exists a unique $c(F) > 0$ for which the boundary value problem (4.17)–(4.18) has a solution, and that solution is unique.*

Proof. Let $F > 0$ be such that $\rho_F = p^{-1}(-F) \in (0, \bar{\rho})$. The boundary value problem (4.17)–(4.18) has a solution for some $c \geq 0$ if there is a trajectory of (4.17) that terminates at (ρ_F, y_F) and converges to $(\bar{\rho}, 0)$ as $z \rightarrow -\infty$, i.e. if $y^u(\rho_F, c) = y_F$, where y^u is defined by (4.22)–(4.23). We now examine how the unstable manifold depends on c .

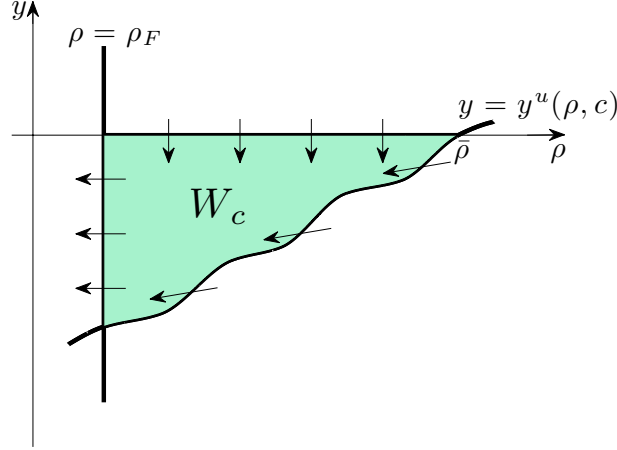


Figure 4.3: The set W_c in the proof of Theorem 4.1 is bounded by the ρ -axis, the vertical line $\{\rho = \rho_F\}$, and the unstable manifold of the saddle point $(\bar{\rho}, 0)$, $y^u(\rho, c)$. The arrows indicate the direction of the flow with $c^* > c$.

For any $c \geq 0$, let W_c be the closed set in the ρy -plane bounded by the lines $\{y = 0\}$ and $\{\rho = \rho_F\}$ and the curve $\{y = y^u(\rho, c)\}$ (see Figure 4.3). Since $q(\rho)$ is positive for $\rho \in [0, \bar{\rho})$, there are no other fixed points in W_c besides $(\bar{\rho}, 0)$. The line $\{y = 0\}$ is the ρ -nullcline and the flow across this line is in the negative y -direction for $\rho \in [0, \bar{\rho})$ (recall equation (2.18d)). For $y < 0$, the flow across the line $\{\rho = \rho_F\}$ is in the negative ρ -direction. The direction field has the slope

$$\frac{y'}{\rho'} = \frac{-1}{p'(\rho)\rho} \left((p'(\rho)\rho)' + cb + b \frac{q(\rho)}{y} \right). \quad (4.24)$$

Fix c and consider any $c^* > c$. The slope at any point $(\rho, y^u(\rho, c))$ with $\rho \in [\rho_F, \bar{\rho})$ is strictly smaller than the slope of $y^u(\rho, c)$ when considering the flow with c^* . Hence, for $c^* > c$, the flow will enter W_c across $y^u(\rho, c)$ (see Figure 4.3).

Furthermore, the eigenvector associated with the positive eigenvalue of the linearized system at $(\bar{\rho}, 0)$ is given by

$$\begin{pmatrix} 1 \\ \frac{-cb}{2p'(\bar{\rho})\bar{\rho}} + \frac{1}{2} \sqrt{\left(\frac{cb}{p'(\bar{\rho})\bar{\rho}} \right)^2 - 4b \frac{q'(\bar{\rho})}{p'(\bar{\rho})\bar{\rho}}} \end{pmatrix}, \quad (4.25)$$

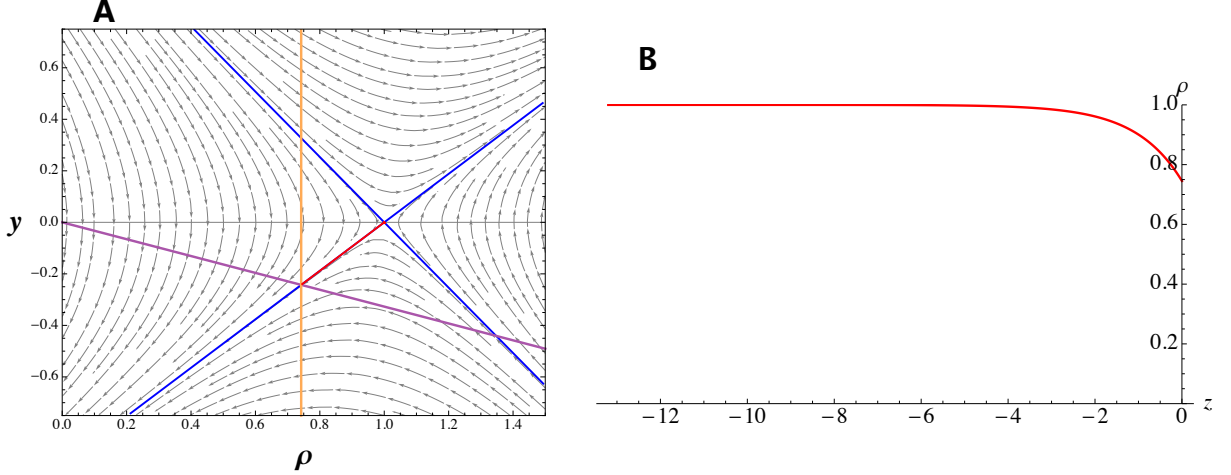


Figure 4.4: Linear growth function (2.9a) is an example of a function that satisfies the conditions of Theorem 4.1 with logarithmic elasticity function (2.3a). Here, $k = 0.838$, $b = 1$, $F = 0.25$, $\bar{\rho} = \rho_0 = 1$, and speed $c = 0.274120$. (A) The phase portrait of the system with the unstable and stable manifolds of the saddle point in blue, the line $\{\rho = \rho_F\}$ in orange, the curve $\left\{y = \frac{-cb}{p'(\rho)}\right\}$ in purple, and the solution trajectory in red. (B) The traveling wave profile of the solution trajectory in traveling wave coordinate z . cf. Figure 3.2A.

and its slope decreases as c increases from 0. Therefore, for any $c^* > c \geq 0$, the unstable manifold $y^u(\rho, c^*)$ enters W_c at the point $(\bar{\rho}, 0)$ and exits W_c across the line $\{\rho = \rho_F\}$. Since $\rho' < 0$ in W_c , the unstable manifold $y^u(\rho, c^*)$ exits W_c at a unique point $(\rho_F, y^u(\rho_F, c^*))$, where $y^u(\rho_F, c^*) > y^u(\rho_F, c)$.

Consequentially, $y^u(\rho_F, c)$ is a continuous monotonically increasing function of c . Recall from (4.18b) that $y_F = \frac{-cb}{p'(\rho_F)}$, and hence $y_F(c)$ continuously monotonically decreases with c such that $y_F(0) = 0 > y^u(\rho_F, 0)$ and $y_F \rightarrow -\infty$ as $c \rightarrow \infty$. By the Intermediate Value Theorem and monotonicity of the two functions, there exists a unique c at which $y^u(\rho_F, c) = y_F(c)$. In addition, for such c , there is a unique trajectory that terminates at (ρ_F, y_F) and converges to $(\bar{\rho}, 0)$ as $z \rightarrow -\infty$, implying that there exists a unique solution of the boundary value problem (4.17)–(4.18). ■

The linear (2.9a) and Fisher (2.9b) growth functions are examples of growth functions that satisfy the conditions of Theorem 4.1. Figure 4.4 illustrates the phase portrait and trav-

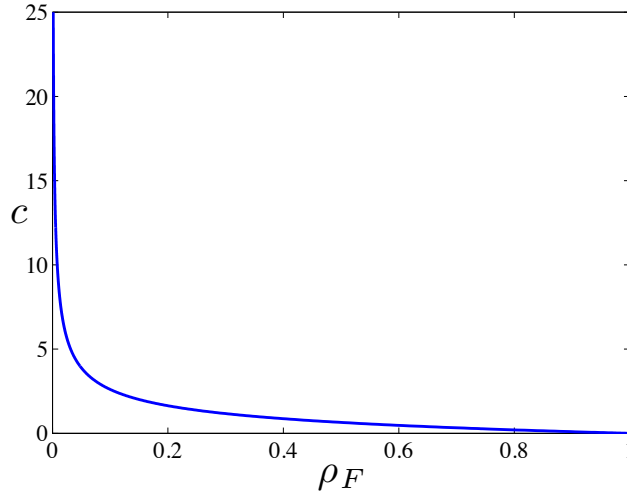


Figure 4.5: The bifurcation diagram for the linear growth function (2.9a) with logarithmic elasticity function (2.3a) and parameters as in Figure 4.4. Values of ρ_F and c that lie along the curve result in unique traveling waves.

eling wave solution profile for the linear growth function and logarithmic elasticity function (2.3a). The bifurcation diagram with c as the varying parameter is illustrated in Figure 4.5, where the curve represents pairs of c and ρ_F for which a solution exists.

We now examine when the phase portrait of the system for a given growth function q has a homoclinic orbit when $c = 0$.

Theorem 4.2. *Let $\bar{\rho}$ be such that $q(\bar{\rho}) = 0$ and $q'(\bar{\rho}) < 0$, and let $\hat{\rho}$ be the smallest non-negative number such that $\int_{\eta}^{\bar{\rho}} q(\alpha) d\alpha \geq 0$ for $\eta \in [\hat{\rho}, \bar{\rho})$. Then for any $F > 0$ such that $\rho_F = p^{-1}(-F) \in [\hat{\rho}, \bar{\rho})$, there exists a $c(F) > 0$ for which the boundary value problem (4.17)–(4.18) has a solution.*

Proof. The proof is identical to that of Theorem 4.1 except that the flow across the nullcline $\{y = 0\}$ is no longer in the negative y -direction for all $\rho \in (\rho_F, \bar{\rho})$, and hence for $c^* > c$ the unstable manifold can exit the domain W_c along the ρ -axis. As a result, there is a limited range $[0, c^\dagger]$ of c for which the unstable manifold intersects the line $\{\rho = \rho_F\}$, but, nonetheless, the functions $y^u(\rho_F, c)$ and $y_F(c)$ (defined as in the proof of Theorem 4.1) are

monotone and intersect at a value $c \in [0, c^\dagger]$. ■

The difference in this case is that the solution to the boundary value problem may not be unique. The conditions of the theorem admit that there be at least one other root $\rho_1 < \bar{\rho}$ of the function q which gives rise to a stable spiral fixed point of the system. In that case, the unstable manifold may converge to that fixed point in the limit as $z \rightarrow -\infty$ and intersect the curves $\{\rho = \rho_F\}$ and $\left\{y = y_F(c) = \frac{-cb}{p'(\rho_F)}\right\}$ for more than one c .

Figure 4.6 illustrates some of the phase portraits and traveling wave solution profiles for the cubic growth function (2.9c), which satisfies the conditions of Theorem 4.2, and logarithmic elasticity function (2.3a). Four possible solutions are shown, and as c decreases, the solution trajectory winds about the spiral fixed point. For any growth function that satisfies the conditions of Theorem 4.2, there exists an upper bound for a countably infinite number of c in which the boundary value problem (4.17)–(4.18) has a solution. Figure 4.7 illustrates the bifurcation diagram with c as the varying parameter, where the curves represent pairs of c and ρ_F for which a solution exists.

Several additional results can be obtained.

Proposition 4.1. *Suppose the hypotheses of Theorem 4.2 are satisfied with $\hat{\rho} > 0$. Then there exists a $c^* < \infty$ such that any solution of boundary value problem (4.17)–(4.18) with $\rho_F \in [\hat{\rho}, \bar{\rho})$ has $c(F) < c^*$.*

Proof. Let $c^* > \sqrt{\frac{2}{b} \int_{\hat{\rho}}^{\bar{\rho}} \alpha p'(\alpha) q(\alpha) d\alpha}$ for all $\rho \in [\hat{\rho}, \bar{\rho}]$. Then the curve $\left\{y = y_F(c) = \frac{-cb}{p'(\rho_F)}\right\}$ does not intersect $y^u(\rho, 0)$ at any $\rho \in (\hat{\rho}, \bar{\rho})$. Furthermore, that curve does not intersect $y^u(\rho, c)$ at any $\rho \in (\hat{\rho}, \bar{\rho})$ for any $c \geq c^*$. Solutions of the boundary value problem cannot exist with $c \geq c^*$ for any $\rho_F \in (\hat{\rho}, \bar{\rho})$. ■

Proposition 4.2. *If $\hat{\rho} > 0$, the number of $c(F)$ for which the boundary value problem (4.17)–(4.18) has a solution is countably infinite for all $\rho_F \in [\hat{\rho}, \bar{\rho})$.*

Proof. Let $0 \leq c < c^*$. Let $\{Z_i(c)\}_{i=1}^\infty$, where $-\infty < Z_1(c) < Z_2(c) < Z_3(c) < \dots$, be the sequence of values of z at which the unstable manifold intersects the ρ -axis. Let $I_1 = (-\infty, Z_1(c)]$ and $I_i = [Z_{i-1}(c), Z_i(c)]$, for $i = 2, 3, \dots$. Denote the unstable manifold for $z \in I_i$ as the function $y_i^u(\rho, c)$, for $i \in \mathbb{N}$. By properties of the flow, $y_i^u(\rho, c) \geq 0$ for i

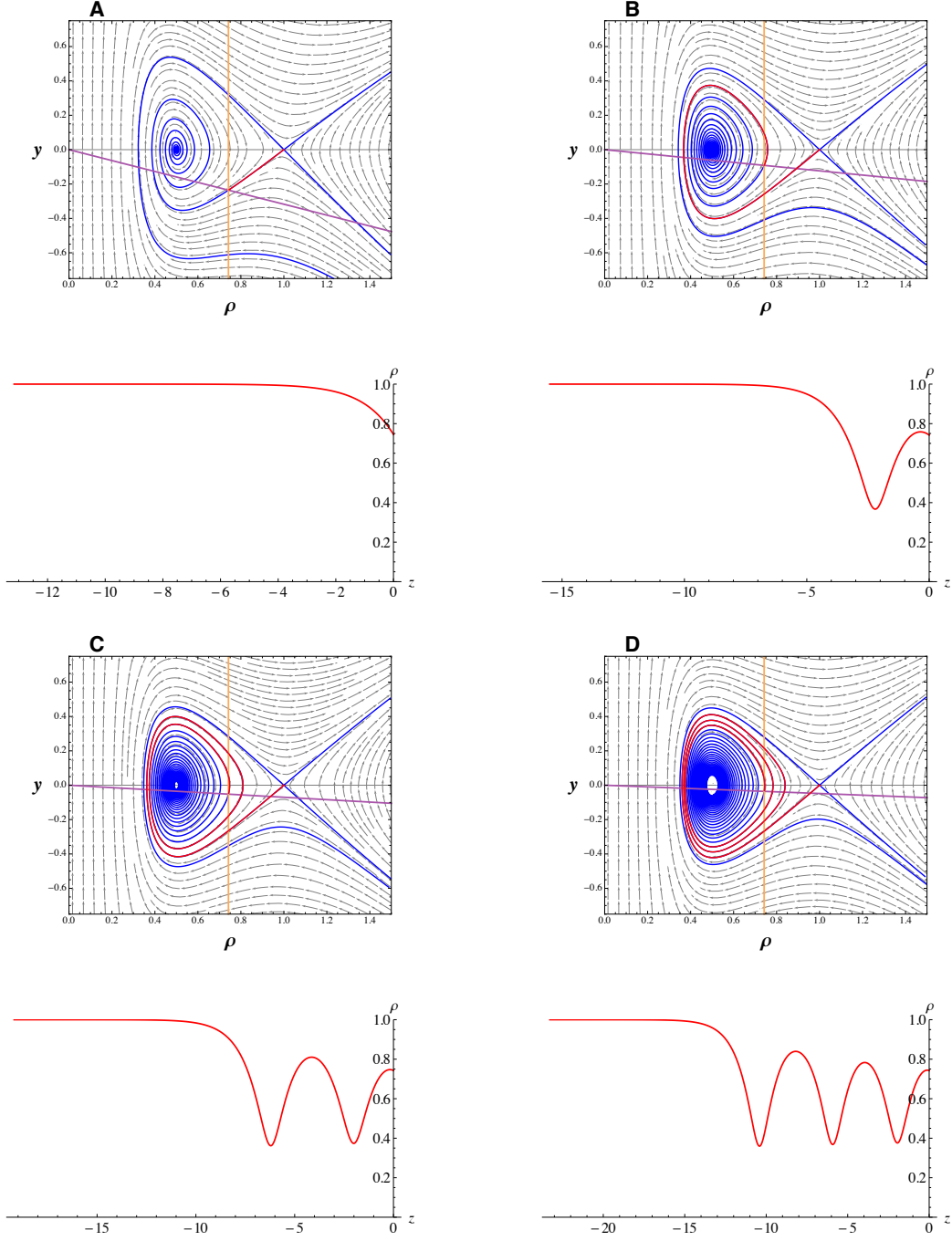


Figure 4.6: Cubic growth function (2.9c) is an example of a function that satisfies the conditions of Theorem 4.2 with logarithmic elasticity function (2.3a). Here, $k = 0.838$, $b = 1$, $F = 0.25$, $\bar{\rho} = \rho_0 = 1$ and speed (A) $c = 0.266062$, (B) $c = 0.103310$, (C) $c = 0.0587513$, and (D) $c = 0.0404030$. First row: The phase portrait of the system with the unstable and stable manifolds of the saddle point in blue, the line $\{\rho = \rho_F\}$ in orange, the curve $\left\{y = \frac{-cb}{p'(\rho)}\right\}$ in purple, and the solution trajectory in red. Second row: Respectively, the traveling wave profile of the solution trajectory in traveling wave coordinate z . cf. Figure 3.4A.

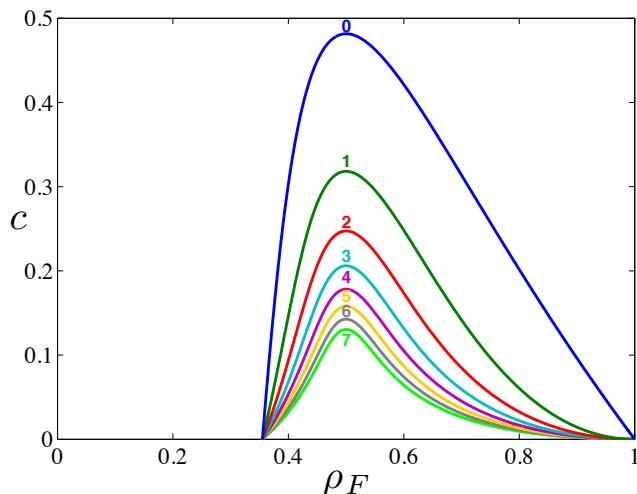


Figure 4.7: *The bifurcation diagram for the cubic growth function (2.9c) with logarithmic elasticity function (2.3a) and parameters as in Figure 4.6. Values of ρ_F and c that lie along the curves result in solutions of the boundary value problem. The number of loops that the solution trajectory traverses about the stable spiral is labeled. Note that only a portion of the countably infinite number of curves is shown.*

even and $y_i^u(\rho, c) \leq 0$ for i odd. For i odd and c sufficiently small, $y_i^u(\rho_F, c) = y_F$. Hence the trajectory $y^u(\rho, c)$ with $z \in (-\infty, Z_i(c)]$, i odd, terminates at (ρ_F, y_F) and converges to $(\bar{\rho}, 0)$ as $z \rightarrow -\infty$, implying that there exists a countably infinite number of solutions of the boundary value problem (4.17)–(4.18). ■

If $\hat{\rho} = 0$ in the statement of Theorem 4.2, the number of solutions of the boundary value problem (4.17)–(4.18) is no longer countably infinite, but finite. Since ρ is the cell density, any physically relevant solution requires $\rho \geq 0$, and thus solution trajectories cannot traverse loops about the stable spiral if they cross the y -axis. Hence in this case, for any $\rho_F \in (0, \bar{\rho})$, there will be a finite number of speeds c for which the boundary value problem (4.17)–(4.18) has a solution. If the other fixed point of the system (see (4.21)) is nonpositive, then there is a unique speed c and there does not exist an upper bound on the speed c for which there is a solution. Two example growth functions are $q(\rho) = (\rho_0 - \rho)(\rho_0 + 4\rho)$ and $q(\rho) = -(\rho_0 - \rho)(\rho_0 - 4\rho)$.

Now let us examine how many solutions exist for the case when q has three roots $\rho_2 < \rho_1 < \rho_0$, such that in the phase portrait, ρ_0 and ρ_2 are saddle points and ρ_1 is a stable spiral or node for sufficiently large c . Therefore, $\bar{\rho}$ may be either ρ_0 or ρ_2 . First consider $0 < \rho_2 < \rho_1 < \rho_0$. There are two possible flavors of phase portraits, one such that a heteroclinic orbit may exist in the lower half of the $y\rho$ -plane and one such that a heteroclinic orbit may exist in the upper half of the $y\rho$ -plane.

If $\int_{\rho}^{\rho_0} q(\alpha)d\alpha > 0$ for all $\rho \in (0, \rho_0)$, then there exists a $c^* \in \mathbb{R}$ such that a heteroclinic orbit in the lower half of the $y\rho$ -plane connects the two saddle points ρ_0 and ρ_2 . Assuming $\bar{\rho} = \rho_0$, there is a finite number of solutions for $\rho_F \in (0, \rho_0)$. Assuming $\bar{\rho} = \rho_2$, for $c = 0$ there will exist a stationary wave solution if ρ_F satisfies $\int_{\rho_2}^{\rho_F} q(\alpha)d\alpha = 0$. For $c > 0$, there are a countably infinite number of solutions for $\rho_F \in (\rho_2, \eta)$ where η satisfies $\int_{\rho_2}^{\eta} q(\alpha)d\alpha = 0$. An example growth function is $q(\rho) = (\rho_0 - \rho)(\rho_0 - 2\rho)(\rho_0 - 4\rho)$, and Figure 4.8 illustrates some of its corresponding phase portraits and traveling wave solution profiles. Figure 4.9 illustrates the bifurcation diagram with c as the varying parameter, where the curves represent pairs of c and ρ_F for which a solution exists.

If $\int_{\rho}^{\rho_0} q(\alpha)d\alpha < 0$ for some $\rho \in (0, \rho_0)$, then there exists a $c^* \in \mathbb{R}$ such that a heteroclinic orbit in the upper half of the $y\rho$ -plane connects the two saddle points ρ_0 and ρ_2 , which cannot result in a solution assuming $c > 0$. Assuming $\bar{\rho} = \rho_0$, there exists a countably infinite number of solutions for $\rho_F \in (\eta, \rho_0)$ where η satisfies $\int_{\eta}^{\rho_0} q(\alpha)d\alpha = 0$, and there exists an upper bound on the speed c for which there is a solution. Assuming $\bar{\rho} = \rho_2$, for $0 \leq c \leq c^*$ there are no solutions, but for $c > c^*$ there are at most a countably infinite number of solutions for $\rho_F \in (\eta, \rho_0)$. An example growth function is $q(\rho) = (\rho_0 - \rho)(\rho_0 - 8\rho)(3\rho_0 - 5\rho)$, and Figures 4.11–4.12 illustrate some of the phase portraits and traveling wave solution profiles. Figure 4.10 illustrates the bifurcation diagram with c as the varying parameter, where the curves represent pairs of c and ρ_F for which a solution exists.

The case when $\rho_2 < 0 < \rho_1 < \rho_0$ or $\rho_2 < \rho_1 < 0 < \rho_0$ is similar to the case just described when $0 < \rho_2 < \rho_1 < \rho_0$, except we can no longer have $\bar{\rho} = \rho_2$. The number of solutions for these cases with $\bar{\rho} = \rho_0$ will be less than or equal to the number of solutions for the case when $0 < \rho_2 < \rho_1 < \rho_0$ because physically relevant solutions require $\rho \geq 0$ and solution trajectories cannot cross the y -axis.

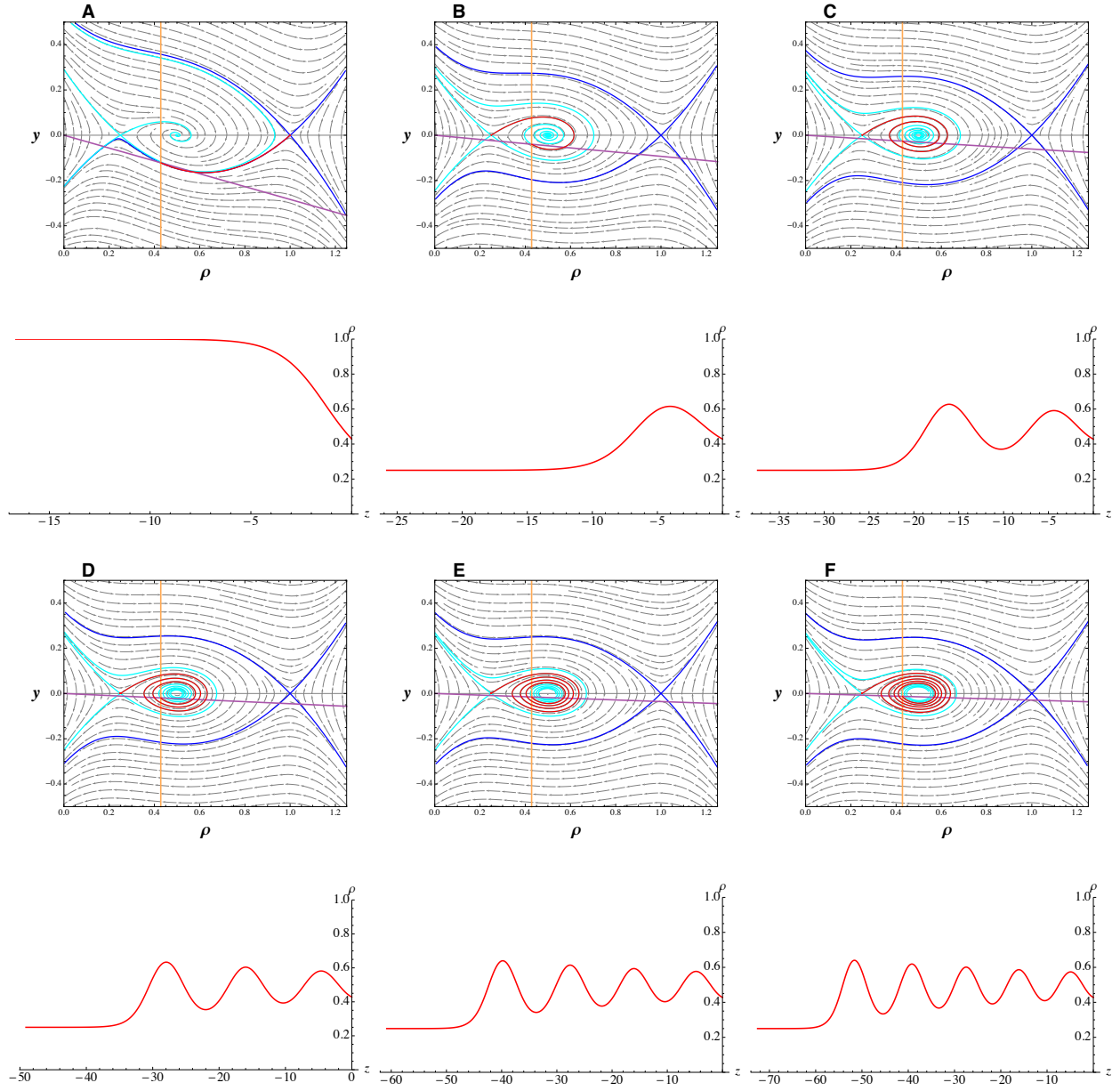


Figure 4.8: Growth function $q(\rho) = (\rho_0 - \rho)(\rho_0 - 2\rho)(\rho_0 - 4\rho)$ with logarithmic elasticity function (2.3a). Here, $k = 2.947$, $b = 1$, $F = 2.5$, $\rho_0 = 1$, (A) $\bar{\rho} = 1$, and (B)–(F) $\bar{\rho} = \frac{1}{4}$. Here, speed (A) $c = 0.8364$, (B) $c = 0.274921$, (C) $c = 0.180012$, (D) $c = 0.133061$, (E) $c = 0.104923$, and (F) $c = 0.0862904$. First row: The phase portrait of the system with the unstable and stable manifolds of the right saddle point in blue and the left saddle point in cyan, the line $\{\rho = \rho_F\}$ in orange, the curve $\left\{y = \frac{-cb}{p'(\rho)}\right\}$ in purple, and the solution trajectory in red. Second row: Respectively, the traveling wave profile of the solution trajectory in traveling wave coordinate z .

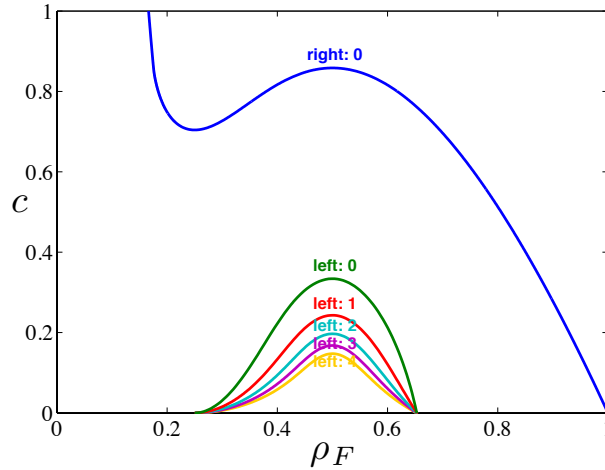


Figure 4.9: The bifurcation diagram for the function $q(\rho) = (\rho_0 - \rho)(\rho_0 - 2\rho)(\rho_0 - 4\rho)$, with logarithmic elasticity function (2.3a). Here, for the curve labeled “right,” $\bar{\rho} = 1$, and for the curves labeled “left,” $\bar{\rho} = \frac{1}{4}$. Values of ρ_F and c that lie along the curves result in solutions of the boundary value problem. The number of loops that the solution trajectory traverses about the stable spiral is labeled. Note that only a portion of the countably infinite number of curves is shown.

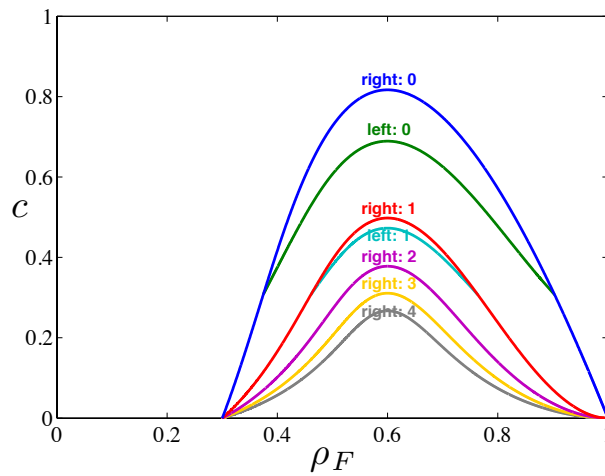


Figure 4.10: The bifurcation diagram for the function $q(\rho) = (\rho_0 - \rho)(\rho_0 - 8\rho)(3\rho_0 - 5\rho)$, with logarithmic elasticity function (2.3a). Here, for the curves labeled “right,” $\bar{\rho} = 1$, and for the curves labeled “left,” $\bar{\rho} = \frac{1}{8}$. Values of ρ_F and c that lie along the curves result in solutions of the boundary value problem. The number of loops that the solution trajectory traverses about the stable spiral is labeled. Note that only a portion of the countably infinite number of curves is shown.

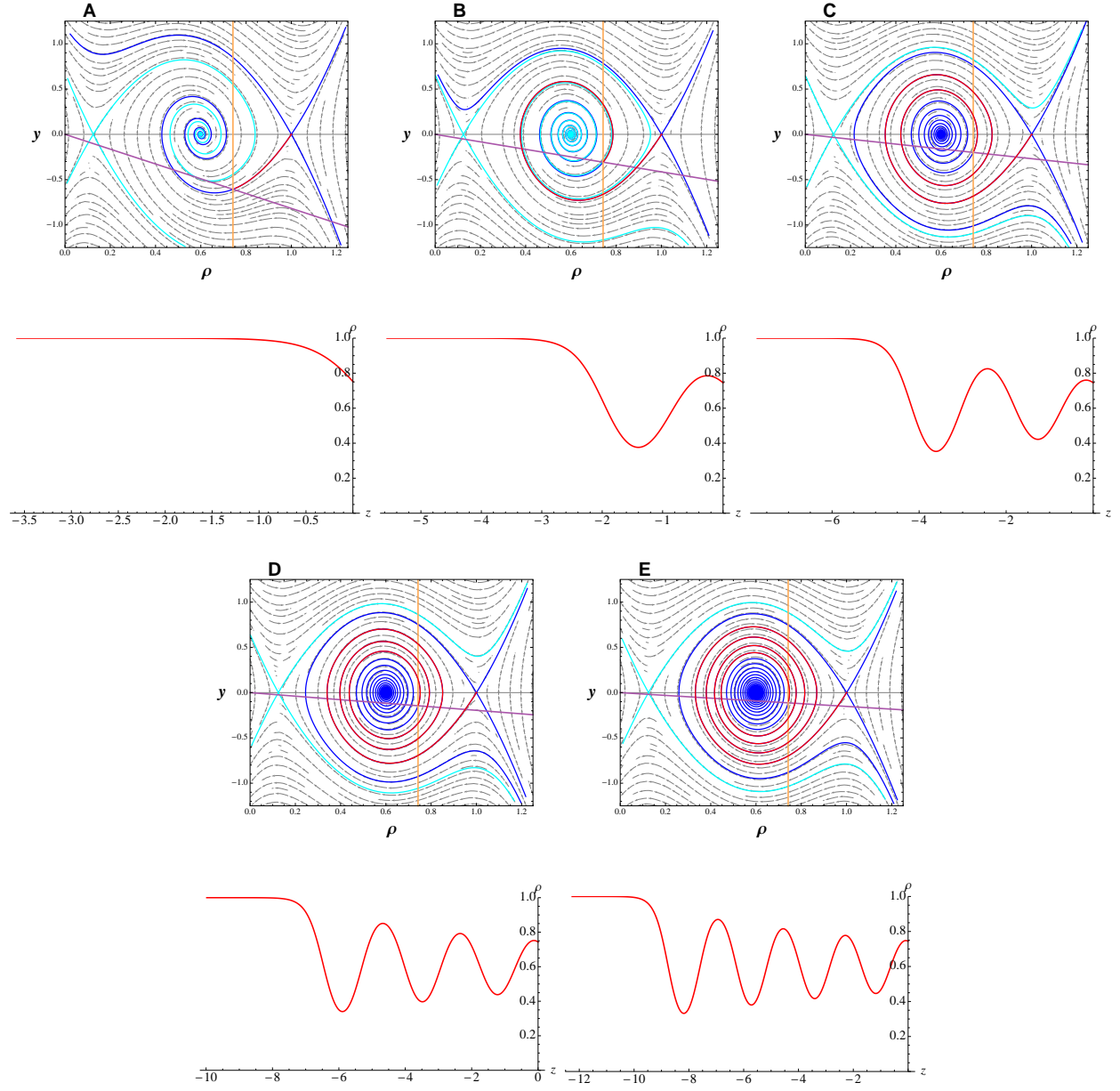


Figure 4.11: Growth function $q(\rho) = (\rho_0 - \rho)(\rho_0 - 8\rho)(3\rho_0 - 5\rho)$ with logarithmic elasticity function (2.3a). Here, $k = 0.838$, $b = 1$, $F = 0.25$, $\rho_0 = 1$, $\bar{\rho} = 1$, and speed (A) $c = 0.685214$, (B) $c = 0.347028$, (C) $c = 0.225201$, (D) $c = 0.163641$, and (E) $c = 0.127442$. First row: The phase portrait of the system with the unstable and stable manifolds of the right saddle point in blue and the left saddle point in cyan, the line $\{\rho = \rho_F\}$ in orange, the curve $\left\{y = \frac{-cb}{p'(\rho)}\right\}$ in purple, and the solution trajectory in red. Second row: Respectively, the traveling wave profile of the solution trajectory in traveling wave coordinate z .

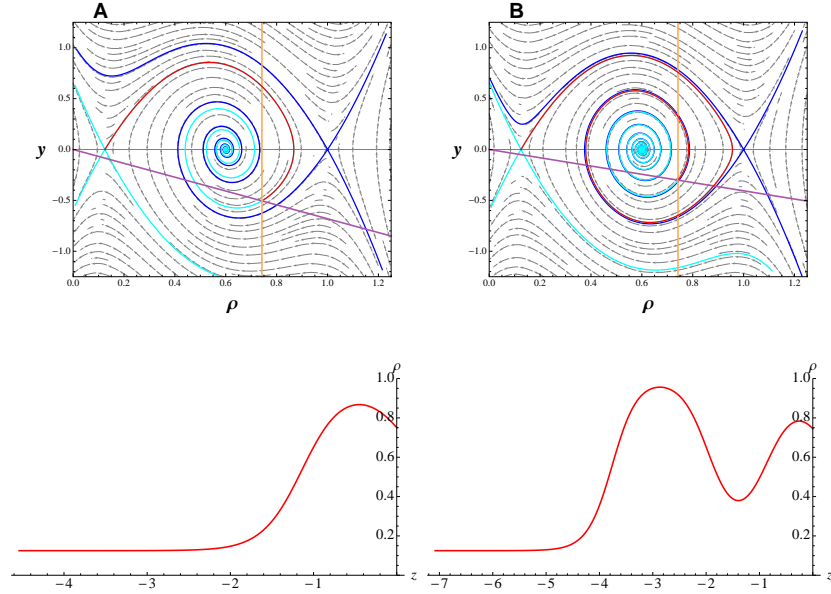


Figure 4.12: Growth function $q(\rho) = (\rho_0 - \rho)(\rho_0 - 8\rho)(3\rho_0 - 5\rho)$ with logarithmic elasticity function (2.3a). Here, $k = 0.838$, $b = 1$, $F = 0.25$, $\rho_0 = 1$, $\bar{\rho} = \frac{1}{8}$, and speed (A) $c = 0.570056$, and (B) $c = 0.340016$. First row: The phase portrait of the system with the unstable and stable manifolds of the right saddle point in blue and the left saddle point in cyan, the line $\{\rho = \rho_F\}$ in orange, the curve $\left\{y = \frac{-cb}{p'(\rho)}\right\}$ in purple, and the solution trajectory in red. Second row: Respectively, the traveling wave profile of the solution trajectory in traveling wave coordinate z .

Our analysis of the number of possible solutions of the boundary value problem (4.17)–(4.18) directly extends to the case when the growth function q has four or more simple roots. These functions will result in phase portraits with alternating saddles and stable spirals/nodes and the number of possible solutions for a chosen ρ_F are either none, one, a finite number, or a countably infinite number. This analysis also extends to the case when the growth function q has three or more roots with some repeated, with the exception of $\bar{\rho}$ which must be a simple root. These growth functions give similar results as simple root functions of one lower degree.

In a limiting sense, Theorems 4.1 and 4.2 extend to more arbitrary growth functions, even if the growth functions do not have any roots (noting that our proofs do not directly

Table 4.1: *Speed of the leading edge. The numerical speed is $v(20)$, the simulated velocity of the leading edge in the material formulation at $t = 20$. The analytic speed is the speed c of the traveling wave solution in the spatial formulation.*

Growth Function	linear (2.9a)	Fisher (2.9b)	cubic (2.9c)
Numerical Speed	0.275432	1.13160	0.267114
Analytic Speed	0.274120	1.12652	0.266062

apply to those cases). Recalling the Weierstrass Approximation Theorem, any continuous function (on a bounded domain) can be approximated by a polynomial and hence could satisfy the conditions of Theorems 4.1 or 4.2. Thus, a Gaussian function centered at $\rho = \rho_0$ (equivalently at $\epsilon = 0$) and a piecewise linear function approximating a Gaussian function (resembling the growth rate function in Stolarska et al. [68]) have traveling wave solutions that exist in a limiting sense, such that the leading edge of cells moves at a constant, or slowly increasing, rate.

4.2.3 Stability of Traveling Waves

Especially in the cases of the previous section where there are multiple traveling wave solutions, it is useful to analyze their stability as solutions of the original partial differential equation. Numerically, we will examine whether the traveling wave persists if it used as the initial condition. If it does persist, it is called stable, but if deviations from the exact traveling wave, whether introduced deliberately or due to numerical error, are amplified, it is called unstable. It is likely that stable traveling waves are the only traveling waves that could be observed biologically.

In Table 4.1, we list the speed of the leading edge found numerically, which is $v(20)$, the simulated velocity of the leading edge in the material formulation at $t = 20$, and analytically, which is the speed c of the traveling wave solution in the spatial formulation, for the linear (2.9a), Fisher (2.9b), and cubic (2.9c) growth functions. The percent error between the two

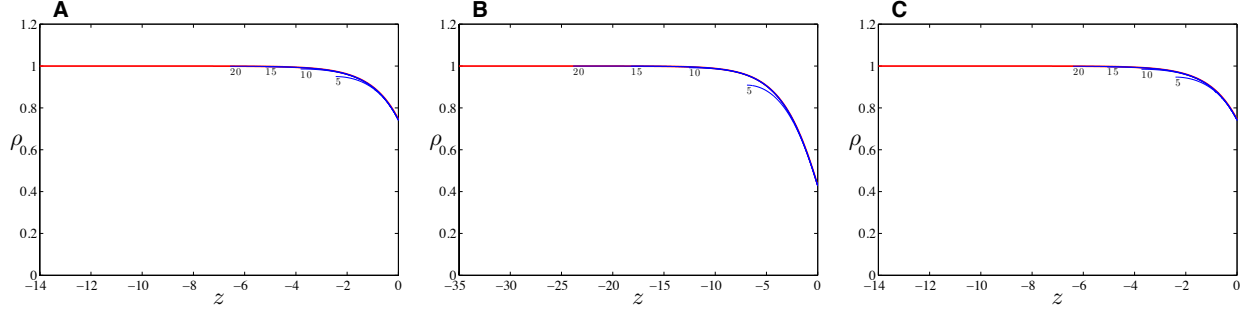


Figure 4.13: *Stability of traveling waves – material formulation to spatial formulation:* The density profiles at $t = 5, 10, 15, 20$ hours (in blue) found numerically in the material formulation converge to the analytic traveling wave solution (in red) found in the spatial formulation. Here, we have the logarithmic elasticity function (2.3a) and (A) linear growth function (2.9a), $k = 0.838$, $b = 1$, $F = 0.25$, $\rho_0 = 1$, $c = 0.274120$, (B) Fisher growth function (2.9b), $k = 2.947$, $b = 1$, $F = 2.5$, $\rho_0 = 1$, $c = 1.12652$, and (C) cubic growth function (2.9c), $k = 0.838$, $b = 1$, $F = 0.25$, $\rho_0 = 1$, $c = 0.266062$.

speeds is less than 1% for all three growth functions.

4.2.3.1 Material Formulation to Spatial Formulation First, we will examine whether the density profiles of the numerical solutions of the material formulation converge to the analytic traveling wave density profile of the spatial formulation. At any specified time, we can calculate the density of the cell layer from the cell positions x found from a numerical simulation of the material formulation via equation (2.21), which can also be written as

$$\tilde{\rho}(s, t) = \rho_0 \left(\frac{\partial x(s, t)}{\partial s} \right)^{-1} \frac{\partial \hat{s}(s, t)}{\partial s}. \quad (4.26)$$

We discretize $\frac{\partial x}{\partial s}$ and $\frac{\partial \hat{s}}{\partial s}$ using centered difference in the interior and forward (backward) difference on the left (right) boundary. See Figure 4.13 for an illustration of the numerical density profiles of the material formulation. These numerical density profiles converge to the analytic traveling wave density profile of the spatial formulation for the linear (2.9a), Fisher (2.9b), and cubic (2.9c) growth functions with logarithmic elasticity function (2.3a).

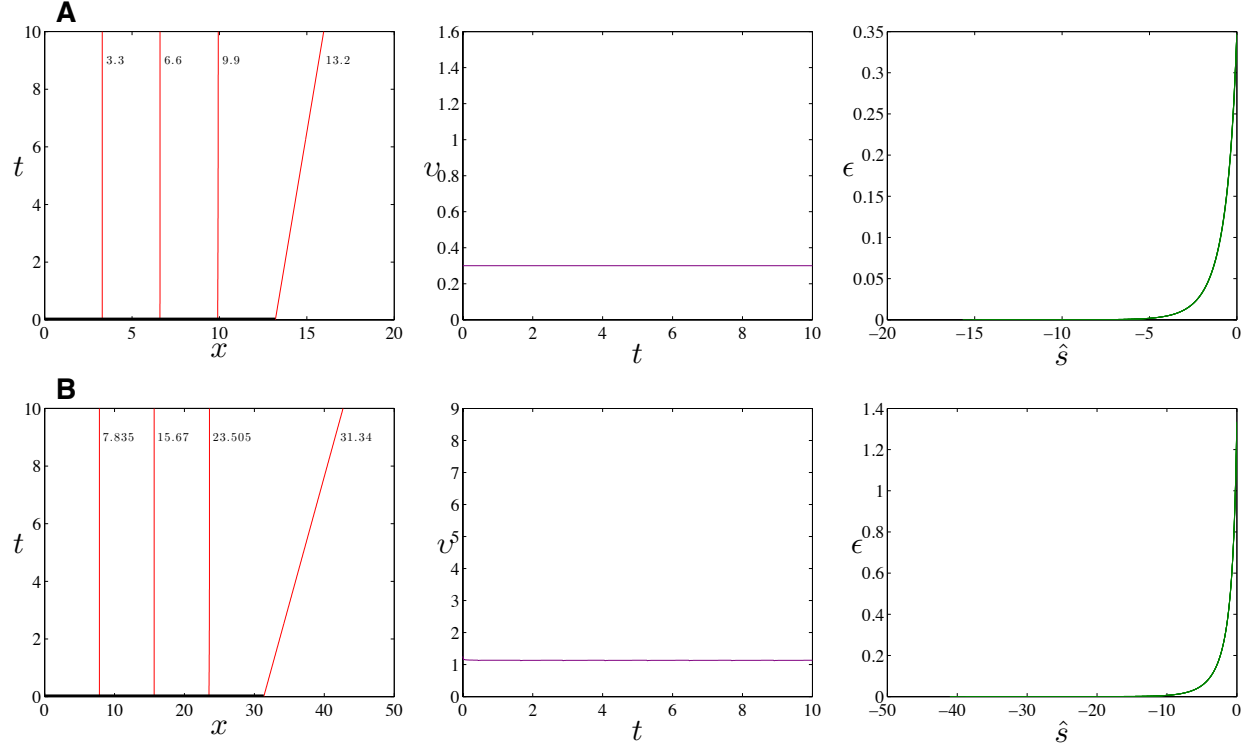


Figure 4.14: *Stability of traveling waves – spatial formulation to material formulation:* The initial cell positions are found using the analytic traveling wave solution shown in Figure 4.13. Here, we have the logarithmic elasticity function (2.3a) and (A) linear growth function (2.9a), $k = 0.838$, $b = 1$, $F = 0.25$, $\rho_0 = 1$, and (B) Fisher growth function (2.9b), $k = 2.947$, $b = 1$, $F = 2.5$, $\rho_0 = 1$.

4.2.3.2 Spatial Formulation to Material Formulation Next, we will use the analytic traveling wave solution of the spatial formulation as an initial condition for the material formulation numerical simulations. From the analytic traveling wave density profile, we calculate $s = s(x, t)$ via equation (2.21) assuming $\frac{\partial \hat{s}}{\partial s} = 1$, since \hat{s} is simply a relabeling of cell positions. Thus, we numerically solve the ordinary differential equation $s' = \rho$ with initial condition $s(0) = 0$. Then we must invert this solution to find $x = x(s, t)$. Using these cell positions x and s as an initial state, we calculate the numerical solution to the material formulation.

Figure 4.14 shows the results for the linear (2.9a) and Fisher (2.9b) growth functions with logarithmic elasticity function (2.3a). The velocity of the leading edge approximates

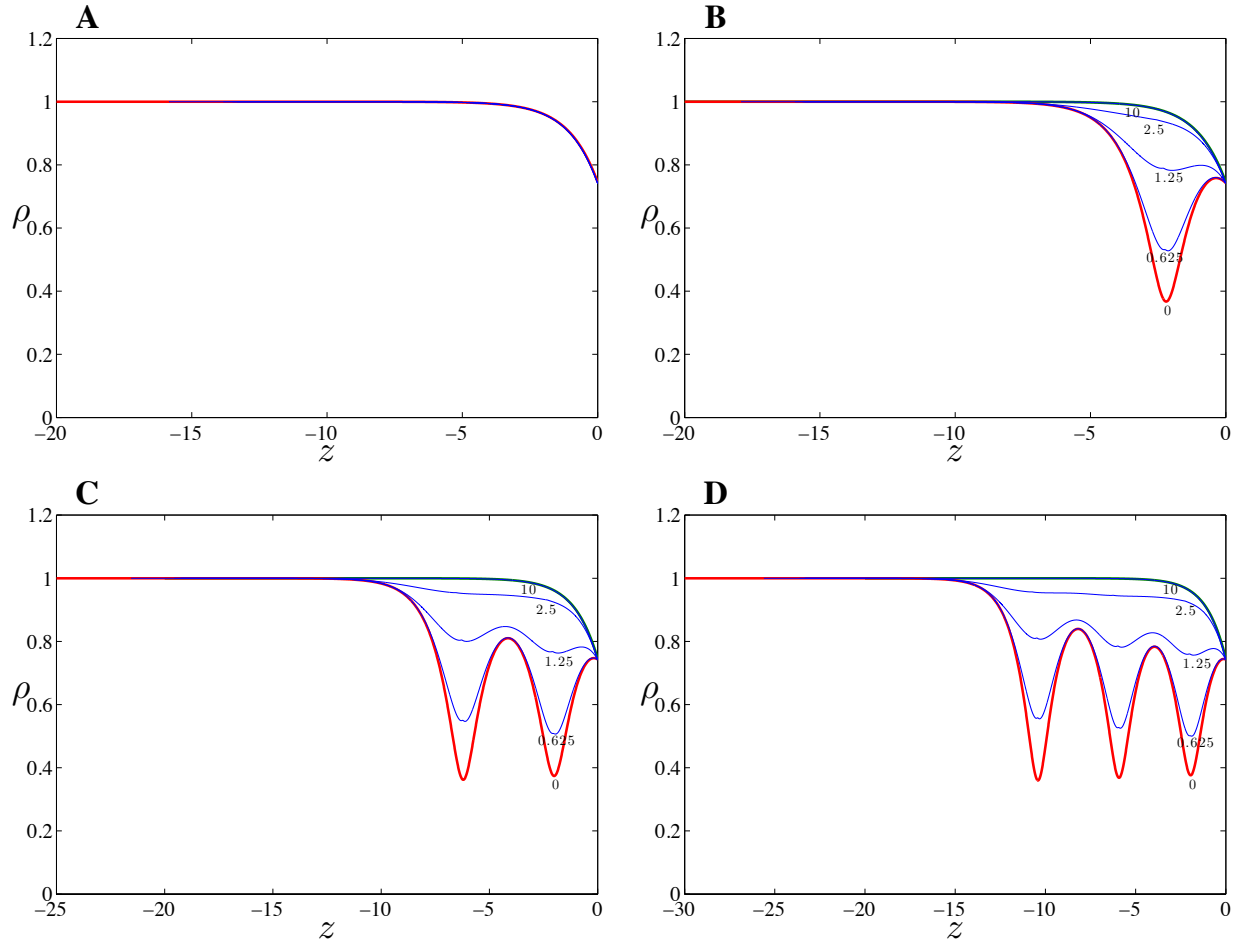


Figure 4.15: *Stability of traveling waves – spatial formulation to material formulation: Cubic growth function (2.9c) with logarithmic elasticity function (2.3a), $k = 0.838$, $b = 1$, $F = 0.25$, and $\rho_0 = 1$. The initial cell positions (red) are found using the analytic traveling wave solution shown in (A) Figure 4.6A, (B) Figure 4.6B, (C) Figure 4.6C, and (D) Figure 4.6D. The density profiles at $t = 0.625, 1.25, 2.5, 10$ hours (blue) found numerically in the material formulation converge to the analytic traveling wave solution (green) shown in Figure 4.6A.*

the speeds listed in Table 4.1, and the shape of the plot of ϵ versus \hat{s} remains unchanged throughout time, implying that the traveling wave solution persists. The density profiles from the numerical simulations remain the exact analytic traveling wave density profile throughout the integration.

Figure 4.15 shows the results for the cubic growth function (2.9c), Figure 4.16 shows the

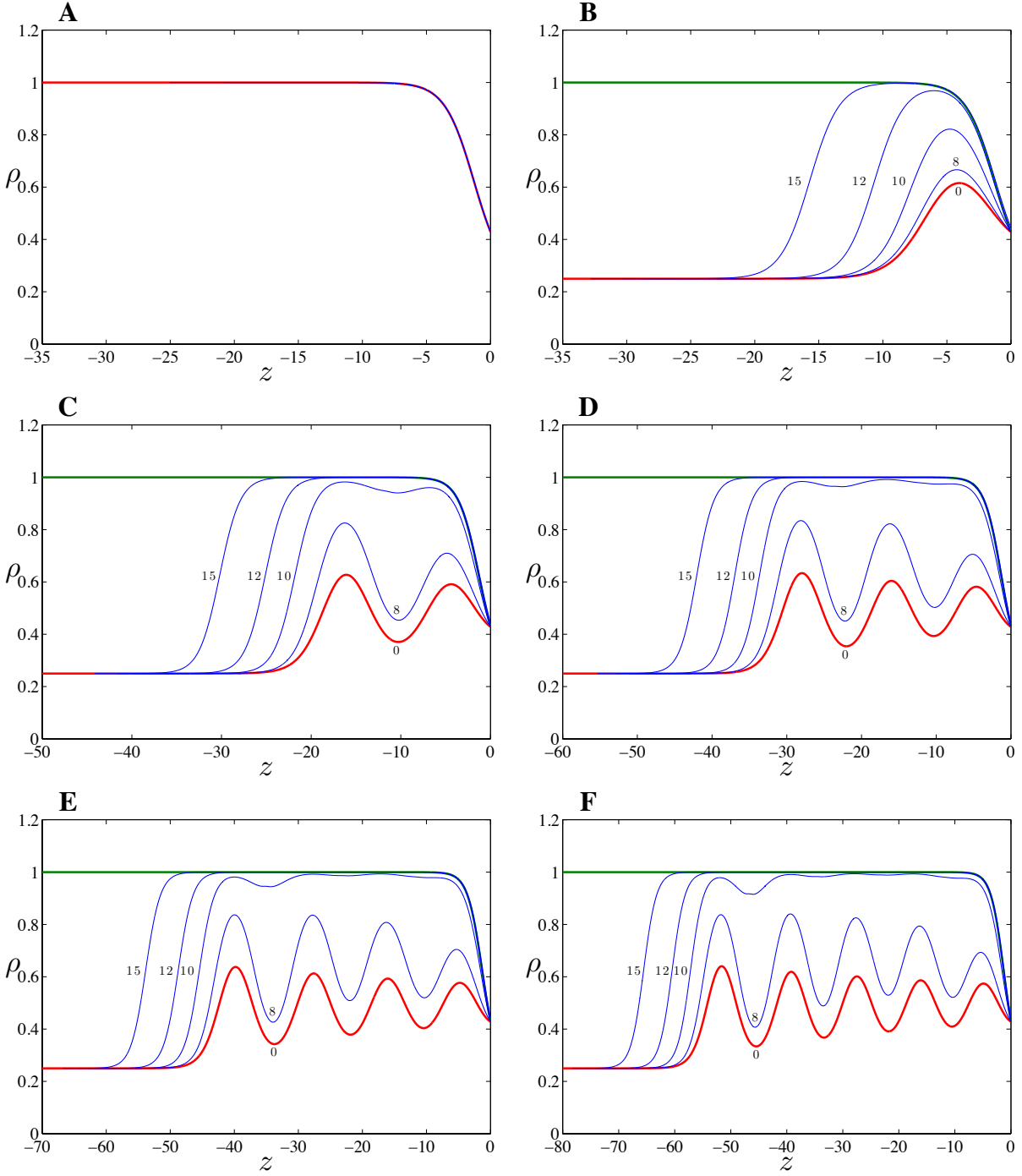


Figure 4.16: *Stability of traveling waves – spatial formulation to material formulation: Growth function $q(\rho) = (\rho_0 - \rho)(\rho_0 - 2\rho)(\rho_0 - 4\rho)$ with logarithmic elasticity function (2.3a), $k = 2.947$, $b = 1$, $F = 2.5$, and $\rho_0 = 1$. The initial cell positions (red) are found using the analytic traveling wave solution shown in (A) Figure 4.8A, (B) Figure 4.8B, (C) Figure 4.8C, (D) Figure 4.8D, (E) Figure 4.8E, and (F) Figure 4.8F. The density profiles at $t = 8, 10, 12, 15$ hours (blue) found numerically in the material formulation converge to the analytic traveling wave solution (green) shown in Figure 4.8A.*

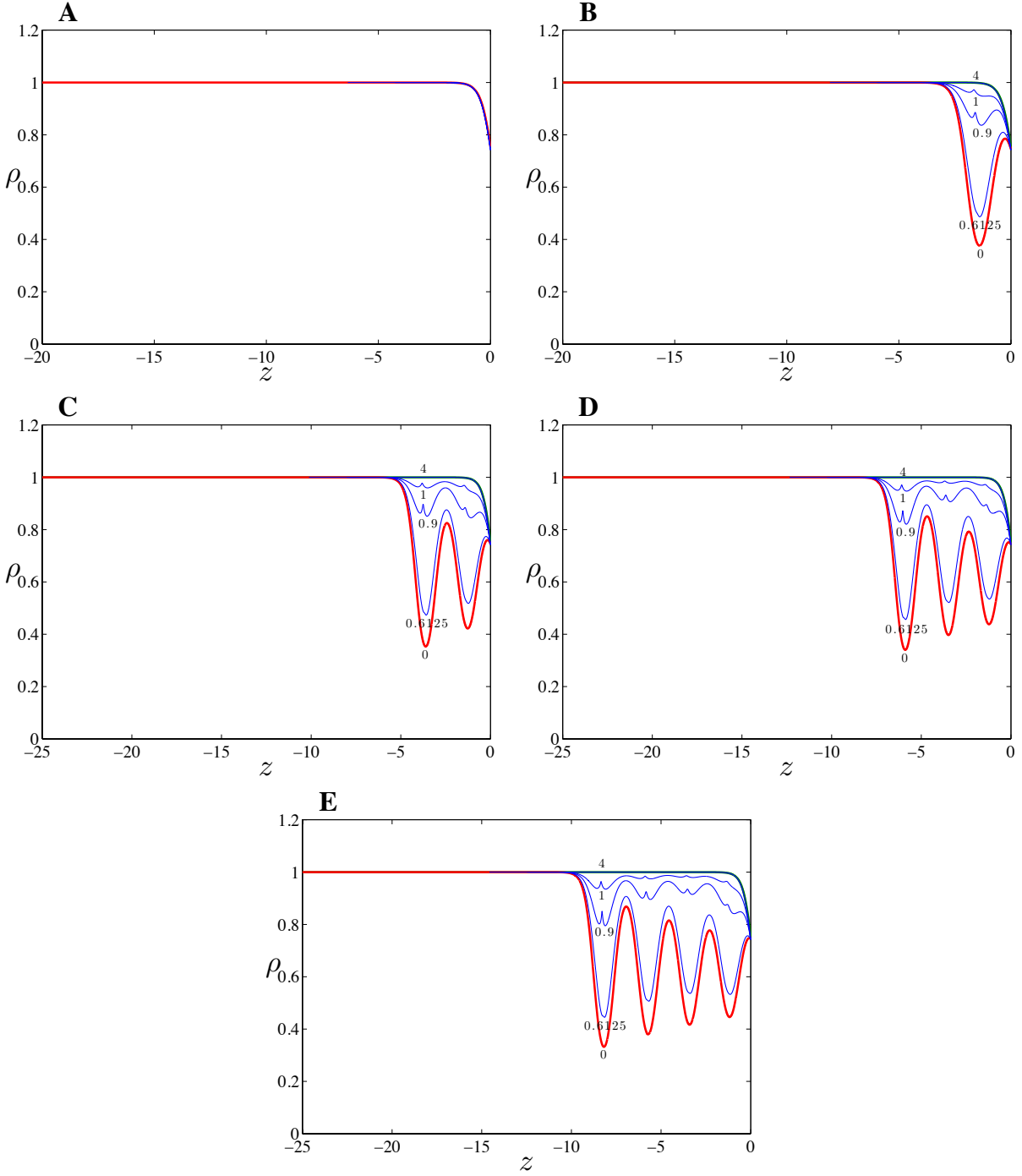


Figure 4.17: *Stability of traveling waves – spatial formulation to material formulation: Growth function $q(\rho) = (\rho_0 - \rho)(\rho_0 - 8\rho)(3\rho_0 - 5\rho)$ with logarithmic elasticity function (2.3a), $k = 2.947$, $b = 1$, $F = 2.5$, $\rho_0 = 1$, and $\bar{\rho} = 1$. The initial cell positions (red) are found using the analytic traveling wave solution shown in (A) Figure 4.11A, (B) Figure 4.11B, (C) Figure 4.11C, (D) Figure 4.11D, and (E) Figure 4.11E. The density profiles at $t = 0.6125, 0.9, 1, 4$ hours (blue) found numerically in the material formulation converge to the analytic traveling wave solution (green) shown in Figure 4.11A.*

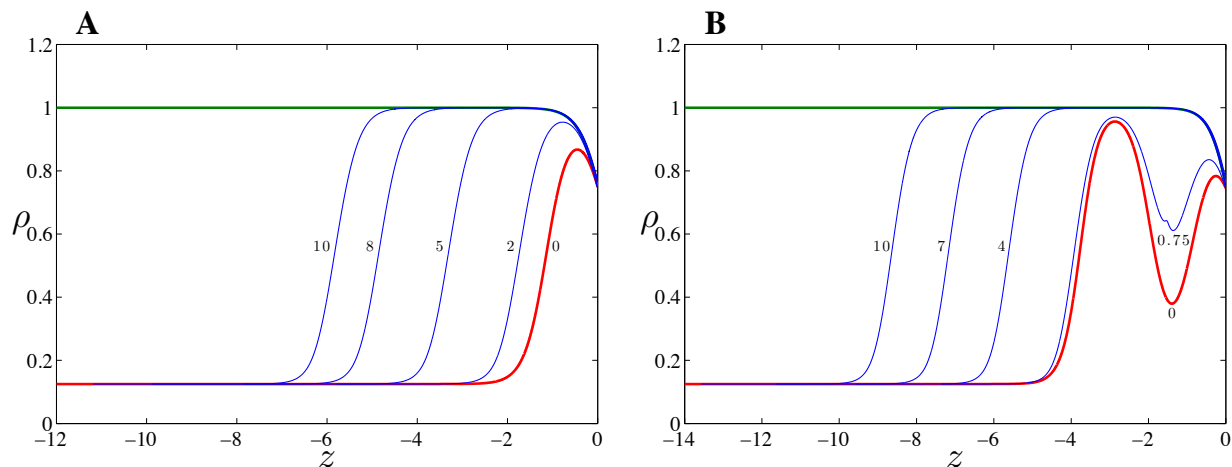


Figure 4.18: *Stability of traveling waves – spatial formulation to material formulation: Growth function $q(\rho) = (\rho_0 - \rho)(\rho_0 - 8\rho)(3\rho_0 - 5\rho)$ with logarithmic elasticity function (2.3a), $k = 2.947$, $b = 1$, $F = 2.5$, $\rho_0 = 1$, and $\bar{\rho} = \frac{1}{8}$. The initial cell positions (red) are found using the analytic traveling wave solution shown in (A) Figure 4.12A, and (B) Figure 4.12B. The density profiles at (A) $t = 2, 5, 8, 10$ hours, (B) $t = 0.75, 4, 7, 10$ hours (blue) found numerically in the material formulation converge to the analytic traveling wave solution (green) shown in Figure 4.11A.*

results for the growth function $q(\rho) = (\rho_0 - \rho)(\rho_0 - 2\rho)(\rho_0 - 4\rho)$, and Figures 4.17–4.18 show the results for the growth function $q(\rho) = (\rho_0 - \rho)(\rho_0 - 8\rho)(3\rho_0 - 5\rho)$, all with logarithmic elasticity function (2.3a). We observe different behaviors based on how many loops the solution trajectory in phase space traverses about the stable spiral (see Figures 4.6, 4.8, and 4.11–4.12, respectively). If the solution trajectory traverses no loops about the stable spiral, we observe the same behavior as for the linear and Fisher growth functions; the traveling wave solution persists. If the solution trajectory traverses one or more loops about the stable spiral, we observe that the traveling wave solution does not persist but instead converges to the traveling wave solution for the trajectory that traverses no loops.

In the cases where there are two saddles, such as in Figures 4.16–4.18, all of the solutions converge to the traveling wave solution for the trajectory that never crosses the ρ -axis. For the traveling wave solutions for the saddle on the left (Figures 4.16B–F and 4.18), we see that there is a “wave within a wave” such that once the solutions converge near the moving

boundary ($z = 0$) to the trajectory that never crosses the ρ -axis, there is a traveling wave of density that moves to the left.

We conclude our study with the following proposition.

Proposition 4.3. *The traveling wave solutions of the spatial formulation of one-dimensional single layer cell migration are stable if the solution trajectory in phase space does not cross the horizontal ρ -axis.*

5.0 2-D DUAL LAYER CELL MIGRATION MODEL

Thus far, we have discussed continuum mechanical models of one-dimensional single cell layer migration. These models are applicable to epithelial cell sheet migration where the cell layer thickness is approximately uniform throughout. However, migrating cells in vivo are often in much more complex environments, and capturing this complexity in experiments and models will lead to better understanding of the true processes.

In this chapter, we extend the two-dimensional spatial formulation of Arciero et al. [3], which we have presented in previous chapters in one dimension, to incorporate two adhering cell layers. The intent is to study the phenomenon of one migrating cell layer acting as the substrate of another migrating cell layer. We will apply this model to time-lapse images of migrating epithelial and mesenchymal cells during gastrulation in Chapter 7.

5.1 DERIVATION OF MODEL EQUATIONS

We start by deriving the equations for an arbitrary number of cell layers that are situated precisely on top of one another (like a layer cake), where we denote the bottom layer as layer 1 and the top layer as layer N . Each cell layer is represented as a compressible fluid, like in the single layer model derived in Section 2.2. The variable $\rho_n(x, y, t)$ describes the cell density of layer n as a function of the spatial position $\mathbf{x} = (x, y)$ and time t . Conservation of cell number (mass) for each layer implies

$$\frac{\partial \rho_n}{\partial t} = -\nabla \cdot (\rho_n \mathbf{v}_n) + q(\rho_n), \quad n = 1, \dots, N, \quad (5.1)$$

where $\mathbf{v}_n = ((v_n)_x, (v_n)_y)$ is the velocity of cell layer n , and q is the cell proliferation/apoptosis term as in Section 2.2. In modeling gastrulation, proliferation is not an important factor, so we set $q = 0$ for all layers.

Conservation of linear momentum implies

$$\rho_n \frac{\partial \mathbf{v}_n}{\partial t} + \rho_n (\mathbf{v}_n \cdot \nabla) \mathbf{v}_n = \mathbf{B}_n + \nabla \cdot \mathbf{T}_n, \quad n = 1, \dots, N, \quad (5.2)$$

where \mathbf{B}_n accounts for the force of adhesion to adjacent layers, i.e. the negative of traction force, and \mathbf{T}_n represents stresses within cell layer n . Assuming that acceleration is negligible since the cells do not move very fast, (5.2) becomes

$$0 = \mathbf{B}_n + \nabla \cdot \mathbf{T}_n, \quad n = 1, \dots, N. \quad (5.3)$$

We assume that all layers behave as compressible inviscid fluids with the constitutive equation

$$\mathbf{T}_n = -p(\rho_n) \mathbf{I}, \quad n = 1, \dots, N, \quad (5.4)$$

where p is the pressure within the cell layer as in Section 2.2. Assuming the force of adhesion is negatively proportional to the relative velocity of the cell layer, then

$$\text{bottom layer:} \quad \mathbf{B}_1 = -b_1 \mathbf{v}_1 + b_2 (\mathbf{v}_2 - \mathbf{v}_1), \quad (5.5a)$$

$$\text{middle layers:} \quad \mathbf{B}_n = -b_n (\mathbf{v}_n - \mathbf{v}_{n-1}) + b_{n+1} (\mathbf{v}_{n+1} - \mathbf{v}_n), \quad (5.5b)$$

$$\text{top layer:} \quad \mathbf{B}_N = -b_N (\mathbf{v}_N - \mathbf{v}_{N-1}), \quad (5.5c)$$

where the adhesion constant b_n describes the adhesion between the $(n-1)^{\text{st}}$ and n^{th} layers. The adhesion constant b_1 describes the adhesion between the substrate and the bottom layer.

Substituting (5.4) and (5.5) into the conservation of linear momentum equation (5.3), simplifying to the case of only two layers, and solving for the velocities, we obtain

$$\mathbf{v}_1 = -\frac{1}{b_1} p'(\rho_1) \nabla \rho_1 - \frac{1}{b_1} p'(\rho_2) \nabla \rho_2, \quad (5.6a)$$

$$\mathbf{v}_2 = -\frac{1}{b_1} p'(\rho_1) \nabla \rho_1 - \left(\frac{1}{b_1} + \frac{1}{b_2} \right) p'(\rho_2) \nabla \rho_2. \quad (5.6b)$$

Then substituting these velocities into the conservation of mass equation (5.1), we obtain the following governing equations that describe the evolution of cell density,

$$\frac{\partial \rho_1}{\partial t} = \frac{1}{b_1} \nabla \cdot (p'(\rho_1) \nabla \rho_1) + \frac{1}{b_1} \nabla \cdot (p'(\rho_2) \nabla \rho_2), \quad (5.7a)$$

$$\frac{\partial \rho_2}{\partial t} = \frac{1}{b_1} \nabla \cdot (p'(\rho_1) \nabla \rho_1) + \left(\frac{1}{b_1} + \frac{1}{b_2} \right) \nabla \cdot (p'(\rho_2) \nabla \rho_2). \quad (5.7b)$$

We assume the constitutive equation for the pressure is

$$p(\rho_n) = k_n \ln \left(\frac{\rho_n}{\rho_{0n}} \right), \quad n = 1, 2, \quad (5.8)$$

where k_n is the residual stretching modulus of cell layer n after cytoskeleton relaxation and ρ_{0n} is the constant density of the relaxed (unstressed) cell layer n . Other choices are possible, such as Hooke's law and the ideal gas law as studied in previous chapters. We choose the logarithmic relation for the dual layer model because it allows for an infinite magnitude of stress for both $\rho \rightarrow 0$ and $\rho \rightarrow \infty$, giving an appropriate behavior at both large and small densities. The governing equation (5.7) becomes

$$\frac{\partial \rho_1}{\partial t} = \frac{k_1}{b_1} \Delta \rho_1 + \frac{k_2}{b_1} \Delta \rho_2, \quad (5.9a)$$

$$\frac{\partial \rho_2}{\partial t} = \frac{k_1}{b_1} \Delta \rho_1 + \left(\frac{k_2}{b_1} + \frac{k_2}{b_2} \right) \Delta \rho_2. \quad (5.9b)$$

We remove the assumption that the cell layers are situated precisely on top of one another, and instead assume that the bottom layer extends further than the top layer. Also, we assume that the top layer can never extend further than the bottom layer. In light of these assumptions, a schematic of the problem is illustrated in Figure 5.1. Therefore, our governing equations are

$$\frac{\partial \rho_1}{\partial t} = \frac{k_1}{b_1} \Delta \rho_1, \quad \text{in } \Omega_1^t \setminus \Omega_2^t, \quad (5.10a)$$

$$\frac{\partial \rho_1}{\partial t} = \frac{k_1}{b_1} \Delta \rho_1 + \frac{k_2}{b_1} \Delta \rho_2, \quad \text{in } \Omega_1^t \cap \Omega_2^t, \quad (5.10b)$$

$$\frac{\partial \rho_2}{\partial t} = \frac{k_1}{b_1} \Delta \rho_1 + \left(\frac{k_2}{b_1} + \frac{k_2}{b_2} \right) \Delta \rho_2, \quad \text{in } \Omega_1^t \cap \Omega_2^t, \quad (5.10c)$$

where we see that there is a single uncoupled equation in the domain $\Omega_1^t \setminus \Omega_2^t$ and a system of coupled equations in the domain $\Omega_1^t \cap \Omega_2^t$.

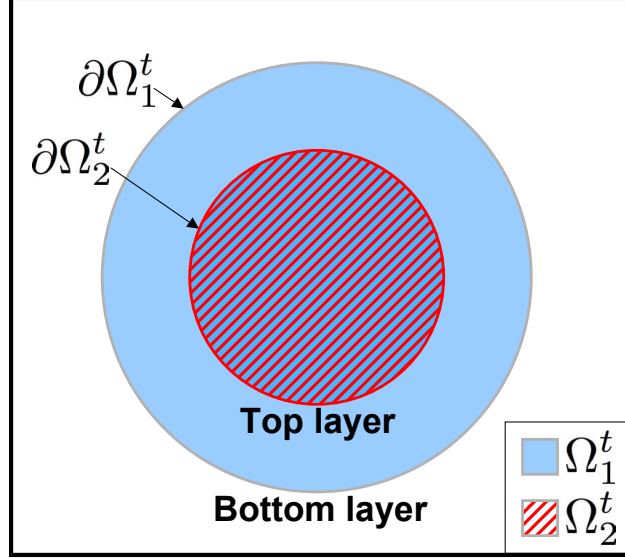


Figure 5.1: Schematic representation of the 2-D dual layer problem as if looking at the cell layers from above. The blue area Ω_1^t represents the bottom cell layer and the red hatched area Ω_2^t represents the top cell layer. The single uncoupled equation (5.10a) is valid in the domain $\Omega_1^t \setminus \Omega_2^t$ and the system of coupled equations (5.10b)-(5.10c) is valid in the domain $\Omega_1^t \cap \Omega_2^t$. The boundaries of the two cell layers are labeled $\partial\Omega_1^t$ (bottom layer) and $\partial\Omega_2^t$ (top layer).

At the boundaries, we assume for layer n that the lamellipodia exert a constant force per unit length F_n that is equal in magnitude to that of cells in the interior, i.e. $p(\rho_n) = -F_n$, and thus we have Dirichlet boundary conditions

$$\rho_1 = \rho_{01} e^{-F_1/k_1}, \quad \text{on } \partial\Omega_1^t, \quad (5.11a)$$

$$\rho_2 = \rho_{02} e^{-F_2/k_2}, \quad \text{on } \partial\Omega_2^t. \quad (5.11b)$$

We also have a condition on the velocity of the boundary which comes from (5.6),

$$\mathbf{v}_1 = -\frac{k_1}{b_1} \frac{1}{\rho_{01}} e^{F_1/k_1} \nabla \rho_1, \quad \text{on } \partial\Omega_1^t, \quad (5.12a)$$

$$\mathbf{v}_2 = -\frac{k_1}{b_1} \frac{1}{\rho_1} \nabla \rho_1 - \left(\frac{k_2}{b_1} + \frac{k_2}{b_2} \right) \frac{1}{\rho_{02}} e^{F_2/k_2} \nabla \rho_2, \quad \text{on } \partial\Omega_2^t, \quad (5.12b)$$

that reduces to the Stefan condition

$$\mathbf{v}_1 \cdot \mathbf{n}_1 = \left(-\frac{k_1}{b_1} \frac{1}{\rho_{01}} e^{F_1/k_1} \nabla \rho_1 \right) \cdot \mathbf{n}_1, \quad \text{on } \partial\Omega_1^t, \quad (5.13a)$$

$$\mathbf{v}_2 \cdot \mathbf{n}_2 = \left(-\frac{k_1}{b_1} \frac{1}{\rho_1} \nabla \rho_1 - \left(\frac{k_2}{b_1} + \frac{k_2}{b_2} \right) \frac{1}{\rho_{02}} e^{F_2/k_2} \nabla \rho_2 \right) \cdot \mathbf{n}_2, \quad \text{on } \partial\Omega_2^t, \quad (5.13b)$$

where \mathbf{n}_n is the outward normal to $\partial\Omega_n^t$.

An interface condition on $\partial\Omega_2^t$ comes from a balance of forces. On the boundary $\partial\Omega_2^t$,

$$T_1|_{\Omega_1^t \cap \Omega_2^t} + T_2 = T_1|_{\Omega_1^t \setminus \Omega_2^t} \implies -p\left(\rho_1|_{\Omega_1^t \cap \Omega_2^t}\right) + F_2 = -p\left(\rho_1|_{\Omega_1^t \setminus \Omega_2^t}\right), \quad (5.14)$$

and thus with the constitutive equation (5.8), the interface condition is

$$\rho_1|_{\Omega_1^t \cap \Omega_2^t} = e^{F_2/k_1} \rho_1|_{\Omega_1^t \setminus \Omega_2^t}, \quad \text{on } \partial\Omega_2^t. \quad (5.15)$$

Initially, we assume that the density of each cell layer is equal to the density of a stretched layer, i.e. $p(\rho_n) = F_n$, and the bottom layer is uniformly dense, and thus we obtain

$$\rho_1 = \rho_{01} e^{F_1/k_1}, \quad \text{in } \Omega_1^0, \quad (5.16a)$$

$$\rho_2 = \rho_{02} e^{F_2/k_2}, \quad \text{in } \Omega_2^0. \quad (5.16b)$$

The two-dimensional dual layer free boundary problem is characterized by the governing equations (5.10), boundary conditions (5.11), Stefan conditions (5.13), interface condition (5.15), and initial conditions (5.16). In summary, these equations, conditions, variables, and parameters are as follows.

Model 3. 2-D Dual Layer Cell Migration

Governing Equations

$$\frac{\partial \rho_1}{\partial t} = \frac{k_1}{b_1} \Delta \rho_1, \quad \text{in } \Omega_1^t \setminus \Omega_2^t$$

$$\frac{\partial \rho_1}{\partial t} = \frac{k_1}{b_1} \Delta \rho_1 + \frac{k_2}{b_1} \Delta \rho_2, \quad \text{in } \Omega_1^t \cap \Omega_2^t$$

$$\frac{\partial \rho_2}{\partial t} = \frac{k_1}{b_1} \Delta \rho_1 + \left(\frac{k_2}{b_1} + \frac{k_2}{b_2} \right) \Delta \rho_2, \quad \text{in } \Omega_1^t \cap \Omega_2^t$$

Initial Conditions

$$\rho_1 = \rho_{01} e^{F_1/k_1}, \quad \text{in } \Omega_1^0$$

$$\rho_2 = \rho_{02} e^{F_2/k_2}, \quad \text{in } \Omega_2^0$$

Boundary Conditions

$$\rho_1 = \rho_{01} e^{-F_1/k_1}, \quad \text{on } \partial\Omega_1^t$$

$$\rho_2 = \rho_{02} e^{-F_2/k_2}, \quad \text{on } \partial\Omega_2^t$$

Stefan Conditions

$$\mathbf{v}_1 \cdot \mathbf{n}_1 = \left(-\frac{k_1}{b_1} \frac{1}{\rho_{01}} e^{F_1/k_1} \nabla \rho_1 \right) \cdot \mathbf{n}_1, \quad \text{on } \partial\Omega_1^t$$

$$\mathbf{v}_2 \cdot \mathbf{n}_2 = \left(-\frac{k_1}{b_1} \frac{1}{\rho_1} \nabla \rho_1 - \left(\frac{k_2}{b_1} + \frac{k_2}{b_2} \right) \frac{1}{\rho_{02}} e^{F_2/k_2} \nabla \rho_2 \right) \cdot \mathbf{n}_2, \quad \text{on } \partial\Omega_2^t$$

Interface Condition

$$\rho_1 \Big|_{\Omega_1^t \cap \Omega_2^t} = e^{F_2/k_1} \rho_1 \Big|_{\Omega_1^t \setminus \Omega_2^t}, \quad \text{on } \partial\Omega_2^t$$

Variables

- t = time
- $\mathbf{x} = (x, y)$ = spatial position of cells
- \mathbf{v}_1 = velocity of the bottom layer
- \mathbf{v}_2 = velocity of the top layer
- \mathbf{n}_1 = outward unit normal to $\partial\Omega_1^t$
- \mathbf{n}_2 = outward unit normal to $\partial\Omega_2^t$
- $\rho_1(x, y, t)$ = cell density of the bottom layer
- $\rho_2(\mathbf{x}, t)$ = cell density of the top layer

Parameters

- b_1 = adhesion constant between the bottom cell layer and the substrate
- b_2 = adhesion constant between the bottom and top cell layers

- F_1 = net external force that develops as a result of lamellipodia formation in the bottom layer
- F_2 = net external force that develops as a result of lamellipodia formation in the top layer
- k_1 = residual stretching modulus of the bottom layer after cytoskeleton relaxation
- k_2 = residual stretching modulus of the top layer after cytoskeleton relaxation
- ρ_{01} = constant density of the initial relaxed (unstressed) bottom cell layer
- ρ_{02} = constant density of the initial relaxed (unstressed) top cell layer

6.0 NUMERICAL SOLUTIONS OF 2-D DUAL LAYER MODEL

A numerical solution of the spatial formulation of the two-dimensional dual layer cell migration model (Model 3) presented in the previous chapter for given initial cell layer geometries and parameters k_1 , k_2 , b_1 , b_2 , F_1 , F_2 , ρ_{01} , and ρ_{02} can be found using a level set method, as described in Section 6.1. Parameter values used in this chapter were chosen based on estimates from Arciero et al. [3].

For all of our simulations, we observe a jump in density in the bottom layer on $\partial\Omega_2^t$, the boundary of the top layer. Since the lamellipodia of the cells in the top layer physically pull back the cells directly below, the density of the bottom layer just inside of $\partial\Omega_2^t$ is larger, compared to the density of the bottom layer a bit further to the inside of $\partial\Omega_2^t$. Due to a balance of forces, the density of cells directly in front of the cells that were physically pulled back will decrease. Thus, the density of the bottom layer just outside of $\partial\Omega_2^t$ is smaller, compared to the density of the bottom layer a bit further to the outside of $\partial\Omega_2^t$. As the top layer reaches equilibrium and slows its movement, the jump in density in the bottom layer on $\partial\Omega_2^t$ persists, but just inside of $\partial\Omega_2^t$, the slope of the density does not significantly change. The behavior is similar for just outside of $\partial\Omega_2^t$.

Figures 6.1–6.3 show the evolution of two cell layers in the case where each layer has the same mechanical properties, i.e. the same parameters, and the initial areas are the same for different initial geometries, which include circles, ellipses, an annulus and circle, two separated circles, two small circles inside a large circle, rectangles, a diamond and square, astroids, and roses.

The average instantaneous normal velocity of the cells at the edge decreases over time (see Figure 6.4) for all the different initial geometry cases, and if the simulations were allowed to run long enough, an equilibrium state would be reached in which the cells move no further.

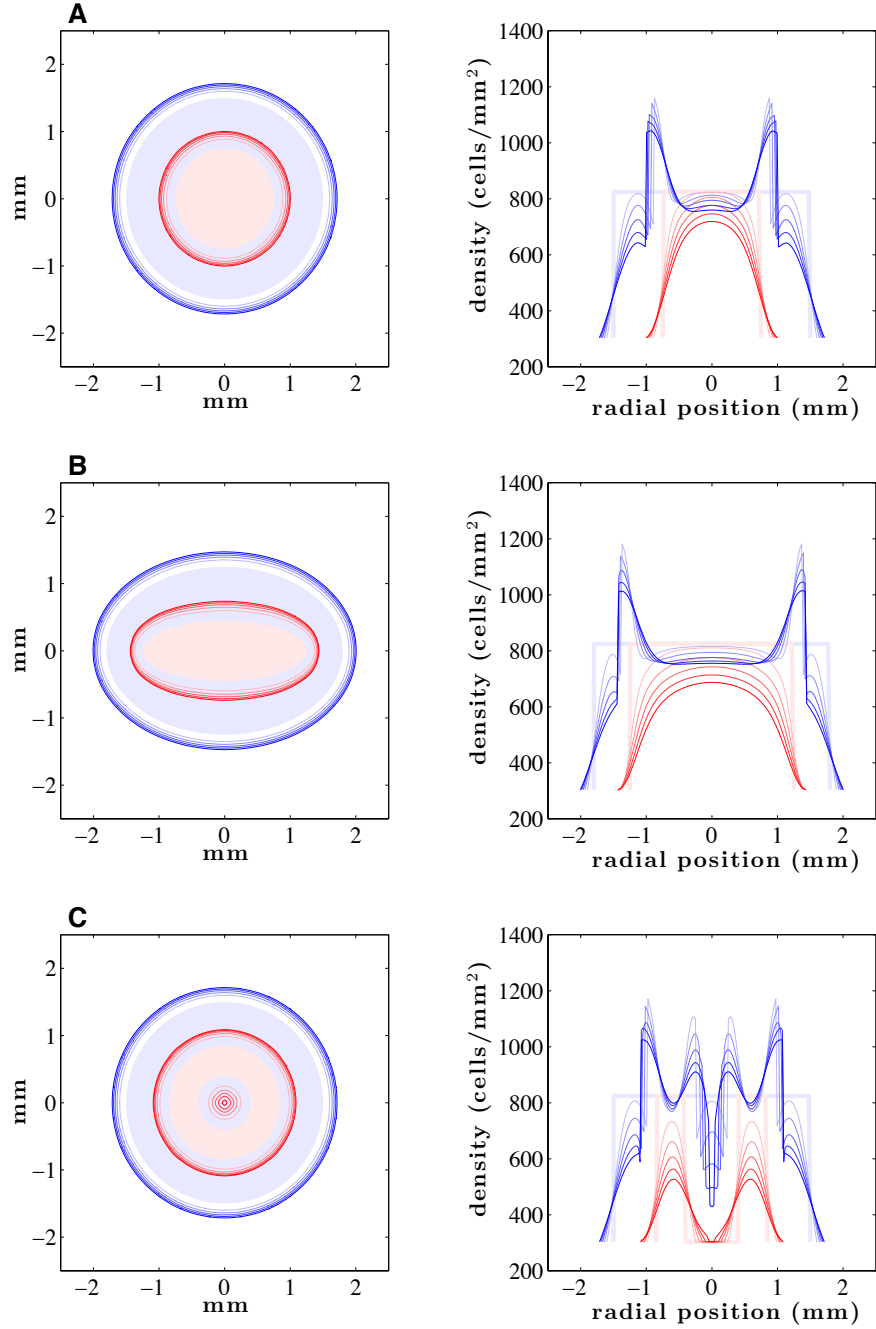


Figure 6.1: Numerical solution of the dual layer model for (A) circles, (B) ellipses, and (C) an annulus and a circle. Here, $\frac{F_1}{k_1} = \frac{F_2}{k_2} = \frac{F_2}{k_1} = 0.5$ (dimensionless), $\frac{k_1}{b_1} = \frac{k_2}{b_2} = \frac{k_2}{b_1} = 5000 \frac{\mu\text{m}^2}{h}$, and $\rho_{01} = \rho_{02} = 0.0005 \frac{\text{cells}}{\mu\text{m}^2}$. The top layer is in red and the bottom layer is in blue. The shaded regions indicate where the cells are initially seeded, and the initial area of the bottom layer is $2.25 \times 10^6 \pi \mu\text{m}^2$ and the initial area of the top layer is $5.625 \times 10^5 \pi \mu\text{m}^2$. The curves are drawn at every 2 hours from 2 to 10 hours, where the lightest curve is at $t = 2$ and the darkest curve is at $t = 10$. The first column shows the position of the leading edge of the migrating cell layers as seen from above, and the second column shows the density profile of the cell layers as a cross-section through the x -axis.

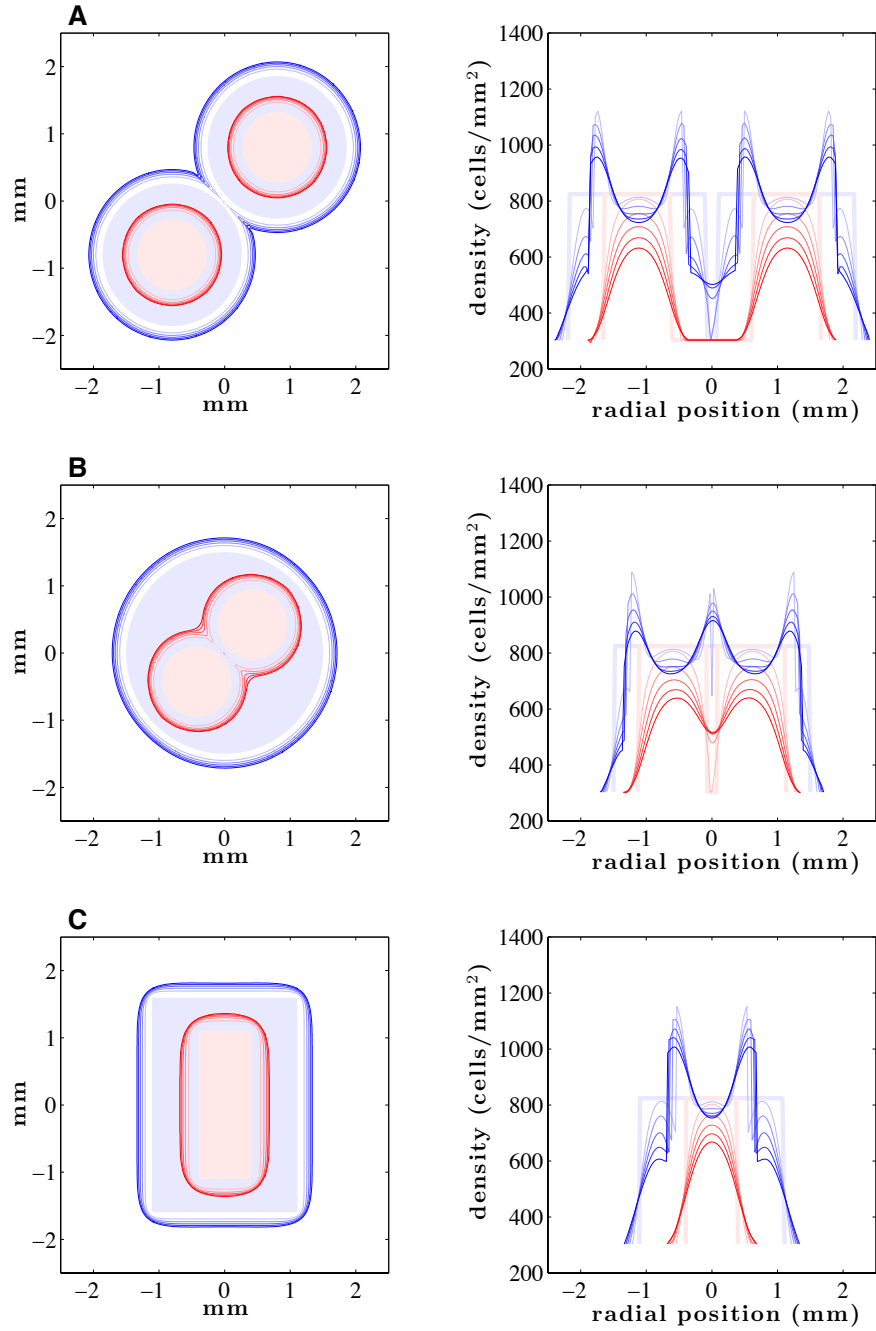


Figure 6.2: Numerical solution of the dual layer model for (A) two separated circles, (B) two small circles inside a large circle, and (C) rectangles. Parameters, initial areas, and color scheme are the same as in Figure 6.1. The first column shows the position of the leading edge of the migrating cell layers as seen from above, and the second column shows the density profile of the cell layers as a cross-section through (A)–(B) the line $y = x$, and (C) the x -axis.

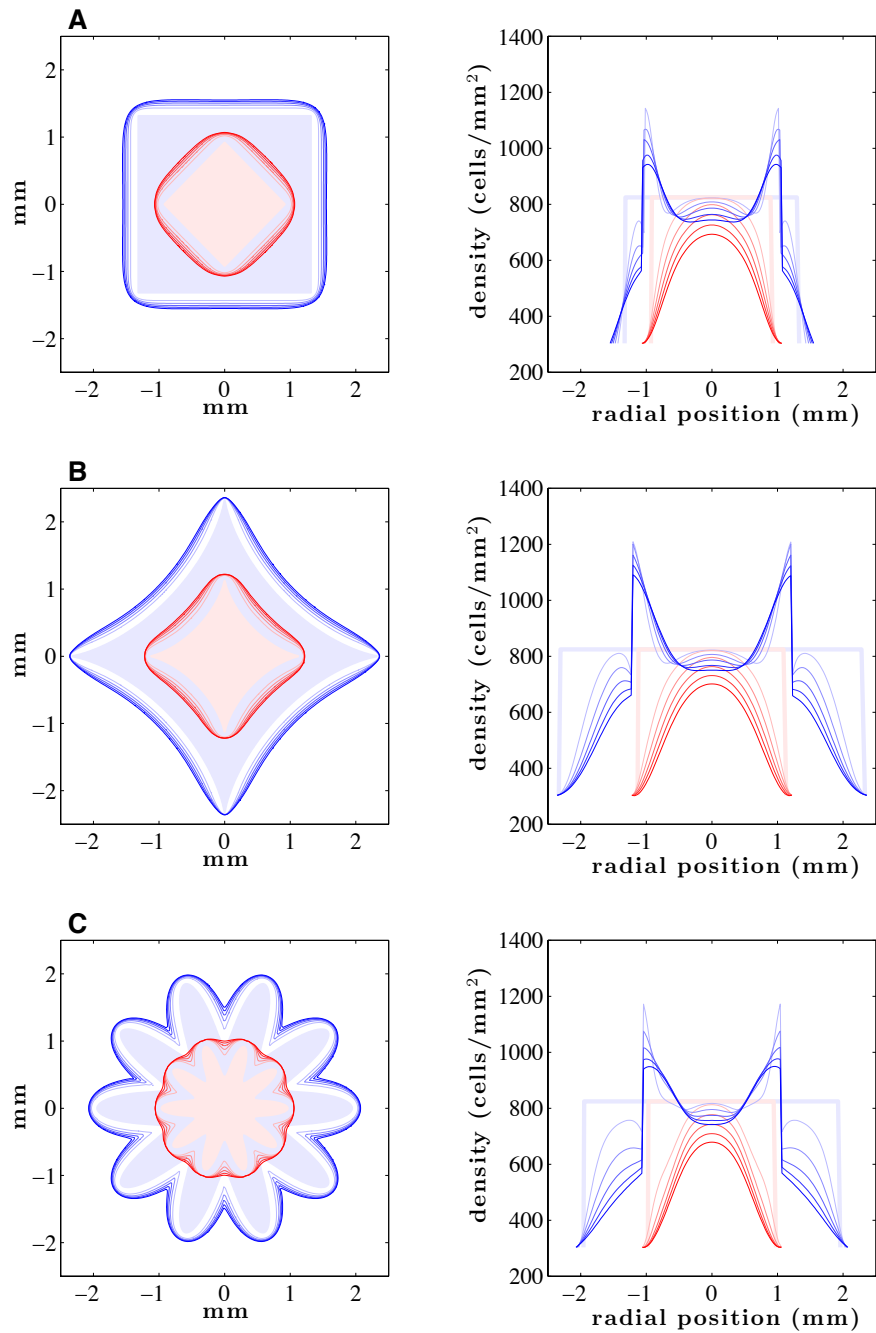


Figure 6.3: Numerical solution of the dual layer model for (A) a diamond and square, (B) astroids, and (C) roses. Parameters, initial areas, and color scheme are the same as in Figure 6.1. The first column shows the position of the leading edge of the migrating cell layers as seen from above, and the second column shows the density profile of the cell layers as a cross-section through the x -axis.

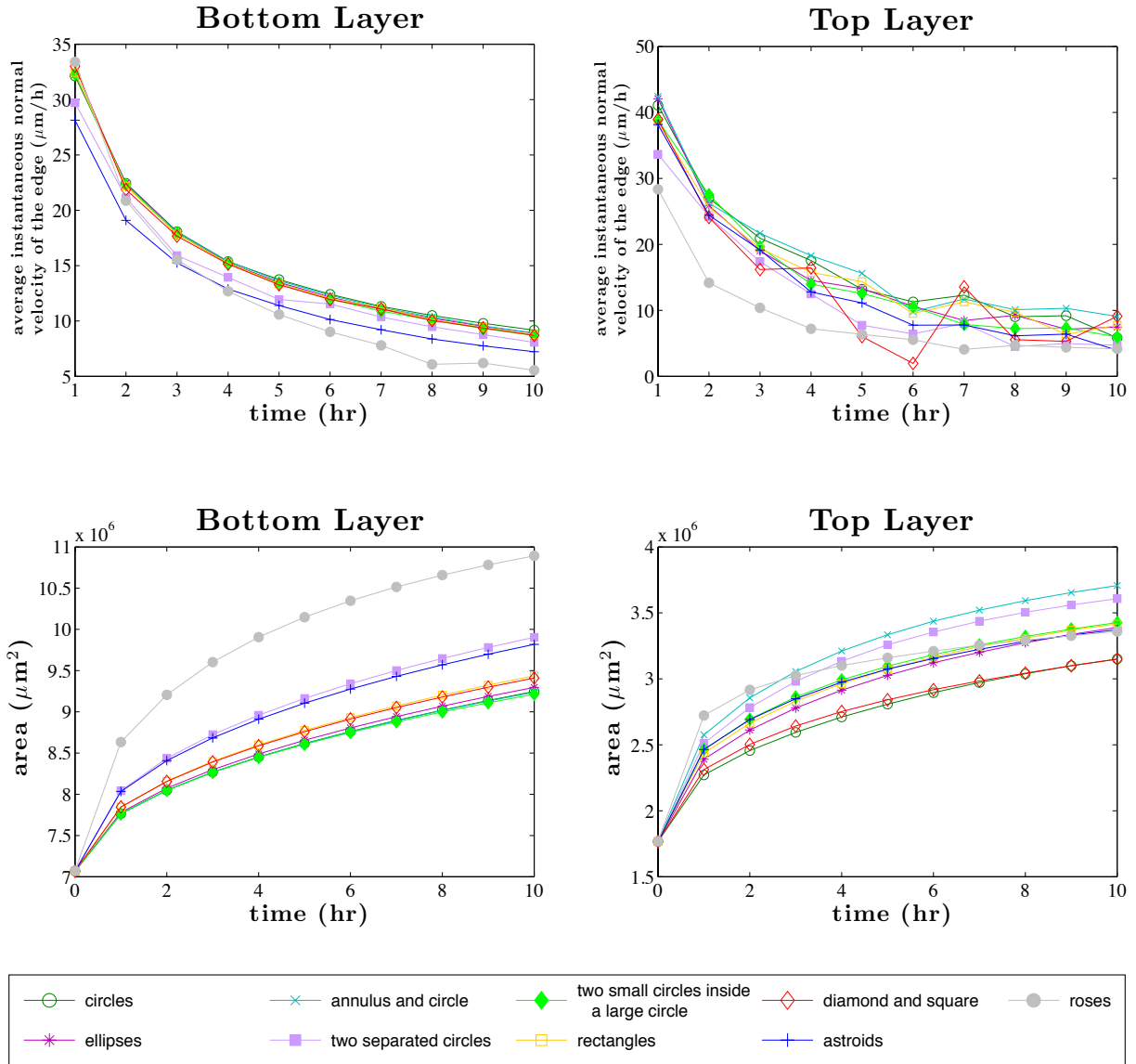


Figure 6.4: Average instantaneous normal velocity of the edge (in the first row) and area (in the second row) of the 2-D dual layer numerical solutions for the bottom and top layers where the initial geometries are circles (Figure 6.1A), ellipses (Figure 6.1B), an annulus and circle (Figure 6.1C), two separated circles (Figure 6.2A), two small circles inside a large circle (Figure 6.2B), rectangles (Figure 6.2C), a diamond and square (Figure 6.3A), astroids (Figure 6.3B), and roses (Figure 6.3C).

Table 6.1: *Relative change in area of the 2-D dual layer numerical solutions for the bottom and top layers in the simulations where the initial area for the bottom layer is $2.25 \times 10^6 \pi \mu m^2$ and for the top layer is $5.625 \times 10^5 \pi \mu m^2$. The relative change, in units of μm^2 , is compared between $t = 0$ hours and $t = 10$ hours. cf. Figures 6.1–6.4.*

Simulation	Bottom Layer	Top Layer
circles	0.3890	0.9087
ellipses	0.3082	0.7831
annulus and circle	0.3313	0.7821
two separated circles	0.3069	1.0980
two small circles inside a large circle	0.3153	0.9182
rectangles	0.3351	0.9333
diamond and square	0.5409	0.9011
astroids	0.3035	0.9392
roses	0.4010	1.0419

This is due to the absence of cell proliferation within the cell layers. If cells were allowed to proliferate in the simulations, it is likely that the cells would continue to spread.

Figure 6.4 also shows the change in area of both layers for all the different initial geometry cases and Table 6.1 lists the relative change in area between $t = 0$ hours and $t = 10$ hours. The relative change in area of the bottom layer was very similar for all the simulations. However, it appears that the less cusps and edges the initial shape has, the less relative change in area. We obtain different results for the top layer since the leading edge is affected by the behavior of the bottom layer. The initial geometries with the largest relative change in area are the two separated circles and rose, and the initial geometries with the smallest relative change in area are the ellipse and annulus. The initial geometries that evolve into a single circle or ellipse shape the soonest, the less relative change in area.

The next series of figures shows the evolution of two cell layers in the case where the

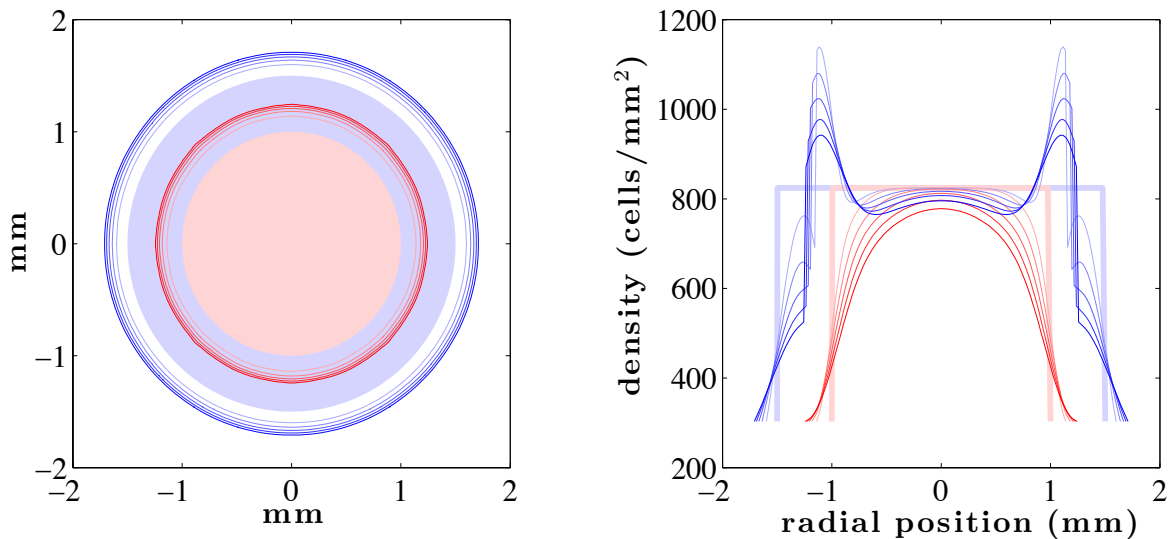


Figure 6.5: Numerical solution of the dual layer model for varying parameters (control case). Here, $\frac{F_1}{k_1} = \frac{F_2}{k_2} = \frac{F_2}{k_1} = 0.5$ (dimensionless), $\frac{k_1}{b_1} = \frac{k_2}{b_2} = \frac{k_2}{b_1} = 5000 \frac{\mu\text{m}^2}{h}$, and $\rho_{01} = \rho_{02} = 0.0005 \frac{\text{cells}}{\mu\text{m}^2}$. The top layer is in red and the bottom layer is in blue. The shaded regions indicate where the cells are initially seeded. The curves are at drawn every 2 hours from 2 to 10 hours, where the lightest curve is at $t = 2$ and the darkest curve is at $t = 10$. The first column shows the position of the leading edge of the migrating cell layers as seen from above, and the second column shows the density profile of the cell layers as a cross-section through the x -axis.

layers have differing mechanical properties, but the same initial geometry. Figure 6.5 shows the control case in which the two layers have the same parameters, i.e. $\frac{F_1}{k_1} = \frac{F_2}{k_2} = \frac{F_2}{k_1}$, $\frac{k_1}{b_1} = \frac{k_2}{b_2} = \frac{k_2}{b_1}$, and $\rho_{01} = \rho_{02}$. For each comparison simulation, we increase or decrease only one of the parameters, except ρ_{01} or ρ_{02} . Any asymmetry in the simulations shown is due to numerical error. The main differences in the simulations compared to the control case are as follows.

In Figure 6.6 we halve and double the net external force due to lamellipodia formation of the bottom layer, F_1 . Halving the force F_1 appears to cause the bottom layer to equilibrate sooner, while doubling F_1 causes the bottom layer to migrate faster and the top layer slower than in the control case.

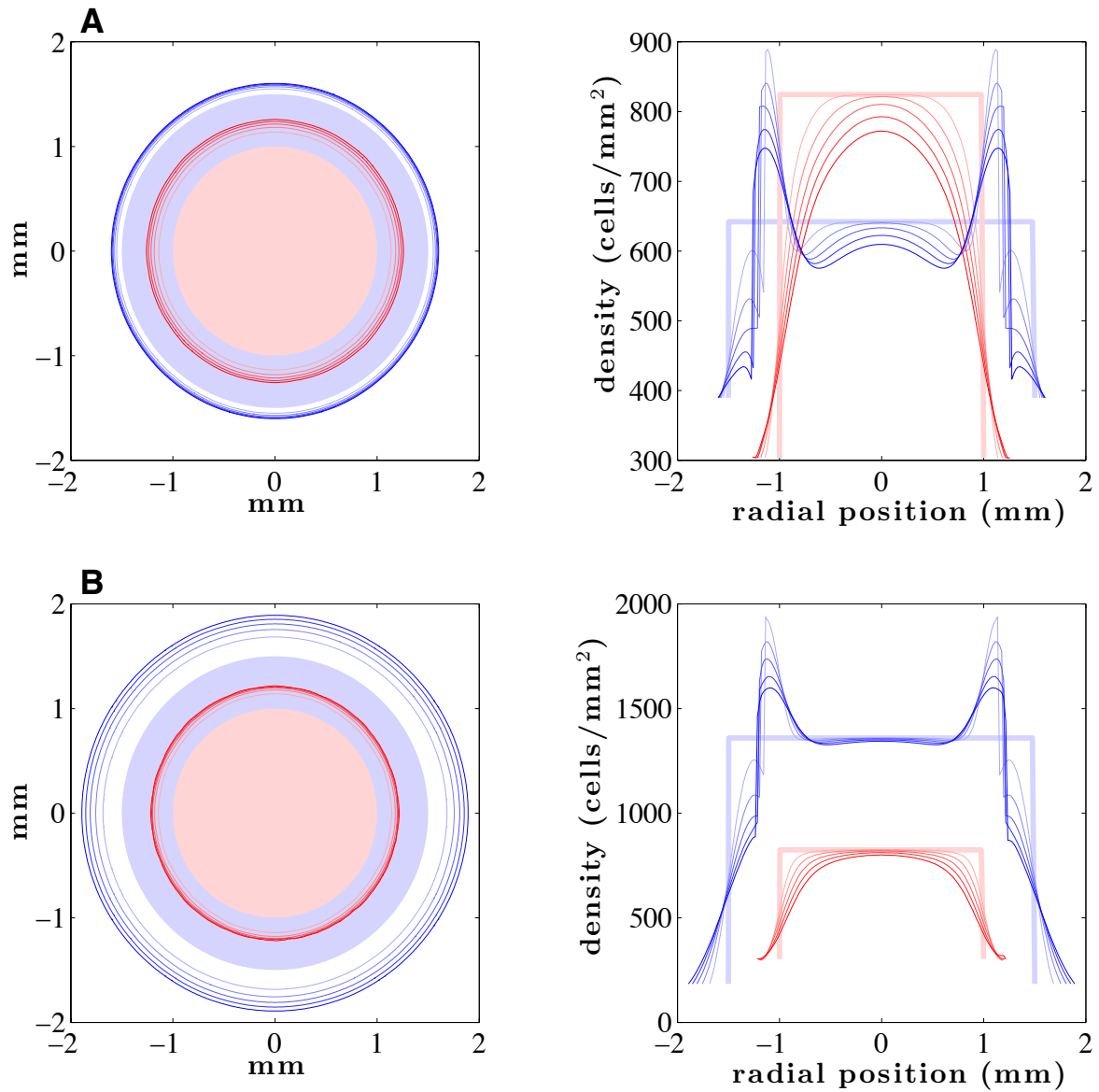


Figure 6.6: Numerical solution of the 2-D dual layer model for varying parameters. The color scheme is the same but F_1 is half or double that as in Figure 6.5 while the other parameters remain fixed, such that, respectively, (A) $\frac{F_1}{k_1} = 0.25$, and (B) $\frac{F_1}{k_1} = 1$.

In Figure 6.7 we halve and double the net external force due to lamellipodia formation of the top layer, F_2 . Halving the force F_2 appears to cause the top layer to migrate slower, while doubling F_2 causes the top layer to migrate faster and the bottom layer to have a larger density gradient near $\partial\Omega_2^t$ compared to the control case.

In Figure 6.8 we halve and double the stretching modulus of the bottom layer, k_1 . If k_1 is halved so that the bottom layer is less stiff (more flexible), the bottom layer migrates faster and has a larger density gradient near $\partial\Omega_2^t$, while if k_1 is doubled so that the bottom layer is stiffer (more rigid), the bottom layer migrates slower compared to the control case.

In Figure 6.9 we halve and double the stretching modulus of the top layer, k_2 . If k_2 is halved so that the top layer is less stiff (more flexible), the top layer appears to migrate faster, while if k_2 is doubled so that the top layer is stiffer (more rigid), the top layer migrates slower than in the control case.

In Figure 6.10 we halve and double the adhesion constant between the bottom layer and substrate, b_1 . Halving the adhesion b_1 causes the density in the interior of both layers to decrease faster, while doubling the adhesion b_1 causes the density in the interior of both layers to decrease slower compared to the control case.

In Figure 6.11 we halve and double the adhesion constant between the two layers, b_2 . Halving the adhesion b_2 causes the density in the interior of the top layer to decrease faster, while doubling the adhesion b_2 causes the density in the interior of the top layer to decrease slower compared to the control case.

We list the final area and relative difference in area compared to the control case in Table 6.2. We deduce that the parameters that have the largest influence in behavior for either the top or bottom layer are F_1 , F_2 , k_1 , and k_2 , and the parameters that have the smallest influence in behavior are b_1 and b_2 . Hence, from this study we conclude that the net external force due to lamellipodia formation and stiffness of both layers plays a substantial role in the amount of spreading of dual cell layers while the adhesion between the bottom layer and the substrate and the adhesion between the two layers does not affect migration as much.

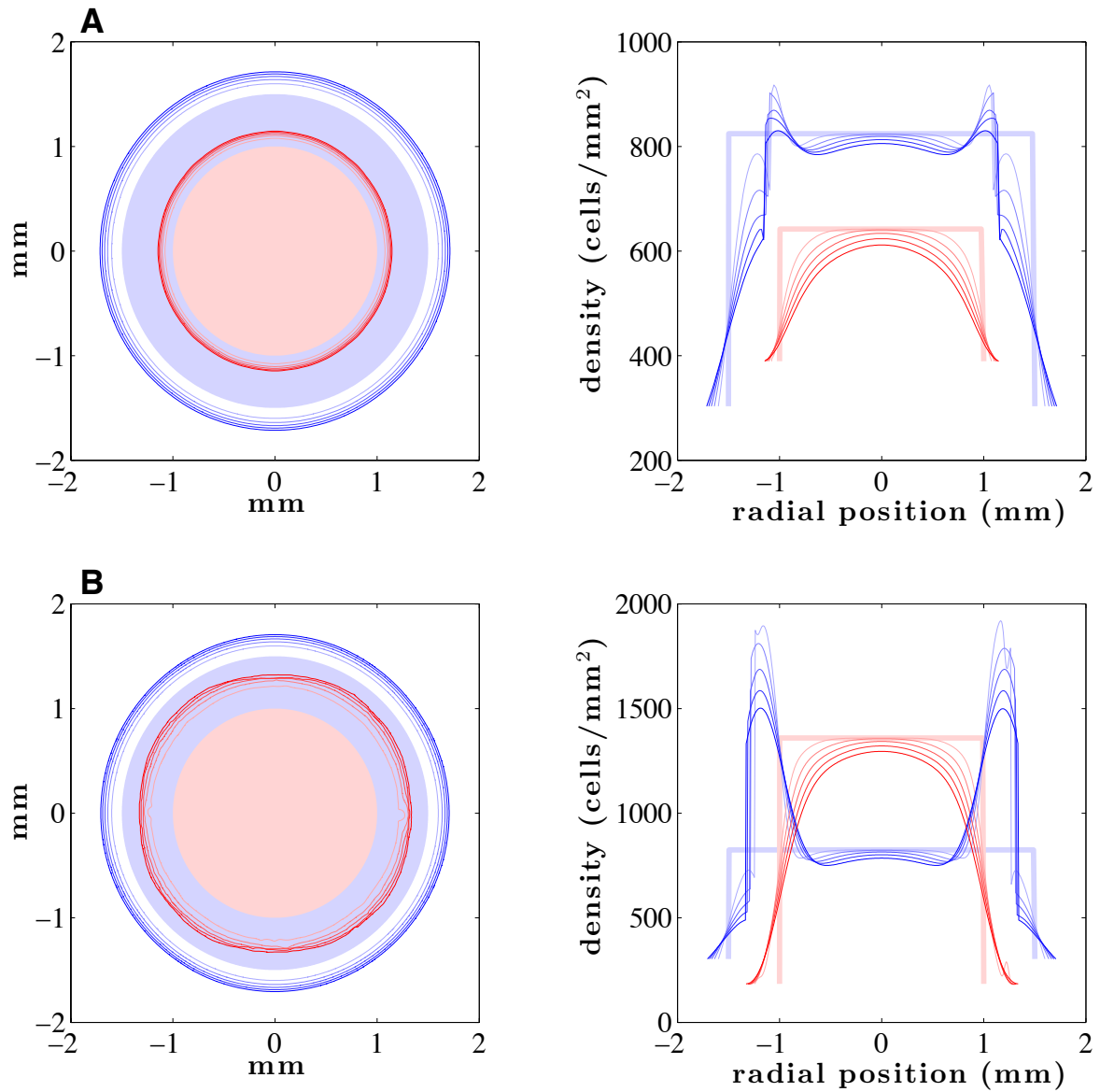


Figure 6.7: Numerical solution of the 2-D dual layer model for varying parameters. The color scheme is the same but F_2 is half or double that as in Figure 6.5 while the other parameters remain fixed, such that, respectively, (A) $\frac{F_2}{k_1} = \frac{F_2}{k_2} = 0.25$, and (B) $\frac{F_2}{k_1} = \frac{F_2}{k_2} = 1$.

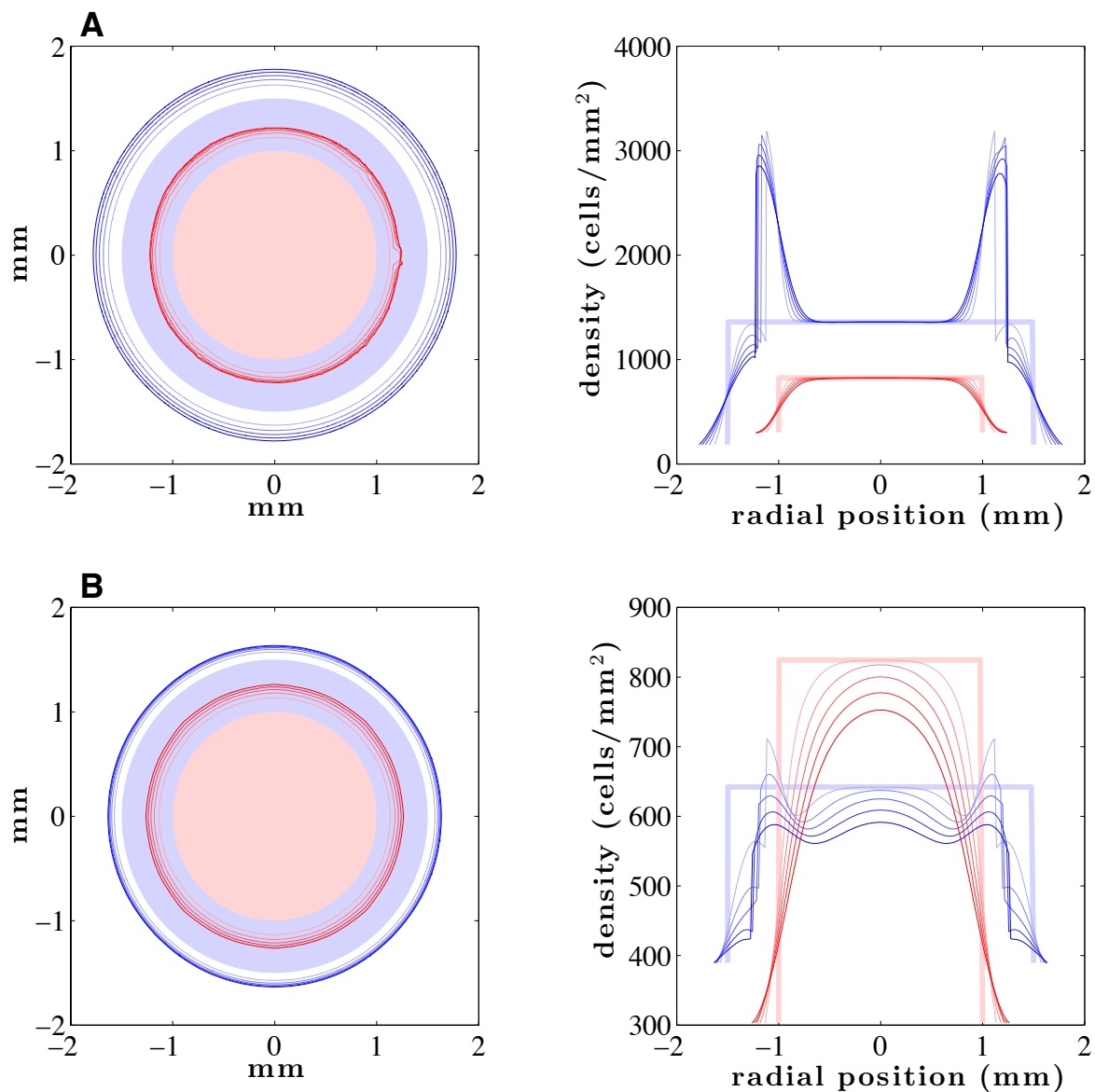


Figure 6.8: Numerical solution of the 2-D dual layer model for varying parameters. The color scheme is the same but k_1 is half or double that as in Figure 6.5 while the other parameters remain fixed, such that, respectively, (A) $\frac{F_1}{k_1} = \frac{F_2}{k_1} = 1$, $\frac{k_1}{b_1} = 2500 \frac{\mu\text{m}^2}{h}$, and (B) $\frac{F_1}{k_1} = \frac{F_2}{k_1} = 0.25$, $\frac{k_1}{b_1} = 10000 \frac{\mu\text{m}^2}{h}$.

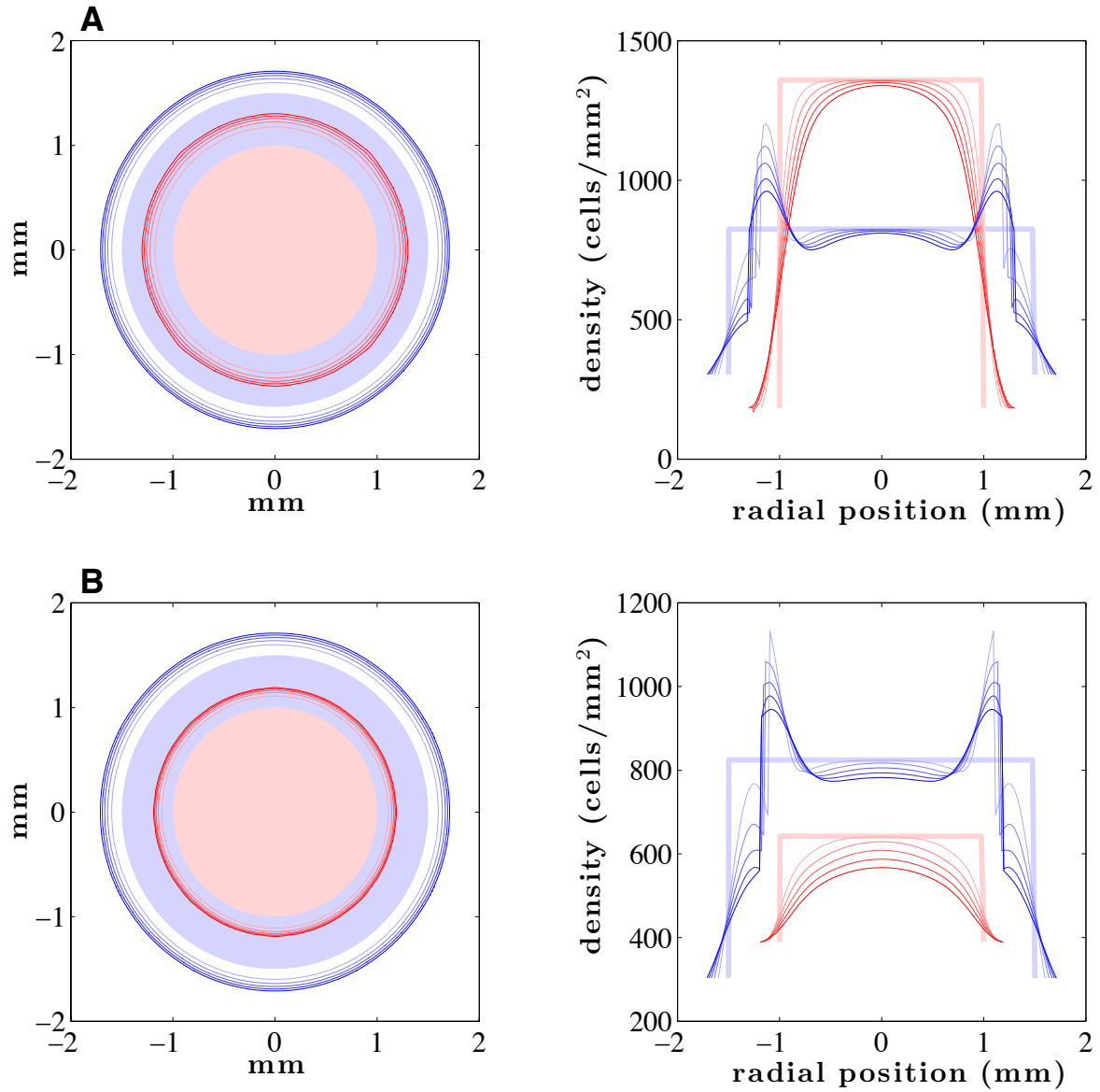


Figure 6.9: Numerical solution of the 2-D dual layer model for varying parameters. The color scheme is the same but k_2 is half or double that as in Figure 6.5 while the other parameters remain fixed, such that, respectively, (A) $\frac{F_2}{k_2} = 1$, $\frac{k_2}{b_1} = \frac{k_2}{b_2} = 2500 \frac{\mu\text{m}^2}{h}$, and (B) $\frac{F_2}{k_2} = 0.25$, $\frac{k_2}{b_1} = \frac{k_2}{b_2} = 10000 \frac{\mu\text{m}^2}{h}$.

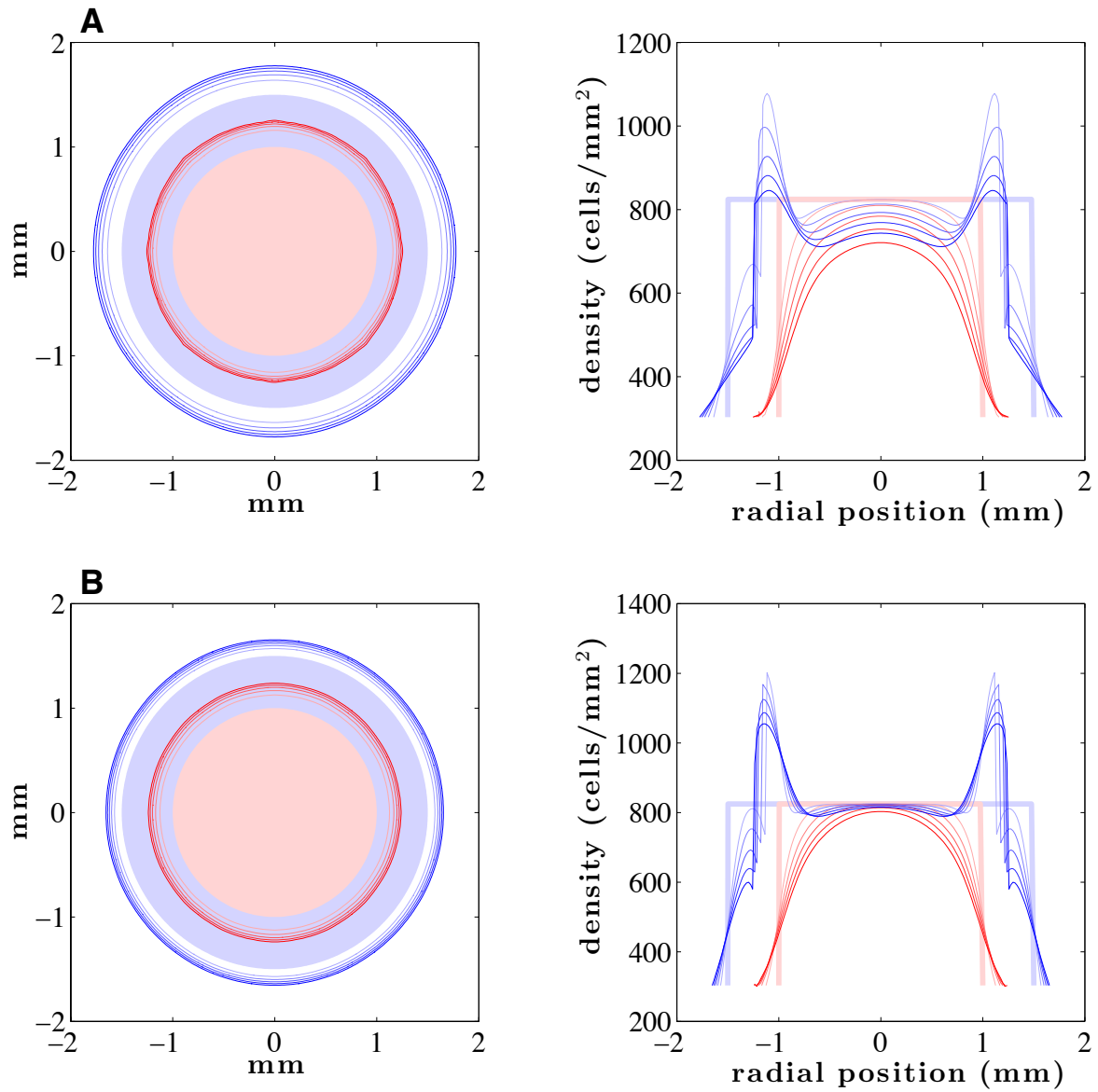


Figure 6.10: Numerical solution of the 2-D dual layer model for varying parameters. The color scheme is the same but b_1 is half or double that as in Figure 6.5 while the other parameters remain fixed, such that, respectively, (A) $\frac{k_1}{b_1} = \frac{k_2}{b_1} = 10000 \frac{\mu\text{m}^2}{h}$, and (B) $\frac{k_1}{b_1} = \frac{k_2}{b_1} = 2500 \frac{\mu\text{m}^2}{h}$.

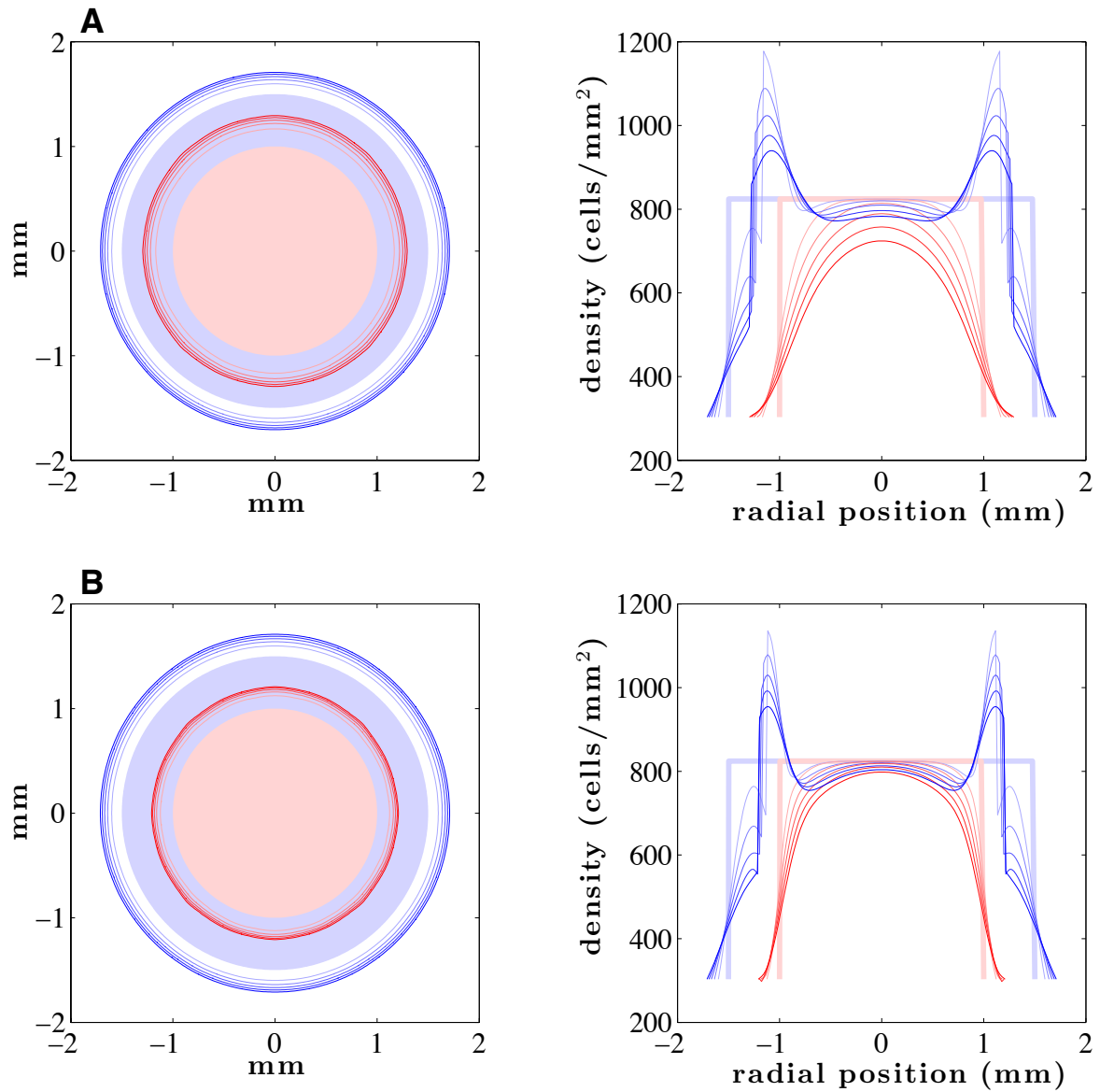


Figure 6.11: Numerical solution of the 2-D dual layer model for varying parameters. The color scheme is the same but b_2 is half or double that as in Figure 6.5 while the other parameters remain fixed, such that, respectively, (A) $\frac{k_2}{b_2} = 10000 \frac{\mu\text{m}^2}{h}$, and (B) $\frac{k_2}{b_2} = 2500 \frac{\mu\text{m}^2}{h}$.

Table 6.2: *Relative difference in area of the 2-D dual layer numerical solutions for the bottom and top layers in the simulations with the same initial geometry but different parameters. The parameters for the control case are $\frac{F_1}{k_1} = \frac{F_2}{k_2} = \frac{F_2}{k_1} = 0.5$ (dimensionless), $\frac{k_1}{b_1} = \frac{k_2}{b_2} = \frac{k_2}{b_1} = 5000 \frac{\mu\text{m}^2}{h}$, and $\rho_{01} = \rho_{02} = 500 \frac{\text{cells}}{\mu\text{m}^2}$. The relative difference between the control case and the other simulations is calculated at $t = 10$ hours. All values are in units of μm^2 . cf. Figures 6.5–6.11.*

Parameters	Bottom Layer		Top Layer	
	Final Area	Rel. Diff.	Final Area	Rel. Diff.
control	0.9188×10^7		4.8364×10^6	
F_1 halved	0.8065×10^7	0.1223	4.9477×10^6	0.0230
F_1 doubled	1.1253×10^7	0.2247	4.6229×10^6	0.0441
F_2 halved	0.9235×10^7	0.0051	4.1167×10^6	0.1488
F_2 doubled	0.9136×10^7	0.0056	5.7008×10^6	0.1787
k_1 halved	0.9947×10^7	0.0825	4.7328×10^6	0.0214
k_1 doubled	0.8377×10^7	0.0883	4.9909×10^6	0.0319
k_2 halved	0.9173×10^7	0.0016	5.3116×10^6	0.0983
k_2 doubled	0.9204×10^7	0.0017	4.4102×10^6	0.0881
b_1 halved	0.9905×10^7	0.0780	4.8847×10^6	0.0100
b_1 doubled	0.8606×10^7	0.0634	4.7895×10^6	0.0097
b_2 halved	0.9170×10^7	0.0020	5.2465×10^6	0.0848
b_2 doubled	0.9199×10^7	0.0011	4.5526×10^6	0.0587

6.1 LEVEL SET METHOD

The level set method was first introduced by Osher and Sethian [49] and applied to Stefan problems by Chen et al. [11], among others. Arciero et al. [3] based their numerical method for solving the two-dimensional spatial formulation of single cell layer migration on the method of Javierre et al. [33]. We extend this numerical method to include two adhering

cell layers to solve the two-dimensional dual layer model equations (Model 3) by employing a domain decomposition method to account for where the migrating cells in each layer are located.

The level set method tracks a moving boundary, which is represented as the zero level set of a smooth function, on a fixed grid. Recalling the schematic in Figure 5.1, the moving boundaries are $\partial\Omega_1^t$ and $\partial\Omega_2^t$ and we denote their corresponding level set functions as Φ_1 and Φ_2 , respectively. Initially these level set functions describe the signed distance d from each grid point to the boundary, where the functions are positive if there are cells in that location, zero on the boundary, or negative otherwise. In other words,

$$\Phi_1(\mathbf{x}, 0) = \begin{cases} d(\mathbf{x}, \partial\Omega_1^0), & \mathbf{x} \in \Omega_1^0 \\ 0, & \mathbf{x} \in \partial\Omega_1^0 \\ -d(\mathbf{x}, \partial\Omega_1^0), & \mathbf{x} \notin \Omega_1^0 \end{cases}, \quad \Phi_2(\mathbf{x}, 0) = \begin{cases} d(\mathbf{x}, \partial\Omega_2^0), & \mathbf{x} \in \Omega_2^0 \\ 0, & \mathbf{x} \in \partial\Omega_2^0 \\ -d(\mathbf{x}, \partial\Omega_2^0), & \mathbf{x} \notin \Omega_2^0 \end{cases}. \quad (6.1)$$

Examples of level set functions are listed in Table 6.3. If the initial boundary is specified in terms of position coordinates, then the distance from any grid node to a boundary is calculated as the minimum Euclidean distance from the grid node position to all the position coordinates. Due to the existence of an interface condition but not a boundary condition for the bottom layer on $\partial\Omega_2^t$, in our simulations we cannot have $\Phi_2(\mathbf{x}, 0) = 0$ on any of the grid nodes.

We note, for clarity later in this section, that there is an expression for the distance from the moving boundary to neighboring grid nodes that depends on the level set function. For example, assume $\mathbf{x}_f = (x_f, j\Delta y)$, for some integer j , is a point on $\partial\Omega_1^t$ or $\partial\Omega_2^t$. The distances between \mathbf{x}_f and the two neighboring grid nodes in the x -direction $\mathbf{x}_{i,j}$ and $\mathbf{x}_{i+1,j}$, such that $x_i < x_f < x_{i+1}$, are calculated by

$$x_{i+1} - x_f = \left(\frac{\Phi_{i+1,j}}{\Phi_{i+1,j} - \Phi_{i,j}} \right) \Delta x, \quad (6.2a)$$

$$x_f - x_i = - \left(\frac{\Phi_{i,j}}{\Phi_{i+1,j} - \Phi_{i,j}} \right) \Delta x. \quad (6.2b)$$

We take the initial domain to be rectangular with a uniform mesh. Let n_x be the number of grid nodes and Δx the grid spacing in the x -direction, and let n_y be the number of grid

Table 6.3: Examples of level set functions Φ for various initial geometries in the case of cell colony growth. For wound healing, use $-\Phi$. Here, $\mathbf{x} = (x, y)$ is the coordinate position of a grid node and (x_0, y_0) denotes the coordinate position of the center of the shape.

Shape	$\Phi(\mathbf{x}, \mathbf{y})$	Meaning of Variables
circle	$r - \sqrt{(x - x_0)^2 + (y - y_0)^2}$	$r = \text{radius}$
annulus	$\frac{r_{\text{out}} - r_{\text{in}}}{2} - \left \sqrt{(x - x_0)^2 + (y - y_0)^2} - \frac{r_{\text{out}} + r_{\text{in}}}{2} \right $	$r_{\text{in}} = \text{inner radius}$ $r_{\text{out}} = \text{outer radius}$
ellipse	$r_x - \sqrt{(x - x_0)^2 + \left(\frac{r_x}{r_y}\right)^2 (y - y_0)^2}$	$r_x = \text{radius in } x\text{-direction}$ $r_y = \text{radius in } y\text{-direction}$
rectangle	$-\max \left\{ x - x_0 - \frac{\ell_x}{2}, y - y_0 - \frac{\ell_y}{2} \right\}$	$\ell_x = \text{length in } x\text{-direction}$ $\ell_y = \text{length in } y\text{-direction}$
astroid	$r^{2/3} - \left((x - x_0)^{2/3} + (y - y_0)^{2/3} \right)$	$r = \text{radius}$
p -norm ball	$r - (x - x_0 ^p + y - y_0 ^p)^{1/p}$	$r = \text{radius}$
rose	$A \cos \left(k \arctan \left(\frac{y}{x} \right) \right) + z$ $-\sqrt{(x - x_0)^2 + (y - y_0)^2}$	$A = \text{petal amplitude}$ $k = \text{number of petals}$ $z = \text{inner petal distance}$

nodes and Δy the grid spacing in the y -direction. We denote the time step as Δt , which is adaptive, and we assume that the top layer of cells never migrates past the bottom layer of cells.

The first step of the algorithm involves moving the level set functions Φ_1 and Φ_2 with velocity determined by the Stefan conditions (5.13). Recall that the Stefan conditions are expressions for the velocity of only the moving boundaries. The velocity $\mathbf{v} = (v^x, v^y, v^\eta, v^\zeta)$ for each boundary is computed, respectively, in the standard Cartesian coordinates x, y and the 45°-rotated coordinates η, ζ , since the four coordinate directions reduce grid orientation effects (Chen et al. [11]). The algorithm for the discretization of v^x , for example, is as follows. If cells from only one layer are located at grid node (i, j) , then

- If $\Phi_{i,j-1} < 0$ and $\Phi_{i,j+1} < 0$, let $r_1 = \frac{\Phi_{i,j}}{\Phi_{i,j} - \Phi_{i,j-1}}$ and $r_2 = \frac{-\Phi_{i,j}}{\Phi_{i,j+1} - \Phi_{i,j}}$.
 - ◊ If $r_1 = 0$, then $v_{i,j-1}^x = 0$, else $v_{i,j-1}^x = \frac{D}{Br_1 \Delta x} (B - \rho_{i,j})$.

- ◇ **If** $r_2 = 0$, **then** $v_{i,j+1}^x = 0$, **else** $v_{i,j+1}^x = \frac{D}{Br_2\Delta x}(\rho_{i,j} - B)$.
- ◇ **If** $r_1 < r_2$, **then** $v_{i,j}^x = v_{i,j-1}^x$, **else** $v_{i,j}^x = v_{i,j+1}^x$.
- **Else if** $\Phi_{i,j-1} < 0$, let $r = \frac{\Phi_{i,j}}{\Phi_{i,j} - \Phi_{i,j-1}}$.
 - ◇ **If** $r \leq TOL$, **then** $v_{i,j}^x = \frac{D}{B(1+r)\Delta x}(B - \rho_{i,j+1})$, **else** $v_{i,j}^x = \frac{D}{Br\Delta x}(B - \rho_{i,j})$.
 - ◇ Set $v_{i,j-1}^x = v_{i,j}^x$.
- **Else if** $\Phi_{i,j+1} < 0$, let $r = \frac{-\Phi_{i,j}}{\Phi_{i,j+1} - \Phi_{i,j}}$.
 - ◇ **If** $r \leq TOL$, **then** $v_{i,j}^x = \frac{D}{B(1+r)\Delta x}(\rho_{i,j-1} - B)$, **else** $v_{i,j}^x = \frac{D}{Br\Delta x}(\rho_{i,j} - B)$.
 - ◇ Set $v_{i,j+1}^x = v_{i,j}^x$.

If we are calculating the velocity of the boundary of the bottom layer, then $D = \frac{k_1}{b_1}$ and $B = \rho_{01}e^{-F_1/k_1}$ (see Equation (5.11a)). If we are calculating the velocity of the boundary of the top layer, then $D = \frac{k_2}{b_1} + \frac{k_2}{b_2}$ and $B = \rho_{02}e^{-F_2/k_2}$ (see Equation (5.11b)). TOL is a small value, less than Δx , that specifies a different discretization depending on how close the grid node (i, j) is to the boundary to reduce numerical error.

However, if cells from both layers are located at grid node (i, j) , then

- **If** $\Phi_{i,j-1} < 0$ and $\Phi_{i,j+1} < 0$, let $r_1 = \frac{\Phi_{i,j}}{\Phi_{i,j} - \Phi_{i,j-1}}$, $R_1 = \frac{2r_1 - \Delta x}{2r_1 + \Delta x}$, $r_2 = \frac{-\Phi_{i,j}}{\Phi_{i,j+1} - \Phi_{i,j}}$, and $R_2 = \frac{2r_2 + \Delta x}{2r_2 - \Delta x}$.
 - ◇ **If** $r_1 = 0$, **then** $v_{i,j-1}^x = 0$, **else**

$$v_{i,j-1}^x = \frac{D}{Br_1\Delta x}(B - \rho_{i,j}) + \frac{\hat{D}}{\hat{\rho}_{i,j}} \left(\frac{E}{(1-R_1)\Delta x} \hat{\rho}_{i,j-1} - (1 + R_1) \hat{\rho}_{i,j} + R_1 E \hat{\rho}_{i,j+1} \right).$$
 - ◇ **If** $r_2 = 0$, **then** $v_{i,j+1}^x = 0$, **else**

$$v_{i,j+1}^x = \frac{D}{Br_2\Delta x}(\rho_{i,j} - B) + \frac{\hat{D}}{\hat{\rho}_{i,j}} \left(\frac{E}{(1-R_2)\Delta x} \hat{\rho}_{i,j-1} - (1 + R_2) \hat{\rho}_{i,j} + R_2 E \hat{\rho}_{i,j+1} \right).$$
 - ◇ **If** $r_1 < r_2$, **then** $v_{i,j}^x = v_{i,j-1}^x$, **else** $v_{i,j}^x = v_{i,j+1}^x$.
- **Else if** $\Phi_{i,j-1} < 0$, let $r = \frac{\Phi_{i,j}}{\Phi_{i,j} - \Phi_{i,j-1}}$ and $R = \frac{2r - \Delta x}{2r + \Delta x}$.
 - ◇ **If** $r \leq TOL$, **then**

$$v_{i,j}^x = \frac{D}{B(1+r)\Delta x}(B - \rho_{i,j+1}) + \frac{\hat{D}}{\hat{\rho}_{i,j}} \left(\frac{E}{(1-R)\Delta x} \hat{\rho}_{i,j-1} - (1 + R) \hat{\rho}_{i,j} + R \hat{\rho}_{i,j+1} \right),$$
 else

$$v_{i,j}^x = \frac{D}{Br\Delta x}(B - \rho_{i,j}) + \frac{\hat{D}}{\hat{\rho}_{i,j}} \left(\frac{E}{(1-R)\Delta x} \hat{\rho}_{i,j-1} - (1 + R) \hat{\rho}_{i,j} + R \hat{\rho}_{i,j+1} \right)$$
 - ◇ Set $v_{i,j-1}^x = v_{i,j}^x$.
- **Else if** $\Phi_{i,j+1} < 0$, let $r = \frac{-\Phi_{i,j}}{\Phi_{i,j+1} - \Phi_{i,j}}$ and $R = \frac{2r + \Delta x}{2r - \Delta x}$.

◇ **If $r \leq TOL$, then**

$$v_{i,j}^x = \frac{D}{B(1+r)\Delta x}(\rho_{i,j-1} - B) + \frac{\hat{D}}{\hat{\rho}_{i,j}} \left(\frac{1}{(1-R)\Delta x} \hat{\rho}_{i,j-1} - (1+R)\hat{\rho}_{i,j} + RE\hat{\rho}_{i,j+1} \right), \text{ else}$$

$$v_{i,j}^x = \frac{D}{Br\Delta x}(\rho_{i,j} - B) + \frac{\hat{D}}{\hat{\rho}_{i,j}} \left(\frac{1}{(1-R)\Delta x} \hat{\rho}_{i,j-1} - (1+R)\hat{\rho}_{i,j} + RE\hat{\rho}_{i,j+1} \right).$$

◇ Set $v_{i,j+1}^x = v_{i,j}^x$.

Here, $\hat{\rho}$ is the density of the other layer, and D , B , and TOL are as above. If we are calculating the velocity of the boundary the bottom layer, then $\hat{D} = \frac{k_2}{b_1} + \frac{k_2}{b_2}$ and $E = e^{-F_2/k_2}$ (see Equation (5.15)). If we are calculating the velocity of the boundary of the top layer, then $\hat{D} = \frac{k_1}{b_1}$ and $E = e^{F_2/k_2}$ (see Equation (5.15)).

Note that for the discretizations of v^y , v^η , and v^ζ , the following substitutions from the discretization of v^x are made.

$$\begin{aligned} v^y : \quad & \Delta x \mapsto \Delta y, & (i, j-1) & \mapsto (i-1, j), & (i, j+1) & \mapsto (i+1, j) \\ v^\eta : \quad & \Delta x \mapsto \sqrt{(\Delta x)^2 + (\Delta y)^2}, & (i, j-1) & \mapsto (i-1, j-1), & (i, j+1) & \mapsto (i+1, j+1) \\ v^\zeta : \quad & \Delta x \mapsto \sqrt{(\Delta x)^2 + (\Delta y)^2}, & (i, j-1) & \mapsto (i+1, j-1), & (i, j+1) & \mapsto (i-1, j+1) \end{aligned}$$

The velocity components are then continuously extended off the boundary to the entire domain for each layer via the advection equations

$$\frac{\partial v^x}{\partial \tau} + \text{sign}(\Phi \Phi_x) \frac{\partial v^x}{\partial x} = 0, \quad (6.3a)$$

$$\frac{\partial v^y}{\partial \tau} + \text{sign}(\Phi \Phi_y) \frac{\partial v^y}{\partial y} = 0, \quad (6.3b)$$

$$\frac{\partial v^\eta}{\partial \tau} + \text{sign}(\Phi \Phi_\eta) \frac{\partial v^\eta}{\partial \eta} = 0, \quad (6.3c)$$

$$\frac{\partial v^\zeta}{\partial \tau} + \text{sign}(\Phi \Phi_\zeta) \frac{\partial v^\zeta}{\partial \zeta} = 0, \quad (6.3d)$$

where τ is a pseudo-time. These equations are discretized with a first-order upwind scheme. The time step $\Delta\tau$ is arbitrary and independent of the main time step Δt , but it must satisfy the Courant-Friedrichs-Lewy (CFL) condition $\frac{\Delta\tau}{\min\{\Delta x, \Delta y\}} \leq 1$. A fixed number of pseudo-time iterations is carried out to reduce computational cost.

Once the components of the (now continuously extended) velocity \mathbf{v} for each layer have been obtained, we propagate each level set function via

$$\frac{\partial \Phi}{\partial t} + \mathbf{v} \|\nabla \Phi\| = 0, \quad (6.4)$$

which is solved using a forward Euler discretization in time and weighted essentially non-oscillatory (WENO) approximations to the spatial derivatives. This discretization leads to a CFL condition on the main time step

$$\Delta t \max_{\text{layer 1, layer 2}} \left\{ \frac{\|v^x\|_\infty}{\Delta x} + \frac{\|v^y\|_\infty}{\Delta y} + \frac{\|v^{\eta}\|_\infty}{\sqrt{\Delta x^2 + \Delta y^2}} + \frac{\|v^{\zeta}\|_\infty}{\sqrt{\Delta x^2 + \Delta y^2}} \right\} < 1, \quad (6.5)$$

where we define $\|\cdot\|_\infty$ as the maximum norm and we take the maximum sum over both layers. The main time step Δt is updated each iteration based on this condition.

The level set functions in general cease to be exact distance functions, i.e. $\|\nabla\Phi\| \neq 1$, even after one time step (Sussman et al. [70]). To avoid steep or flat gradients in Φ near the moving boundaries, the level set functions are reinitialized to be exact distance functions from the moving boundary at every time step. Given a function Φ_0 that is not an exact distance function, we can evolve it into an exact distance function by iterating the following to steady state

$$\frac{\partial\Phi}{\partial\tau} = \overline{\text{sign}}(\Phi_0)(1 - \|\nabla\Phi\|), \quad (6.6a)$$

$$\Phi(\mathbf{x}, 0) = \Phi_0(\mathbf{x}). \quad (6.6b)$$

Here, τ is a pseudo-time and $\overline{\text{sign}}$ is the smooth sign function $\overline{\text{sign}}(x) = \frac{x}{\sqrt{x^2 + \epsilon^2}}$. The equation is discretized using Godunov's method in pseudo-time, a third-order Runge-Kutta scheme in real time, and fifth-order WENO approximations for the spatial gradient. Only 3–10 iterations are needed for sufficient accuracy to evolve Φ to an exact distance function (Javierre et al. [33]). At this point we verify that the top layer does not extend further than the bottom layer to satisfy our model assumptions, otherwise the program is exited.

After the level set functions Φ_1 and Φ_2 have moved the correct velocity at the moving boundary and been reinitialized as exact distance functions, we solve (5.10) for the density of each cell layer over the entire domain using a finite difference scheme with adjustments for grid nodes near the boundary. We also use domain decomposition to solve the governing equations separately on the two disjoint nonoverlapping domains $\Omega_1^t \cap \Omega_2^t$, where there is a system of two coupled equations, and $\Omega_1^t \setminus \Omega_2^t$, where there is a single uncoupled equation (see Figure 6.12).

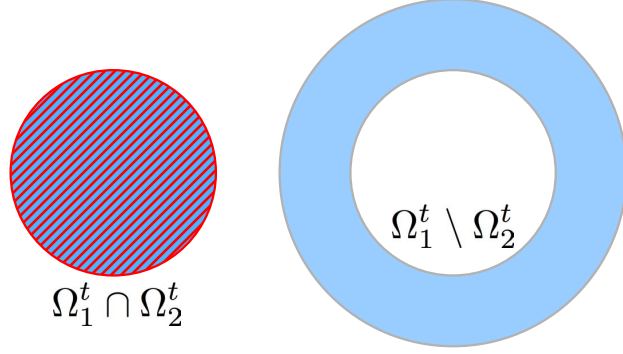


Figure 6.12: *Domain decomposition of the 2-D dual layer problem: Since there is a system of two coupled equations in the domain $\Omega_1^t \cap \Omega_2^t$ but a single uncoupled equation in the domain $\Omega_1^t \setminus \Omega_2^t$, we decompose the entire domain into these two disjoint nonoverlapping domains and solve the governing equations independently on each domain.*

We first create matrices representing the discrete Laplacians for $\frac{k_1}{b_1} \Delta \rho_1$, $\frac{k_2}{b_1} \Delta \rho_2$, and $\left(\frac{k_2}{b_1} + \frac{k_2}{b_2}\right) \Delta \rho_1$ using the standard 5-point stencil scheme (Chen et al. [11]), but we update the rows that correspond to grid nodes near the moving boundary or outside of the actual domain. A cut-cell method is used to adapt the grid to the location of the domains by “cutting” grid nodes that are not located within the domain (Javierre et al. [33]). In practice, this means setting equal to zero those rows of the discretized Laplacian matrix that correspond to any grid node not in the domain.

For grid nodes that border the moving boundaries, the standard 5-point stencil scheme is adjusted using interpolating polynomials and one-sided differencing with values of Φ near the interface, the boundary conditions (5.11), and the interface condition (5.15) (Chen et al. [11]). To incorporate the interface condition (5.15) into the discretization, we use the additive Schwarz method for Dirichlet conditions with one iteration (Quarteroni [54], Geiser [24], Toselli and Widlund [76]). For example, for discretization in the domain $\Omega_1^t \cap \Omega_2^t$, if $\mathbf{x}_f = (x_f, j\Delta y)$, for some integer j , is a point on $\partial\Omega_2^t$ and cells in the top layer are located at the grid node $\mathbf{x}_{i,j}$ but not the grid node $\mathbf{x}_{i+1,j}$, such that $x_i < x_f < x_{i+1}$, then the value of the density of the bottom layer on the boundary $\partial\Omega_2^t$ is calculated as $e^{F_2/k_1} \rho_{i+1,j}$, where ρ is from the previous time step. Correspondingly, for discretization in the domain $\Omega_1^t \setminus \Omega_2^t$,

the value of the density of the bottom layer on the boundary $\partial\Omega_2^t$ is calculated as $e^{-F_2/k_1}\rho_{i,j}$, where ρ is from the previous time step. We note that, unlike in the discretization of the velocity of the level sets, we use the same discretization no matter how close a grid node is to the moving boundary.

Using the backward Euler method for time integration, we obtain two linear systems, one which solves the two coupled equations on $\Omega_1^t \cap \Omega_2^t$ for $\rho_1|_{\Omega_1^t \cap \Omega_2^t}$ and ρ_2 , and one which solves the single uncoupled equation on $\Omega_1^t \setminus \Omega_2^t$ for $\rho_1|_{\Omega_1^t \setminus \Omega_2^t}$. The density of the bottom layer is obtained by simply adding together $\rho_1|_{\Omega_1^t \cap \Omega_2^t} + \rho_1|_{\Omega_1^t \setminus \Omega_2^t}$.

6.1.1 Analysis of the Numerical Method

One of largest issues with the level set method we presented is mesh refinement. If the mesh is too coarse, blow up can occur near the moving boundary. However, computer limitations restrict how fine a mesh may be.

Our numerical code is written in MATLAB, which has limits on memory allotment and maximum allowed array size. For example, with MATLAB Version 7.4 (R2007A), the largest number of elements in a real double array is bounded by approximately 2×10^8 for 32-bit Windows XP or Vista, or Mac OS X running 32-bit MATLAB; 3×10^8 for 32-bit Linux, 64-bit Linux running 32-bit MATLAB, or 64-bit Windows XP running 32-bit MATLAB; 4×10^8 for Solaris running 32-bit MATLAB; 2×10^9 for 64-bit Windows XP, Linux, or Solaris running 64-bit MATLAB Version 7.4 and earlier; and 3×10^{14} for 64-bit Windows XP, Linux, or Solaris running 64-bit MATLAB Version 7.5 and later (MathWorks [41]). Note that these values depend primarily on the total amount of memory MATLAB has available for all of the variables in the workspace, and additional random-access memory (RAM) installed on a machine with a 32-bit operating system or 32-bit version of MATLAB will not increase the total amount of available memory.

If our grid size is $n_y \times n_x$, then the discrete Laplacian matrices are size $n_x n_y \times n_x n_y$, and thus they have $(n_x n_y)^2$ elements. If $(n_x n_y)^2$ is larger than the maximum allowed array size, then our mesh cannot be refined to be $n_y \times n_x$.

However, refining the mesh may not be viable due to the computational time. Table 6.4

Table 6.4: *Elapsed CPU time for numerical solutions of the 2-D dual layer model for varying mesh sizes. Simulations on a $5000\mu\text{m} \times 5000\mu\text{m}$ domain are compared for various grid sizes which correspond to the grid spacings Δx and Δy , which are equal in this case. cf. Figures 6.13–6.14.*

Grid Size	Grid Spacing (μm)	CPU Time
25 \times 25	208.3333	3.6 sec
50 \times 50	102.0408	6.1 sec
100 \times 100	50.5051	24.6 sec
200 \times 200	25.1256	2.7 min
300 \times 300	16.7224	10.5 min
400 \times 400	12.5313	30.4 min
500 \times 500	10.0200	1.2 hr
600 \times 600	8.3472	2.9 hr
700 \times 700	7.1531	5.6 hr

lists the elapsed central processing unit (CPU) time on a Dell Precision T3500 Workstation with quad-core 2.66GHz processor and 12 GB memory, running 64-bit Ubuntu 12.04 LTS and 64-bit MATLAB Version R2012a for various mesh sizes. The results of the simulations for a portion of the respective mesh sizes are shown in Figures 6.13–6.14. It is clear that for mesh sizes too small, the solution may not stay bounded, as in Figure 6.13A. As the mesh is refined, the solution becomes more smooth. However, the solution in the most refined mesh shown in Figure 6.14C still has some roughness to its boundaries upon very close examination on a magnified scale, but refining the mesh more would require more than 6 hours of elapsed CPU time, which is not very practical. On average, a grid size of 200 \times 200 appears to give the most reliable results for the least amount of elapsed CPU time, and furthermore the size of the discrete Laplacians remain less than the maximum array size on almost all operating systems and MATLAB versions.

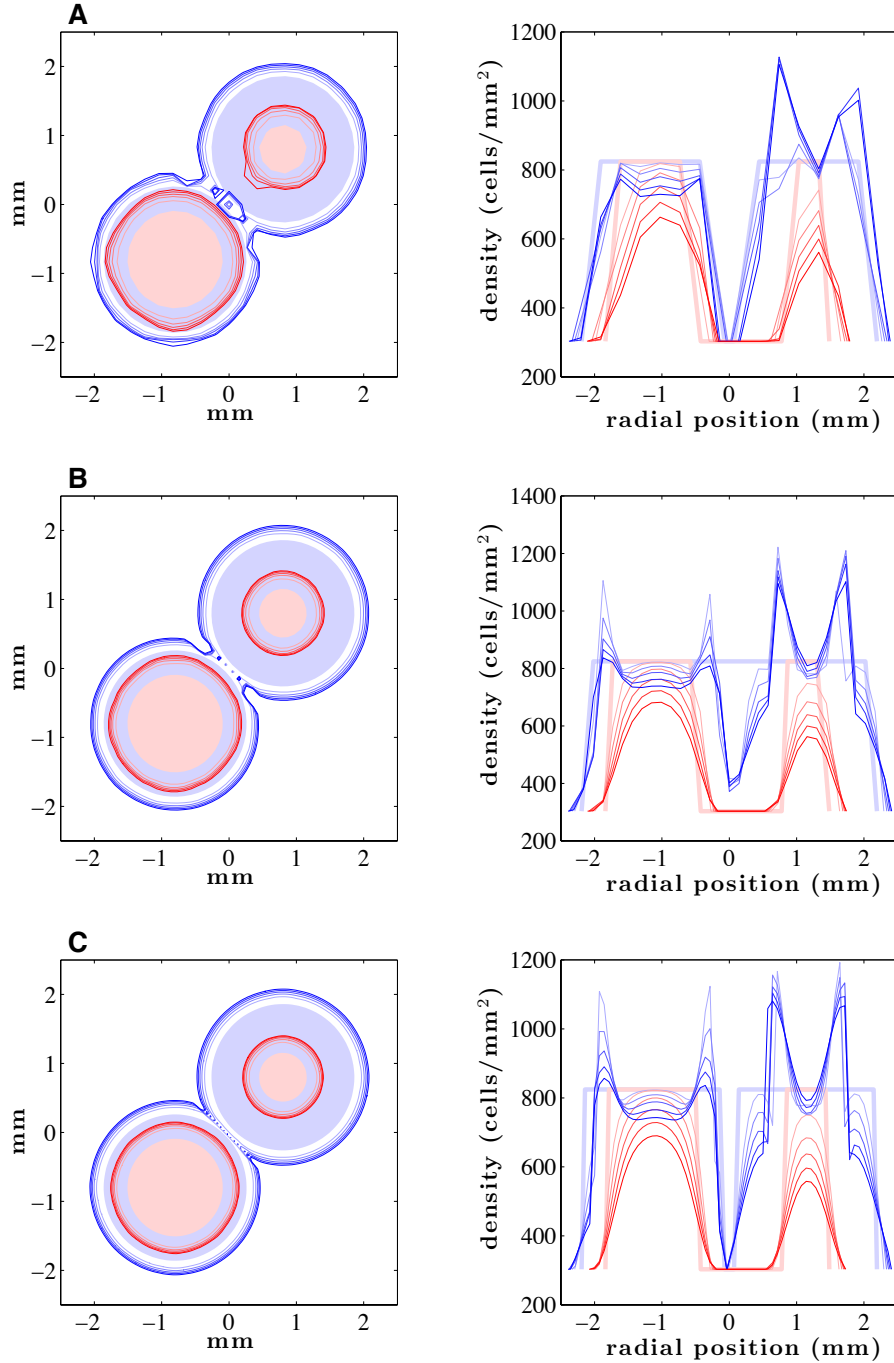


Figure 6.13: Numerical solution of the 2-D dual layer model for varying mesh sizes. Here, $\frac{F_1}{k_1} = \frac{F_2}{k_2} = \frac{F_2}{k_1} = 0.5$ (dimensionless), $\frac{k_1}{b_1} = \frac{k_2}{b_2} = \frac{k_2}{b_1} = 5000 \frac{\mu\text{m}^2}{h}$, and $\rho_{01} = \rho_{02} = 0.0005 \frac{\text{cells}}{\mu\text{m}^2}$. The top layer is in red and the bottom layer is in blue. The shaded regions indicate where the cells are initially seeded. The curves are drawn at every 2 hours from 2 to 10 hours, where the lightest curve is at $t = 2$ and the darkest curve is at $t = 10$. The first column shows the position of the leading edge of the migrating cell layers as seen from above, and the second column shows the density profile of the cell layers as a cross-section through the x -axis. Grid sizes are (A) 25×25 , (B) 50×50 , and (C) 100×100 .

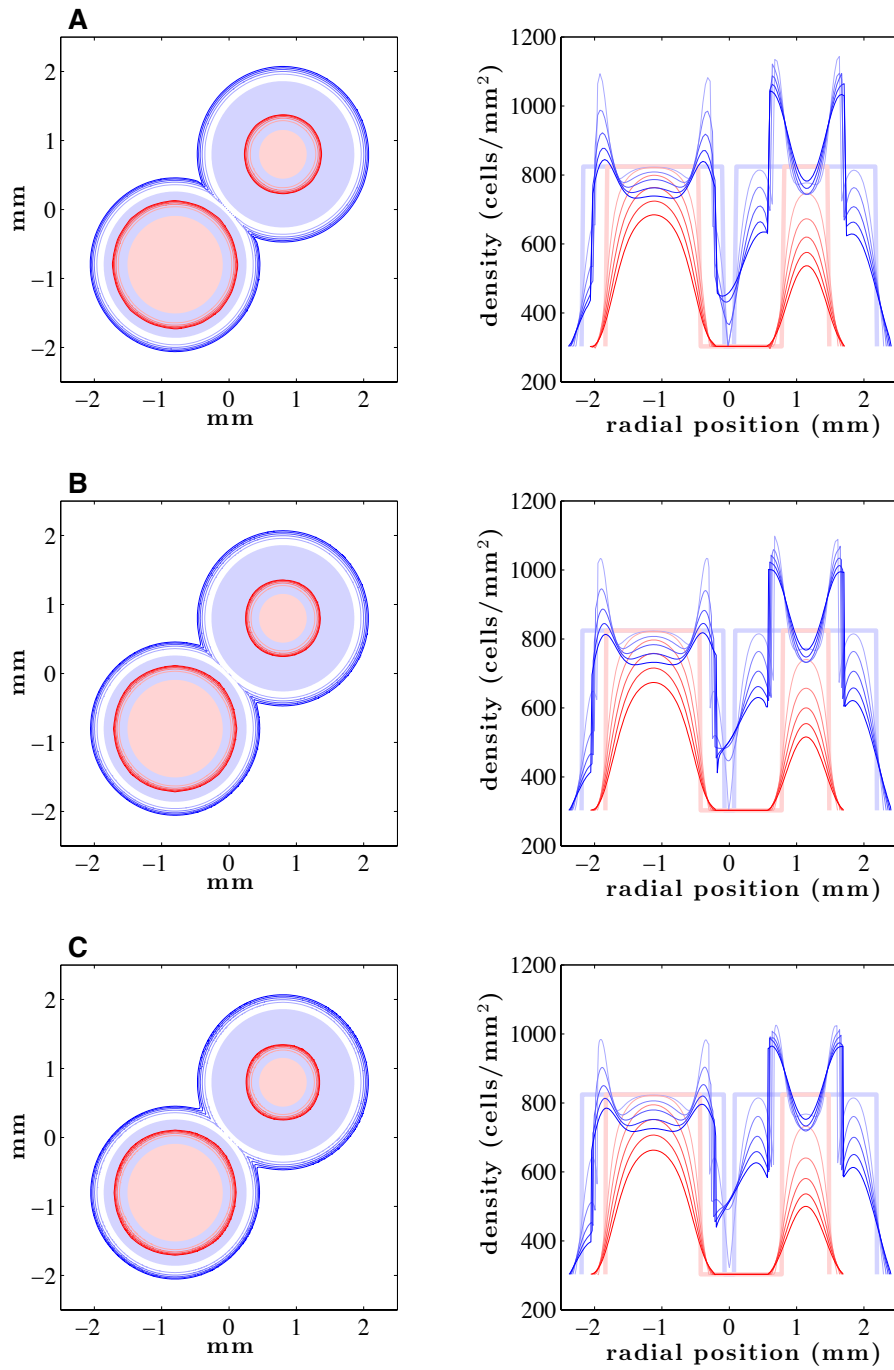


Figure 6.14: Numerical solution of the 2-D dual layer model for varying mesh sizes. Parameters and color scheme are the same as in Figure 6.13. Grid sizes are (A) 200×200 , (B) 400×400 , and (C) 700×700 .

7.0 ESTIMATING MODEL PARAMETERS FROM EXPERIMENTAL DATA

Now that we have developed a model of cell migration for two adhering layers of cells (Model 3) and a way to (numerically) solve the equations (see Section 6.1), we can apply the model to experimental data. Doing so allows us to determine properties of the cell layers that we may not be able to directly measure otherwise. Since the parameters in our continuum mechanical model correspond to physical properties, by estimating model parameter values that best represent the behavior of an experiment, we can deduce the material properties of the cell layers.

We note that not all of the model parameters k_1 , k_2 (stretching moduli), b_1 , b_2 (adhesion constants), F_1 , F_2 (net external forces), and ρ_{01} , ρ_{02} (density of the unstressed cell layers) are identifiable. In other words, since the first six parameters in the list appear in the model equations only as the ratios $\frac{F_1}{k_1}$, $\frac{F_2}{k_2}$, $\frac{F_2}{k_1}$, $\frac{b_1}{k_1}$, $\frac{b_2}{k_2}$, and $\frac{b_2}{k_1}$, we will not be able to reliably determine k_1 , k_2 , b_1 , b_2 , F_1 , and F_2 separately. Hence, we optimize the values of $\frac{F_1}{k_1}$, $\frac{F_2}{k_2}$, $\frac{F_2}{k_1}$, $\frac{b_1}{k_1}$, $\frac{b_2}{k_2}$, $\frac{b_2}{k_1}$, ρ_{01} , and ρ_{02} to determine the material properties of the cell layers. Optimal values are found by minimizing the sum of the mean-squared difference between the experimental and predicted cell layer edge positions and the mean-squared difference between the experimental and predicted densities.

7.1 EXPERIMENTAL SETUP

The data to which we apply our continuum mechanical model of single and dual cell layer migration was provided by the Davidson Lab at the University of Pittsburgh, and we briefly

describe their experimental setup in this section. The lab maintains a colony of African claw-toed frogs, *Xenopus laevis*, under the Institutional Animal Care and Use Committee (IACUC) of the University of Pittsburgh (Protocol #12020250). Eggs are obtained and fertilized through standard methods, and then fertilized eggs are cultured in standard media until they reach gastrula stages (Sive et al. [67]). Select embryos are transferred to explant culture media. Desired tissue explants, consisting of an outer epithelial layer and one inner mesenchymal layer, are microsurgically isolated and then transferred to custom culture chambers such that the mesenchymal cells contact a glass coverslip surface that has been coated with fibronectin for live time-lapse imaging (Kim and Davidson [35]). Detergent is used to cleave the epithelial cells in a microfluidic channel in the dual layer experiments shown in Section 7.3.

Time-lapse images of migrating animal cap explants are collected using a multi-position stage (Ludl XY stage and MAC 2000 controller, Ludl Electronic Products Ltd., Hawthorne, NY) and a stereomicroscope with a video port (Stemi 2000, Carl Zeiss Microscopy, LLC, Thornwood, NY) equipped with a CCD camera (CFW-1312M, Scion Corporation, Frederick, MD) under the control of automated image acquisition software, the Micro-Manager software plugin for ImageJ (Schneider et al. [60], Stuurman et al. [69], Rueden and Eliceiri [58]). Details regarding the extraction of data from the images are in the subsequent section.

While the images do not report thicknesses of the cells or tissues within the experimental samples, the samples do not change volume over the course of the experiment. Thus our assumption of uniform thickness of both cell layers in the model equations is reasonable.

7.2 PARAMETER OPTIMIZATION METHOD

We extract both the cell layer edge position and density data from time-lapse images of cell migration using the software ImageJ and Fiji (Schneider et al. [60], Schindelin et al. [59]). The edge position data is extracted from the images in one of two ways. Either the edge positions are extracted using the Fiji software plugin Level Sets, which is an image segmentation technique based on partial differential equations, or by eye. The error is expected to be less

than 5 pixels.

To calculate the difference between the experimental and computational edge positions for each cell layer, the minimum difference from each experimental point to every line segment along the computational edge is found for the j^{th} image in the time-lapse sequence and denoted $d_{1,j}$ for the bottom cell layer and $d_{2,j}$ for the top cell layer. The square root of the average of the squares of these minimum distances is calculated and denoted $D_{i,j}$, where for each cell layer $i = 1, 2$,

$$D_{i,j} = \sqrt{\sum_{n=1}^N \frac{d_{i,j}^2}{N}}, \quad (7.1)$$

where index n denotes the experimental points counted along the edge and N is the total number of these points. Summing over all time points and cell layers gives

$$z_d = \sum_{i=1}^2 \sum_{j=1}^{t_{\text{end}}} D_{i,j}. \quad (7.2)$$

Extracting the density data is more complicated. We use a method that involves calculating the strain, or local deformation, from one still image to the subsequent still image in the time-lapse sequence. Let us first review some definitions from mechanics.

Let $\mathbf{X} = (\mathbf{X}_1, \mathbf{X}_2)$ be the initial (x, y) -coordinate positions, i.e. the material coordinates, and $\mathbf{x} = (\mathbf{x}_1, \mathbf{x}_2)$ be the current (x, y) -coordinate positions, i.e. the spatial coordinates. The conservation of mass equation can be written as

$$\rho = \frac{\rho_0}{\det \mathbf{F}}, \quad (7.3)$$

where ρ is the current density, ρ_0 is the constant density of the relaxed (unstressed) cell layer, and \mathbf{F} is the deformation gradient defined as

$$\mathbf{F}(\mathbf{X}, t) = \begin{pmatrix} \frac{\partial \mathbf{x}_1(\mathbf{X}, t)}{\partial \mathbf{X}_1} & \frac{\partial \mathbf{x}_1(\mathbf{X}, t)}{\partial \mathbf{X}_2} \\ \frac{\partial \mathbf{x}_2(\mathbf{X}, t)}{\partial \mathbf{X}_1} & \frac{\partial \mathbf{x}_2(\mathbf{X}, t)}{\partial \mathbf{X}_2} \end{pmatrix}. \quad (7.4)$$

The deformation gradient is related to the displacement vector

$$\mathbf{u}(\mathbf{X}, t) = \mathbf{x}(\mathbf{X}, t) - \mathbf{X}, \quad (7.5)$$

in the following way. Since the displacement gradient is defined as

$$\nabla \mathbf{u} = \begin{pmatrix} \frac{\partial \mathbf{u}_1}{\partial \mathbf{X}_1} & \frac{\partial \mathbf{u}_1}{\partial \mathbf{X}_2} \\ \frac{\partial \mathbf{u}_2}{\partial \mathbf{X}_1} & \frac{\partial \mathbf{u}_2}{\partial \mathbf{X}_2} \end{pmatrix} = \begin{pmatrix} \frac{\partial \mathbf{x}_1}{\partial \mathbf{X}_1} & \frac{\partial \mathbf{x}_1}{\partial \mathbf{X}_2} \\ \frac{\partial \mathbf{x}_2}{\partial \mathbf{X}_1} & \frac{\partial \mathbf{x}_2}{\partial \mathbf{X}_2} \end{pmatrix} - \mathbf{I}, \quad (7.6)$$

where \mathbf{I} is the identity matrix, this implies that

$$\mathbf{F} = \nabla \mathbf{u} + \mathbf{I}. \quad (7.7)$$

Since the cells in the experiments we analyze are pigmented, we use a texture mapping strategy with the ImageJ software plugin bUnwarpJ, which is used for elastic and consistent image registration, to extract the strains (Arganda-Carreras et al. [4]). If our set of time-lapse images have width n pixels and height m pixels, then we can represent properties of each pixel by an entry in $m \times n$ matrices. For each pair of consecutive images from a time-lapse sequence, let $\mathbf{X} = (\mathbf{X}_1, \mathbf{X}_2)$ be the (x, y) -coordinate positions in the first still image, in pixels, and $\mathbf{x} = (\mathbf{x}_1, \mathbf{x}_2)$ be the (x, y) -coordinate positions in the second still image, in pixels. The top left corner of an image is the origin, and x increases from left to right and y increases from top to bottom. The entries of \mathbf{X} are therefore defined by

$$\mathbf{X}_1(i, j) = j - 1, \quad i = 1, 2, \dots, n, \quad j = 1, 2, \dots, m, \quad (7.8a)$$

$$\mathbf{X}_2(i, j) = i - 1, \quad i = 1, 2, \dots, n, \quad j = 1, 2, \dots, m. \quad (7.8b)$$

We mask the two consecutive images so that registration occurs only in the actual location of cells. We then initialize bUnwarpJ to calculate the coefficients of the cubic B-spline map β that defines the transformation $(\mathbf{X}_1, \mathbf{X}_2) \xrightarrow{\beta} (\mathbf{x}_1, \mathbf{x}_2)$. Initializing bUnwarpJ again, we apply β to \mathbf{X} by converting the transformation to “raw” data. We obtain \mathbf{x} , the mapped position of each pixel from the first image to its position in the second image, in pixels. Note that pixels outside of the mask will be mapped as well, but we remove this extraneous data after we have obtained the strains. Next, we calculate the displacement vector \mathbf{u} by

$$\mathbf{u}_1(i, j) = \mathbf{x}_1(i, j) - \mathbf{X}_1(i, j), \quad i = 1, 2, \dots, n, \quad j = 1, 2, \dots, m, \quad (7.9a)$$

$$\mathbf{u}_2(i, j) = \mathbf{x}_2(i, j) - \mathbf{X}_2(i, j), \quad i = 1, 2, \dots, n, \quad j = 1, 2, \dots, m. \quad (7.9b)$$

It is at this step that we obtain the strains. The engineering, or Cauchy, strain is defined as

$$\epsilon = \frac{\Delta L}{L_0} = \frac{L - L_0}{L_0}, \quad (7.10)$$

where ΔL is the change in length, L_0 is the original length, and L is the current length. \mathbf{u} is converted into x -strain, y -strain, xy -strain, and yx -strain by

$$\epsilon_{xx}(i, j) = \frac{\mathbf{u}_1(i, j) - \mathbf{u}_1(i - 1, j)}{\mathbf{X}_1(i, j) - \mathbf{X}_1(i - 1, j)}, \quad i = 2, 3, \dots, n, \quad j = 1, 2, \dots, m, \quad (7.11a)$$

$$\epsilon_{xy}(i, j) = \frac{\mathbf{u}_1(i, j) - \mathbf{u}_1(i, j - 1)}{\mathbf{X}_2(i, j) - \mathbf{X}_2(i, j - 1)}, \quad i = 1, 2, \dots, n, \quad j = 2, 3, \dots, m, \quad (7.11b)$$

$$\epsilon_{yx}(i, j) = \frac{\mathbf{u}_2(i, j) - \mathbf{u}_2(i - 1, j)}{\mathbf{X}_1(i, j) - \mathbf{X}_1(i - 1, j)}, \quad i = 2, 3, \dots, n, \quad j = 1, 2, \dots, m, \quad (7.11c)$$

$$\epsilon_{yy}(i, j) = \frac{\mathbf{u}_2(i, j) - \mathbf{u}_2(i, j - 1)}{\mathbf{X}_2(i, j) - \mathbf{X}_2(i, j - 1)}, \quad i = 1, 2, \dots, n, \quad j = 2, 3, \dots, m. \quad (7.11d)$$

Note that all of the denominators above equal 1 pixel. We can numerically approximate the displacement gradient at each pixel as

$$\nabla \mathbf{u}(i, j) = \begin{pmatrix} \epsilon_{xx}(i, j) & \epsilon_{xy}(i, j) \\ \epsilon_{yx}(i, j) & \epsilon_{yy}(i, j) \end{pmatrix}, \quad i = 2, 3, \dots, n, \quad j = 2, 3, \dots, m, \quad (7.12)$$

and thus we have an approximation for the deformation gradient at each pixel,

$$\mathbf{F}(i, j) = \begin{pmatrix} \epsilon_{xx}(i, j) & \epsilon_{xy}(i, j) \\ \epsilon_{yx}(i, j) & \epsilon_{yy}(i, j) \end{pmatrix} + \mathbf{I}, \quad i = 2, 3, \dots, n, \quad j = 2, 3, \dots, m. \quad (7.13)$$

At each pixel, we approximate the experimental density, denoted as $\rho_{\text{exp},j}$, from (7.3) with the deformation gradient (7.13) for the j^{th} image in the time-lapse sequence. However, we do not multiply by ρ_0 since ρ_{01} and ρ_{02} are parameters we are trying to optimize. We also do not differentiate between the cell layers since we cannot determine the density of the bottom layer if the top layer is located at the same position from our method. Since the size of the matrix $\rho_{\text{exp},j}$ may not be the same size as the computational grid, we first linearly interpolate the density values at the computational grid nodes. The computational densities $\rho_{\text{comp},1,j}$ and $\rho_{\text{comp},2,j}$ are modified so that if cells from both the top layer and bottom layer are

located at a point, only the top layer density is represented. The square root of the average of the squares of the differences between the experimental and computational densities is

$$P_j = \sqrt{\frac{\sum_{\ell_1=1}^{L_1} \sum_{\ell_2=1}^{L_2} \left((\rho_{\text{comp},1,j} - \rho_{01}\rho_{\text{exp},j})|_{\Omega_1^t \setminus \Omega_2^t} + (\rho_{\text{comp},2,j} - \rho_{02}\rho_{\text{exp},j})|_{\Omega_1^t \cap \Omega_2^t} \right)^2}{L_1 L_2}}, \quad (7.14)$$

where $\rho_{\text{comp},1,j}$, $\rho_{\text{comp},2,j}$, and $\rho_{\text{exp},j}$ are all evaluated at (ℓ_1, ℓ_2) , and the size of the computational grid is $L_2 \times L_1$. Summing over all time points gives

$$z_\rho = \sum_{j=1}^{t_{\text{end}}} P_j. \quad (7.15)$$

To optimize according to both edge position and density, we minimize the value of

$$z = \omega z_d + z_\rho, \quad (7.16)$$

where ω is a weighting factor, usually $\omega = 10^5$. The minimization is done using the MATLAB command `fminsearch`, which uses the simplex search method of Lagarias et al. [37]. A penalty is imposed within the minimization procedure if any of the parameters are negative or if any simulation results in the top layer of cells migrating past the bottom layer.

7.3 RESULTS

In this section, we present preliminary results on fitting the density and cell layer edge positions of model predictions with available data. The data includes time-lapse images of adhering epithelial and mesenchymal cell layers, only the epithelial layer, and only the mesenchymal layer. For single cell layers, we use the two-dimensional single layer model of Arciero et al. [3], and for dual cell layers, we use the two-dimensional dual layer model (Model 3) presented in Chapter 5.

Figures 7.1–7.2 show the predicted edge positions of an epithelial cell layer as a single layer, denoted by solid yellow curves, compared with the experimental edge positions, denoted by dotted cyan curves. The optimal parameters for the epithelial layer by itself are

$$\frac{F}{k} = 0.20413, \quad \frac{k}{b} = 1464.3 \frac{\mu\text{m}^2}{\text{h}}, \quad \rho_0 = 0.0020361 \frac{\text{cells}}{\mu\text{m}^2}, \quad (7.17)$$

which were optimized using the data from Figure 7.1. We expect ρ_0 , the constant density of the initial relaxed (unstressed) cell layer, to be on the order of $0.002 \frac{\text{cells}}{\mu\text{m}^2}$, depending on the stage of development of the cells, so our estimate is physiologically relevant (J. Shawky, D. Vijayraghavan, and L. A. Davidson, unpublished data). The epithelial layer does not spread far on its own.

Figures 7.3–7.4 show the predicted edge positions of a mesenchymal cell layer as a single layer, denoted by solid yellow curves, compared with the experimental edge positions, denoted by dotted cyan curves. The optimal parameters for the epithelial layer by itself are

$$\frac{F}{k} = 0.19031, \quad \frac{k}{b} = 16442 \frac{\mu\text{m}^2}{\text{h}}, \quad \rho_0 = 0.0012202 \frac{\text{cells}}{\mu\text{m}^2}, \quad (7.18)$$

which were optimized using the data from Figure 7.3. Since the cell colony does not move radially outwards overall, our model cannot capture the behavior in the best manner possible which might imply that there may be phenomena we are missing in the single layer model, which was originally developed for epithelial cell sheets. However, it does capture where density is the highest. We expect ρ_0 for the mesenchymal cell layer to be approximately half of ρ_0 for the epithelial cell layer due to the differing sizes of each of the cell types. We also do not expect the stiffness of each layer to be starkly different, so our results imply the force due to lamellipodia formation F is approximately the same for both layers. However, the stretching modulus to adhesion constant ratio $\frac{k}{b}$ is much larger for the mesenchymal cell layer. This likely implies that mesenchymal cell layers, which are not as tightly connected as epithelial cell layers because mesenchymal cells have less adherens junctions, adhere less strongly to the substrate compared to epithelial layers.

Figures 7.5–7.6 show adhering epithelial and mesenchymal cell layers. The predicted edge positions are denoted by solid yellow curves for the mesenchymal layer and solid green curves for the epithelial layer. The experimental edge is denoted by the dotted cyan curves

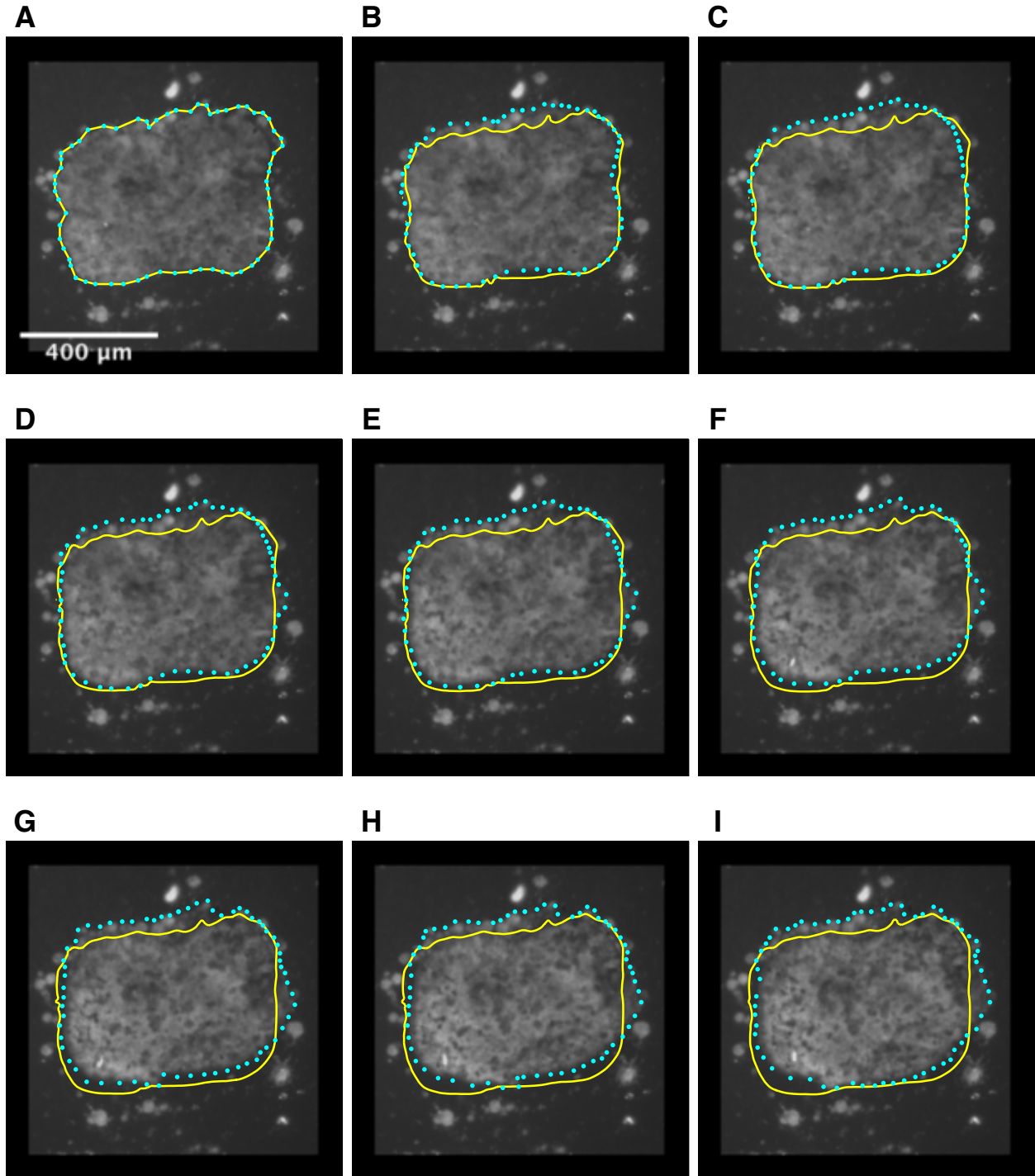


Figure 7.1: Comparison of model predictions with experimental edge: epithelial layer only. The computed edge is represented by the solid yellow curves and the experimental edge is represented by the dotted cyan curves. Optimized parameters are given in (7.17). The images are 275×275 pixels. (A)–(I) The progression of experimental cell migration at 50 minute time intervals using the estimated parameters.

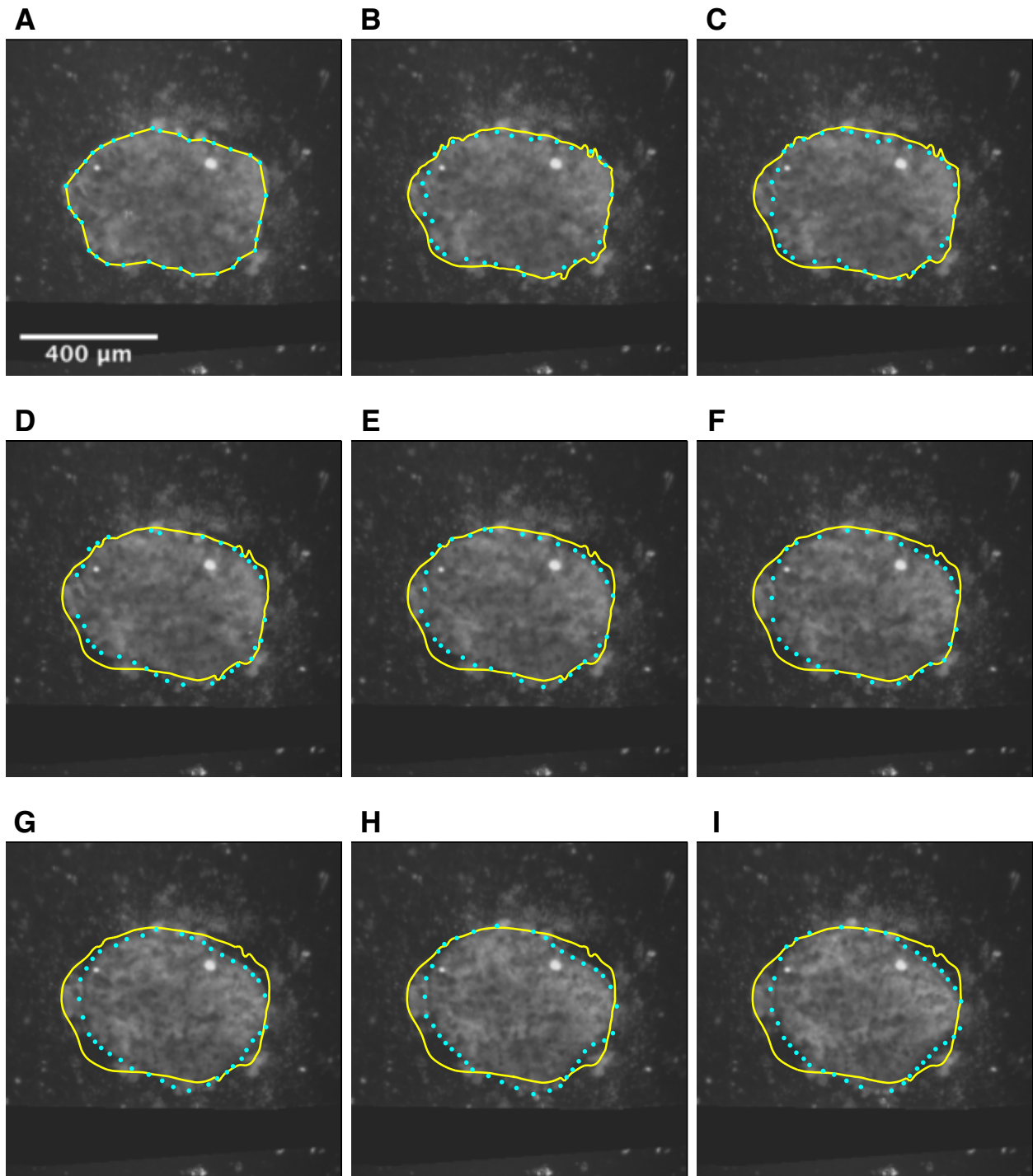


Figure 7.2: Comparison of model predictions with experimental edge: epithelial layer only. The computed edge is represented by the solid yellow curves and the experimental edge is represented by the dotted cyan curves. The parameters used are the ones optimized for Figure 7.1, which are given in (7.17). The images are 275×275 pixels. (A)–(I) The progression of experimental cell migration at 50 minute time intervals using the estimated parameters.

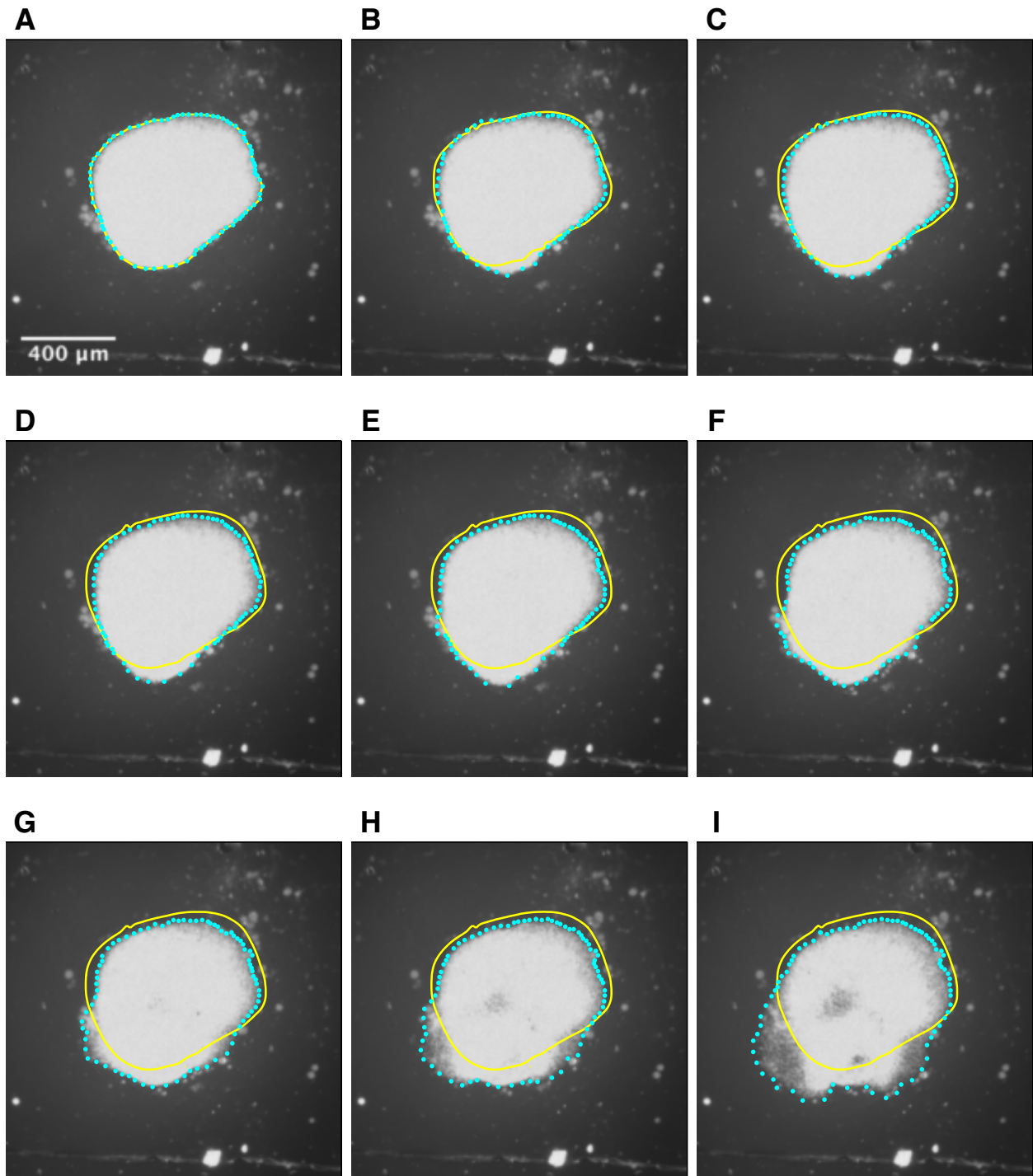


Figure 7.3: Comparison of model predictions with experimental edge: mesenchymal layer only. The computed edge is represented by the solid yellow curves and the experimental edge is represented by the dotted cyan curves. Optimized parameters are given in (7.18). The images are 400×400 pixels. (A)–(I) The progression of experimental cell migration at 50 minute time intervals using the estimated parameters.

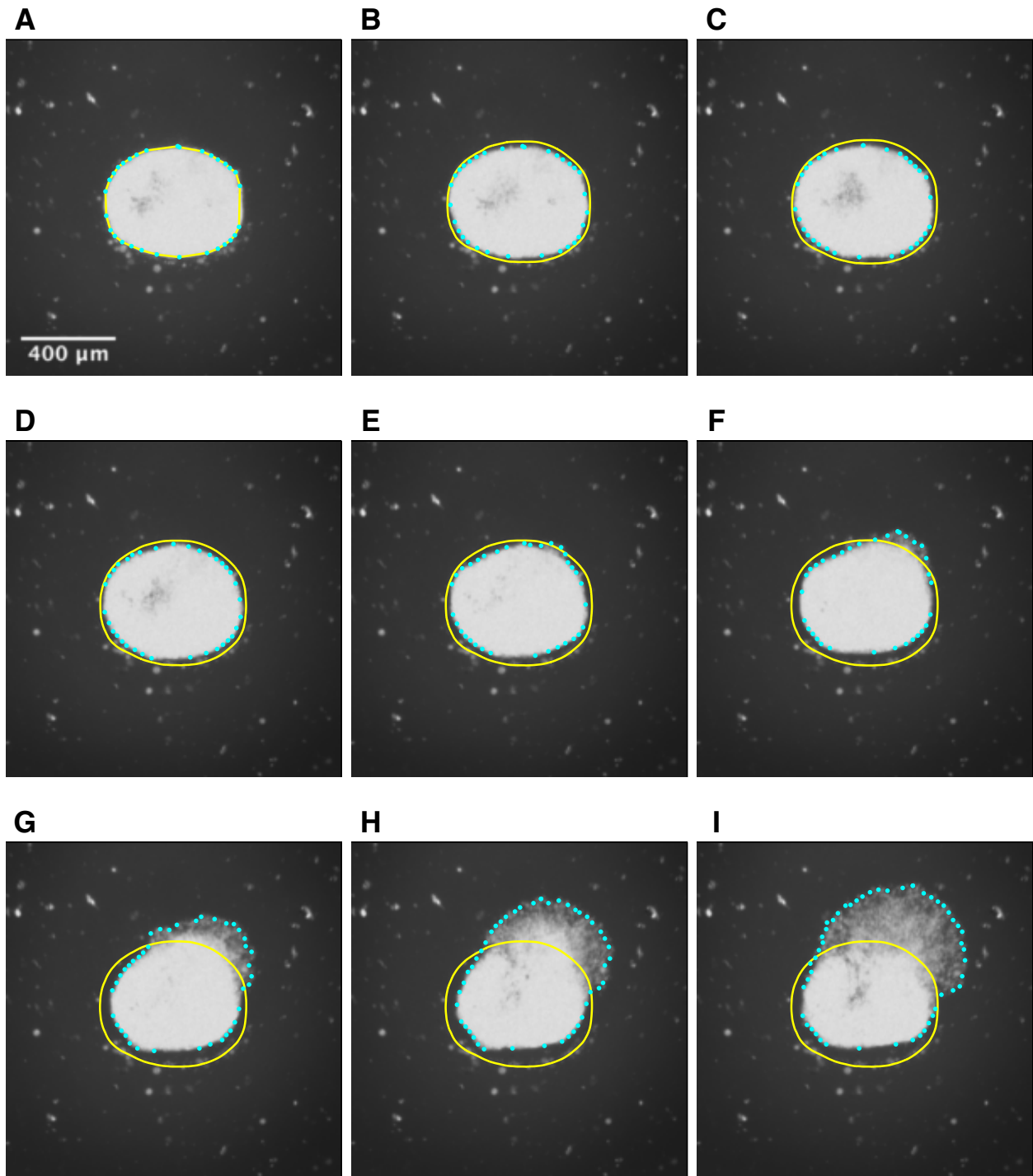


Figure 7.4: Comparison of model predictions with experimental edge: mesenchymal layer only. The computed edge is represented by the solid yellow curves and the experimental edge is represented by the dotted cyan curves. The parameters used are the ones optimized for Figure 7.3, which are given in (7.18). The images are 400×400 pixels. (A)–(I) The progression of experimental cell migration at 50 minute time intervals using the estimated parameters.

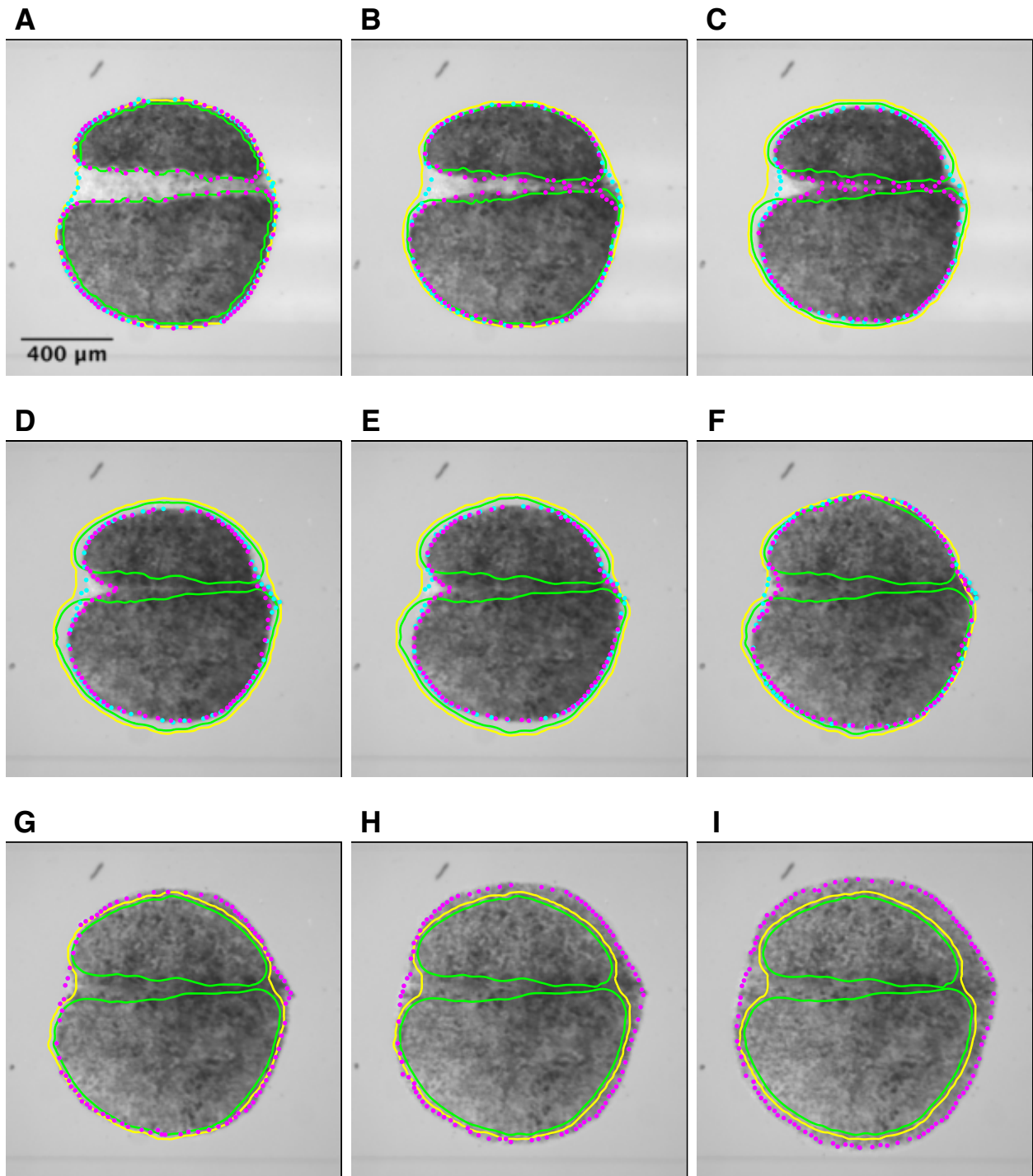


Figure 7.5: Comparison of model predictions with experimental edge: epithelial and mesenchymal layers. The computed edge is represented by the solid yellow curves for the mesenchymal layer and solid green curves for the epithelial layer. The experimental edge is represented by the dotted cyan curves for the mesenchymal layer and dotted magenta curves for the epithelial layer. Optimized parameters are given by (7.19). The images are 800×800 pixels. (A)–(I) The progression of experimental cell migration at 35 minute time intervals using the estimated parameters.

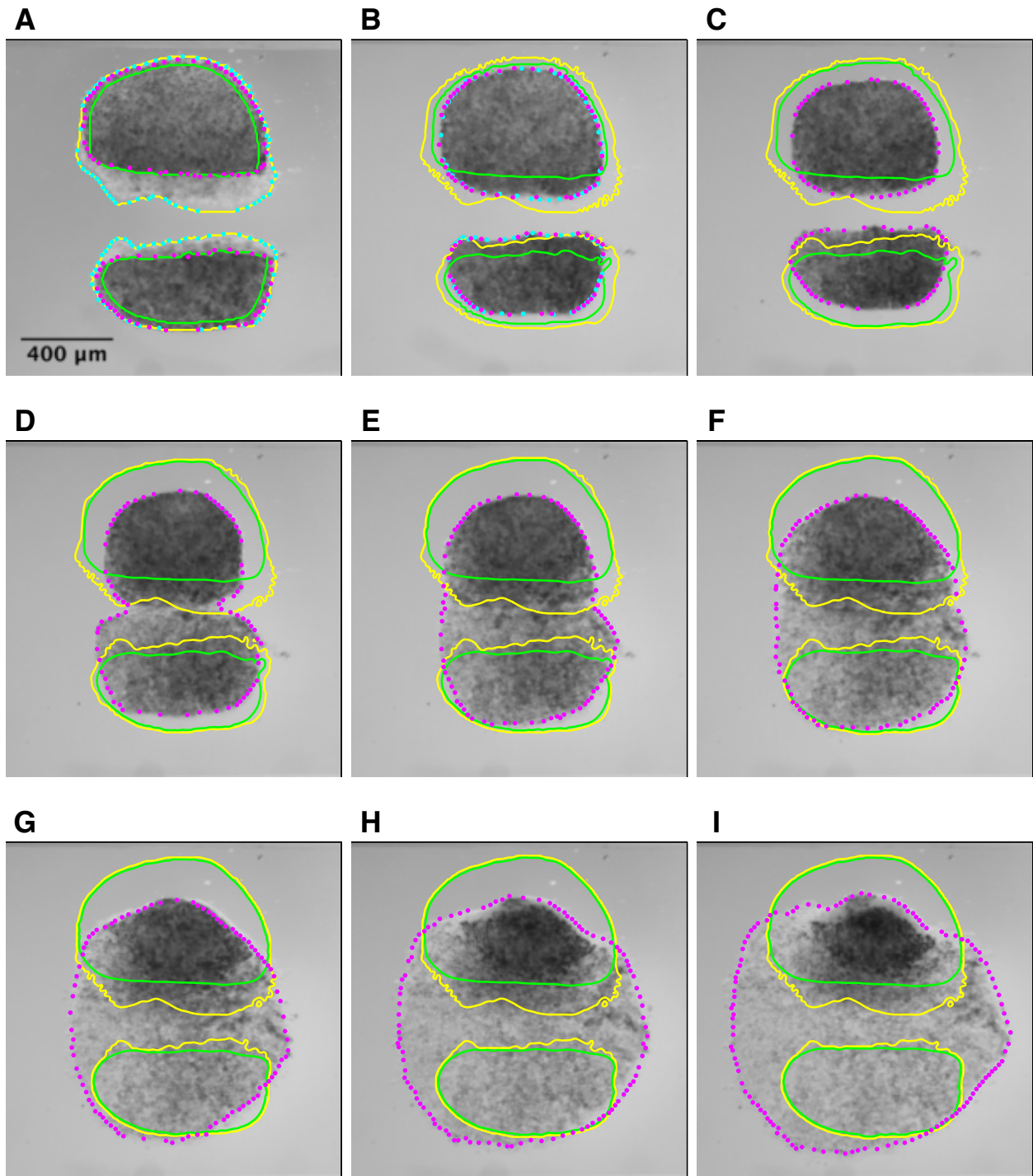


Figure 7.6: Comparison of model predictions with experimental edge: epithelial and mesenchymal layers. The computed edge is represented by the solid yellow curves for the mesenchymal layer and solid green curves for the epithelial layer. The experimental edge is represented by the dotted cyan curves for the mesenchymal layer and dotted magenta curves for the epithelial layer. The parameters used are the ones optimized for Figure 7.5, which are given by (7.19). The images are 800×800 pixels. (A)–(I) The progression of experimental cell migration at 70 minute time intervals using the estimated parameters.

for the mesenchymal layer and dotted magenta curves for the epithelial layer. We set $\rho_{01} = 0.0012202 \frac{\text{cells}}{\mu\text{m}^2}$ (see (7.18)) and $\rho_{02} = 0.0020361 \frac{\text{cells}}{\mu\text{m}^2}$ (see (7.17)) and estimate the remaining parameters. The optimal parameters for the epithelial and mesenchymal layers together are

$$\begin{aligned} \frac{F_1}{k_1} &= 0.0069062, & \frac{F_2}{k_1} &= 1.8098, & \frac{F_2}{k_2} &= 0.017547, \\ \frac{k_1}{b_1} &= 259.44 \frac{\mu\text{m}^2}{\text{h}}, & \frac{k_2}{b_1} &= 202.57 \frac{\mu\text{m}^2}{\text{h}}, & \frac{k_2}{b_2} &= 2296.7 \frac{\mu\text{m}^2}{\text{h}}, \end{aligned} \quad (7.19)$$

which were optimized using the data from Figure 7.5. We see that $\frac{F_1}{k_1}$ is on the order of 10^{-2} times smaller than the optimized $\frac{F}{k}$ for the mesenchymal layer in (7.18) and $\frac{F_2}{k_2}$ is on the order of 10^{-1} times smaller than the optimized $\frac{F}{k}$ for the epithelial layer in (7.17). Further, $\frac{k_1}{b_1}$ is also on the order of 10^{-2} times smaller than the optimized $\frac{k}{b}$ for the mesenchymal layer in (7.18) and $\frac{k_2}{b_2}$ is also on the order of 10^{-1} times smaller than the optimized $\frac{k}{b}$ for the epithelial layer in (7.17).

In Figures 7.5–7.6, the computed edges do not seem to capture the experimental behavior of the cell layers throughout the time-lapse sequences. This likely means that the optimal parameters (7.19) correspond to a local minimum instead of a global minimum or we may be missing features corresponding to adhering epithelial and mesenchymal cell layer migration in our model. To obtain a global minima, we should explore more of the parameter space, keeping in mind that the elapsed CPU time for the parameter estimation procedure (on the same machine as described in Section 6.1.1) is on the order of days.

Since we do not allow the top epithelial layer to migrate ahead of the bottom mesenchymal layer in our numerical code, the points along the initial boundary of the top layer are set slightly inside its actual boundary if they coincide with points along the initial boundary of the bottom layer. This partly explains why the computed edge of the top layer in Figure 7.5 does not capture the merging of the two portions of the epithelial layer very well. One solution to this issue is to refine the mesh so that the difference in the actual initial boundary of the top layer and the initial boundary used in simulations can be minimized, noting that this will cause the elapsed CPU time for the parameter estimation procedure to increase.

Our preliminary study of fitting model predictions with experimental data is promising. Parameter space needs to be further explored to find global minima so that we can perform

a full comparison between the case when the epithelial or mesenchymal cell layer is treated as a single layer and the case when the epithelial and mesenchymal cell layers are adhering together while migrating.

8.0 DISCUSSION

In the first portion of this dissertation, we reviewed the one-dimensional elastic continuum model of cell layer migration of Mi et al. [43] and extended it to include stretch-dependent proliferation, as a cell layer that is stretched may be more likely to reproduce than a compressed, crowded cell layer. The majority of growth functions discussed in this dissertation are physiologically relevant because they indicate proliferation when cells are stretched and decay when cells are compressed while the others are more theoretical in nature. The material formulation is equivalent to the spatial formulation of Arciero et al. [3], which we showed through point-particle interchangeability.

The material formulation with stretch-dependent growth is numerically solved using an adaptive finite difference method, which is much simpler, in terms of the number of lines of programming code and computational expense, than the level set method used to numerically solve the spatial formulation. It is also more reliable than the transverse method of lines method presented, which becomes stiff as the time step tends to 0. The velocity of the leading edge found in numerical simulations of the material formulation was used to determine whether traveling wave solutions might exist for certain cell proliferation rates and cell layer elasticity functions. However, analysis of the existence of traveling wave solutions was more amenable in the spatial formulation. For various nonzero cell proliferation rates and cell layer elasticity functions, we proved that traveling wave solutions with constant wave speed exist in the spatial formulation. The velocity of the leading edge found numerically approximated the analytic wave speed. Stability of the traveling wave was determined numerically; the traveling wave is stable if the corresponding trajectory in phase space does not cross the horizontal ρ -axis. For the model equations in the absence of proliferation, similarity solutions under scaling exist with certain conditions on the constitutive equation for elasticity.

The governing equation of the spatial formulation with logarithmic elasticity function (2.26a) and Fisher growth (2.35b) becomes the classical Fisher-Kolmogorov equation. The typical method of proving the existence of traveling wave solutions for the Fisher-Kolmogorov equation on an infinite domain is to show the existence of a heteroclinic orbit connecting two equilibrium points. The set of admissible traveling wave speeds is bounded below (Murray [45]). Our model includes a Stefan condition on a moving boundary, and the traveling wave solution is solved on a semi-infinite domain instead of on an infinite domain. The necessary phase space trajectory that identifies a traveling wave solution is no longer a heteroclinic orbit, but a portion of an unstable manifold. We find that, in the cases described here, there is either a unique admissible traveling wave speed, a finite number of admissible traveling wave speeds, or a countably infinite number of admissible traveling wave speeds.

For all of our numerical simulations and analysis for the one-dimensional single layer cell migration model, we found that different constitutive functions for the cell proliferation rate and cell layer elasticity do not result in very dissimilar traveling wave speeds. Since choices of cell proliferation rates and cell layer elasticity functions that result in traveling wave solutions more accurately describe the material properties of the cell layer, our studies imply that the inference of material properties from the existence and speed of traveling waves is difficult. Most cell migration experiments tend to calculate the velocity of the wound edge and wound closure time, and we would be able to match this data with various constitutive functions. We suggest that the density of the cell layer should be calculated in future experiments to elucidate which constitutive functions are the most realistic, though we also hypothesize that the fitting of this data will not be starkly different for many constitutive functions. In sum, our approach of analyzing the existence of traveling waves verifies experimental results and models that utilize reaction-diffusion equations by showing that the leading edge of a cell layer gap moves with constant speed. However, more data and further analysis is needed to determine accurate constitutive assumptions for the cell proliferation rate and cell layer elasticity for epithelial sheet migration.

In the second portion of this dissertation, we studied the migration of two adhering cell layers by extending the two-dimensional spatial formulation of Arciero et al. [3]. Each layer is treated as if it were a single layer like in the model of Arciero et al. [3], and the layers are

coupled together through adhesion. We studied only the case when there was an absence of cell proliferation. The resulting system of equations can be separated onto two disjoint domains with an interface condition.

The dual layer model is numerically solved using a level set method for free boundary problems with a domain decomposition method to account for where the migrating cells in each layer are located since extending the material formulation adaptive finite difference method proved to be complicated. The numerical code is flexible for inputting any initial cell layer geometry one desires, while the elapsed central processing unit (CPU) time can greatly vary depending on the model parameters and grid size. The cell layers reached equilibrium if simulations were allowed to run long enough, and studies were performed to compare how different initial geometries, parameters, and grid sizes affected the simulations.

Experimental data of epithelial and mesenchymal cell layer migration during gastrulation from animal cap explants of *Xenopus laevis* embryos was used to estimate model parameters. The data extraction method utilized involves determining the edge positions and density of the cell layers. The density was not directly extracted from experimental time-lapse images but was computed using relations involving the strain, which was directly extracted. Preliminary results showed that the computational edge predictions from simulations with the optimized parameters for single epithelial layers appeared to match the experimental data better than the optimized parameters for single mesenchymal layers. Since the single layer model was developed for epithelial cell sheets, it may be missing features that correctly capture the behavior of mesenchymal cell sheets.

Preliminary results for adhering epithelial and mesenchymal cell layers show that we may also be missing features in our dual layer migration model. Possible model enhancements include treating one or both layers as viscoplastic materials instead of elastic materials or as heterogeneous materials instead of homogeneous materials and incorporating the elasticity of the substrate. Refinement of the mesh and adding constraints on the parameter optimization method will also lead to more accurate optimal parameters.

Our study focused on the mechanical aspects of collective cell migration and the apparent interactions between migrating cells. We used a novel approach to infer material properties from continuum mechanical models based on biomechanical principles by using sophisticated

mathematical analysis, namely traveling wave analysis, to determine a stress-strain relationship and a cell proliferation rate for a single layer of cells. For dual cell layers, specifically adhering epithelial and mesenchymal cell layers, we fit model predictions with experimental strain data, which was innovatively used to calculate the density, and edge position data to find optimal model parameters. Gradually adding complexity to our models, more detailed data, and finding numerical and analytical solutions will continue to aid in our understanding of the mechanisms of collective cell migration.

BIBLIOGRAPHY

- [1] B. ALBERTS, A. JOHNSON, J. LEWIS, M. RAFF, K. ROBERTS, AND P. WALTER, *Molecular Biology of the Cell*, Garland Science, New York, NY, 2008.
- [2] R. J. ANAND, C. L. LEAPHEART, K. P. MOLLEN, AND D. J. HACKAM, *The role of the intestinal barrier in the pathogenesis of necrotizing enterocolitis*, *Shock*, 27 (2007), pp. 124–133.
- [3] J. C. ARCIERO, Q. MI, M. F. BRANCA, D. J. HACKAM, AND D. SWIGON, *Continuum model of collective cell migration in wound healing and colony expansion*, *Biophys. J.*, 100 (2011), pp. 535–543.
- [4] I. ARGANDA-CARRERAS, C. O. S. SORZANO, R. MARABINI, J. M. CARAZO, C. ORTIZ-DE-SOLORZANO, AND J. KYBIC, *Consistent and elastic registration of histological sections using vector-spline regularization*, in *Computer Vision Approaches to Medical Image Analysis*, ser. Lecture Notes in Computer Science, vol. 4241, R. R. Beichel and M. Sonka, eds., Springer Berlin Heidelberg, Germany, 2006, pp. 85–95.
- [5] M. BINDSCHADLER AND J. L. MCGRATH, *Sheet migration by wounded monolayers as an emergent property of single-cell dynamics*, *J. Cell. Sci.*, 120 (2007), pp. 1811–1821.
- [6] E. R. BLOCK, A. R. MATELA, N. SUNDARAJ, E. R. ISZKULA, AND J. K. KLARLUND, *Wounding induces motility in sheets of corneal epithelial cells through loss of spatial constraints: role of heparin-binding epidermal growth factor-like growth factor signaling*, *J. Biol. Chem.*, 279 (2004), pp. 24307–24312.
- [7] T. CALLAGHAN, E. KHAIN, L. M. SANDER, AND R. M. ZIFF, *A stochastic model for wound healing*, *J. Stat. Phys.*, 122 (2006), pp. 909–924.
- [8] E. CANETTA, A. DUPERRAY, A. LEYRAT, AND C. VERDIER, *Measuring cell viscoelastic properties using a force-spectrometer: influence of protein-cytoplasm interactions*, *Biorheology*, 42 (2005), pp. 321–333.
- [9] S. CETIN, J. DUNKLEBARGER, J. LI, P. BOYLE, O. ERGUN, F. QURESHI, H. FORD, J. UPPERMAN, S. WATKINS, AND D. J. HACKAM, *Endotoxin differentially modulates the basolateral and apical sodium/proton exchangers (NHE) in enterocytes*, *Surgery*, 136 (2004), pp. 375–383.

- [10] S. CETIN, H. R. FORD, L. R. SYSKO, C. AGARWAL, J. WANG, M. D. NEAL, C. BATY, G. APODACA, AND D. J. HACKAM, *Endotoxin inhibits intestinal epithelial restitution through activation of Rho-GTPase and increased focal adhesions*, J. Biol. Chem., 279 (2004), pp. 24592–24600.
- [11] S. CHEN, B. MERRIMAN, S. OSHER, AND P. SMEREKA, *A simple level set method for solving Stefan problems*, J. Comput. Phys., 135 (1997), pp. 8–29.
- [12] X. CHEN AND A. FRIEDMAN, *A free boundary problem arising in a model of wound healing*, SIAM J. Math. Anal., 32 (2000), pp. 778–800.
- [13] X. CHEN AND A. FRIEDMAN, *A free boundary problem for an elliptic-hyperbolic system: An application to tumor growth*, SIAM J. Math. Anal., 35 (2003), pp. 974–986.
- [14] P. D. DALE, P. K. MAINI, J. A. SHERRATT, *Mathematical-modeling of corneal epithelial wound healing*, Math. Biosci., 124 (1994), pp. 127–147.
- [15] P. D. DALE, L. OLSEN, P. K. MAINI, J. A. SHERRATT, *Travelling waves in wound healing*, Forma, 100 (1995) pp. 205–222.
- [16] R. FAROOQUI AND G. FENTEANY, *Multiple rows of cells behind an epithelial wound edge extend cryptic lamellipodia to collectively drive cell-sheet movement*, J. Cell Sci., 118 (2005), pp. 51–63.
- [17] J. FENG, O. N. EL-ASSAL, AND G. E. BESNER, *Heparin-binding EGF-like growth factor (HB-EGF) and necrotizing enterocolitis*, Semin. Pediatr. Surg., 14 (2005), pp. 167–174.
- [18] R. A. FISHER, *The wave of advance of advantageous genes*, Ann. Eugenics, 7 (1937), pp. 355–369.
- [19] J. A. FOZARD, H. M. BYRNE, O. E. JENSEN, AND J. R. KING, *Continuum approximations of individual-based models for epithelial monolayers*, Math. Med. Biol., 27 (2009), pp. 39–74.
- [20] P. FRIEDL AND D. GILMOUR, *Collective cell migration in morphogenesis, regeneration, and cancer*, Nat. Rev. Mol. Cell Biol., 10 (2009), pp. 445–457.
- [21] A. FRIEDMAN, *The Stefan problem in several space variables*, Trans. Amer. Math. Soc., 133 (1968), pp. 51–87.
- [22] Y. C. FUNG, *Biomechanics: Mechanical Properties of Living Tissues*, Springer, New York, NY, 1993.
- [23] E. A. GAFFNEY, P. K. MAINI, C. D. MCCAIG, M. ZHAO, AND J. V. FORRESTER, *Modelling corneal epithelial wound closure in the presence of physiological electric fields via a moving boundary formalism*, IMA J. Math. Appl. Med. Biol., 16 (1999), pp. 369–393.

- [24] J. GEISER, *Decomposition Methods for Differential Equations: Theory and Applications*, CRC Press, Boca Raton, FL, 2009.
- [25] M. GHIBAUDO, A. SAEZ, L. TRICHET, A. XAYAPHOUMMINE, J. BROWAEYS, P. SILBERZAN, A. BUGUIN, AND B. LADOUX, *Traction forces and rigidity sensing regulate cell functions*, *Soft Matter*, 4 (2008), pp. 1836–1843.
- [26] J. B. GURDON AND N. HOPWOOD, *The introduction of *Xenopus laevis* into developmental biology: of empire, pregnancy testing and ribosomal genes*, *Int. J. Dev. Biol.*, 44, (2000), pp. 43–50.
- [27] C. A. HALL AND T. A. PORSCHING, *Numerical Analysis of Partial Differential Equations*, Prentice Hall, Englewood Cliffs, NJ, 1990.
- [28] E. HANZAWA, *Classical solutions of the Stefan problem*, *Tohoku Math.*, 33 (1981), pp. 297–335.
- [29] M. C. W. HENRY AND R. L. MOSS, *Necrotizing enterocolitis*, *Annu. Rev. Med.*, 60 (2009), pp. 111–124.
- [30] M. HERON, D. L. HOYERT, S. L. MURPHY, J. XU, K. D. KOCHANEK, AND B. TEJADA-VERA, *Deaths: Final Data for 2006*, National Vital Statistics Reports vol. 57 no. 14., National Center for Health Statistics, Hyattsville, MD, 2009.
- [31] O. ILINA AND P. FRIEDL, *Mechanisms of collective cell migration at a glance*, *J. Cell Sci.*, 122 (2009), pp. 3203–3208.
- [32] E. JAVIERRE, F. J. VERMOLEN, C. VUIK, S. VAN DER ZWAAG, *A mathematical analysis of physiological and morphological aspects of wound closure*, *J. Math. Biol.*, 59 (2009), pp. 605–630.
- [33] E. JAVIERRE, C. VUIK, F. J. VERMOLEN, AND A. SEGAL, *A level set method for three dimensional vector Stefan problems: Dissolution of stoichiometric particles in multi-component alloys*, *J. Comput. Phys.*, 224 (2007), pp. 222–240.
- [34] S. L. KAMENOMOSTSKAJA, *On the Stefan problem*, *Mat. Sb.*, 53 (1965), pp. 485–514.
- [35] H. Y. KIM AND L. A. DAVIDSON, *Methods to investigate molecular mechanisms and cellular mechanics responsible for morphogenesis in *Xenopus laevis* embryos*, in *Imaging in Developmental Biology: A Laboratory Manual*, J. Sharpe and R. O. Wong, eds., Cold Spring Laboratory Press, Cold Spring, NY, 2010, pp. 551–568.
- [36] A. KOLMOGOROV, I. PETROVSKIĬ, AND N. PISCOUNOV, *Étude de l'équation de la diffusion avec croissance de la quantité de matière et son application à un problème biologique*, *Moscow Univ. Bull. Math.*, 1 (1937), pp. 1–25.

- [37] J. C. LAGARIAS, J. A. REEDS, M. H. WRIGHT, AND P. E. WRIGHT, *Convergence properties of the Nelder-Mead Simplex Method in low dimensions*, SIAM J Optim., 9 (1998), pp. 112–147.
- [38] D. A. LAUFFENBURGER AND A. F. HORWITZ, *Cell migration: A physically integrated molecular process*, Cell, 84 (1996), pp. 359–369.
- [39] P. K. MAINI, S. MCELWAIN, AND D. LEAVESLEY, *Travelling waves in a wound healing assay*, Appl. Math. Lett., 17 (2004), pp. 575–580.
- [40] P. K. MAINI, S. MCELWAIN, AND D. LEAVESLEY, *Traveling wave model to interpret a wound-healing cell migration assay for human peritoneal mesothelial cells*, Tissue Eng., 10 (2004), pp. 475–482.
- [41] MATHWORKS, *What is the maximum matrix size for each platform?*, (2012, June 13), Retrieved April 13, 2013, from <http://www.mathworks.com/support/solutions/en/data/1-IHYHFZ/>.
- [42] R. M. M. MATTHEIJ, S. W. RIENSTRA, AND J. H. M. TEN THIJE BOONKKAMP, *Partial Differential Equations: Modeling, Analysis, Computation*, SIAM, Philadelphia, PA, 2005.
- [43] Q. MI, D. SWIGON, B. RIVIÈRE, S. CETIN, Y. VODOVOTZ, AND D. J. HACKAM, *One-dimensional elastic continuum model of enterocyte layer migration*, Biophys. J., 93 (2007), pp. 3745–3752.
- [44] A. MOGILNER, *Mathematics of cell motility: have we got its number?*, J. Math. Biol., 58 (2009), pp. 105–134.
- [45] J. D. MURRAY, *Mathematical Biology: I: An Introduction*, Springer, New York, NY, 2002.
- [46] J. D. MURRAY, *Mathematical Biology: II: Spatial Models and Biomedical Applications*, Springer, New York, NY, 2003.
- [47] J. D. MURRAY AND G. F. OSTER, *Cell traction models for generating pattern and form in morphogenesis*, J. Math. Biol., 19 (1984), pp. 265–279.
- [48] O. A. OLEINIK, *On a method of the construction of solutions of the Stefan problem*, Dokl. Acad. Nauk USSR, 135 (1960), pp. 1054–1057.
- [49] S. OSHER AND J. A. SETHIAN, *Fronts propagating with curvature-dependent speed: algorithms based on Hamilton-Jacobi formulations*, J. Comput. Phys., 79 (1988), pp. 12–49.
- [50] G. F. OSTER, J. D. MURRAY, AND A. K. HARRIS *Mechanical aspects of mesenchymal morphogenesis*, J. Embryol. Exp. Morph., 78 (1983), pp. 83–125.

- [51] S. P. PALECEK, J. C. LOFTUS, M. H. GINSBERG, D. A. LAUFFENBURGER, AND A. F. HORWITZ, *Integrin-ligand binding properties govern cell migration speed through cell-substratum adhesiveness*, *Nature*, 385 (1997), pp. 537–540.
- [52] G. J. PETTET, C. P. PLEASE, M. J. TINDALL, AND D. L. S. MCELWAIN, *The migration of cells in multicell tumor spheroids*, *Bull. Math. Biol.*, 63 (2001), pp. 231–257.
- [53] M. POUJADE, E. GRASLAND-MONGRAIN, A. HERTZOG, J. JOUANNEAU, P. CHAVRIER, B. LADOUX, A. BUGUIN, AND P. SILBERZAN, *Collective migration of an epithelial monolayer in response to a model wound*, *Proc. Natl. Acad. Sci. USA*, 104 (2007), pp. 15988–15993.
- [54] A. QUARTERONI, *Numerical Models for Differential Problems*, Springer, New York, NY, 2009.
- [55] F. G. QURESHI, C. LEAPHEART, S. CETIN, J. LI, S. GRISHIN, S. WATKINS, H. R. FORD, AND D. J. HACKAM, *Increased expression and function of integrins in enterocytes by endotoxin impairs epithelial restitution*, *Gastroenterology*, 128 (2005), pp. 1012–1022.
- [56] A. J. RIDLEY, M. A. SCHWARTZ, K. BURRIDGE, R. A. FIRTEL, M. H. GINSBERG, G. BORISY, J. T. PARSONS, AND A. R. HORWITZ, *Cell migration: Integrating signals from front to back*, *Science*, 302 (2003), pp. 1704–1709.
- [57] P. RØRTH, *Collective cell migration*, *Annu. Rev. Cell Dev. Biol.*, 25 (2009), pp. 407–429.
- [58] C. T. RUEDEN AND K. W. ELICEIRI, *Visualization approaches for multidimensional biological image data*, *BioTechniques*, 43 (2007), pp. S31–S36.
- [59] J. SCHINDELIN, I. ARGANDA-CARRERAS, E. FRISE, V. KAYNIG, M. LONGAIR, T. PIETZSCH, S. PREIBISCH, C. RUEDEN, S. SAALFELD, B. SCHMID, J.-Y. TIN-EVEZ, D. J. WHITE, V. HARTENSTEIN, K. ELICEIRI, P. TOMANCAK, AND A. CARDONA, *Fiji: an open-source platform for biological-image analysis*, *Nat. Methods* 9 (2012), pp. 676–682.
- [60] C. A. SCHNEIDER, W. S. RASBAND, K. W. ELICEIRI, *NIH Image to ImageJ: 25 years of image analysis*, *Nat. Methods*, 9 (2012), pp. 671–675.
- [61] X. SERRA-PICAMAL, V. CONTE, R. VINCENT, E. ANON, D. T. TAMBE, E. BAZEL-LIERES, J. P. BUTLER, J. J. FREDBERG, AND X. TREPAT, *Mechanical waves during tissue expansion*, *Nat. Phys.*, 8 (2012), pp. 628–634.
- [62] H. SHEARDOWN AND Y.L. CHENG, *Mechanisms of corneal epithelial wound healing*, *Chem. Eng. Sci.*, 51 (1996), pp. 4517–4529.

- [63] M. P. SHEETZ, D. P. FELSENFELD, AND C. G. GALBRAITH, *Cell migration: regulation of force on extracellular matrix-integrin complexes*, Trends Cell Biol., 8 (1998), pp. 51–54.
- [64] J. A. SHERRATT, *Actin aggregation and embryonic epidermal wound healing*, J. Math. Biol., 31 (1993), pp. 703–716.
- [65] J. A. SHERRATT, AND J. D. MURRAY, *Models of epidermal wound healing*, Proc. Biol. Sci., 241 (1990), pp. 29–36.
- [66] J. A. SHERRATT, AND J. D. MURRAY, *Mathematical analysis of a basic model for epidermal wound healing*, J. Math. Biol., 31 (1991), pp. 703–716.
- [67] H. L. SIVE, R. M. GRAINGER, AND R. M. HARLAND, *Early Development of Xenopus laevis: A Laboratory Manual*, Cold Spring Harbor Laboratory Press, Cold Spring Harbor, NY, 2000.
- [68] M. A. STOLARSKA, Y. KIM, AND H. G. OTHMER, *Multi-scale models of cell and tissue dynamics*, Phil. Trans. R. Soc. A, 367 (2009), pp. 3525–2553.
- [69] N. STURMAN, N. AMODAJ, AND R. D. VALE, *Micro-Manager: Open Source software for light microscope imaging*, Microscopy Today, 15 (2007) pp. 42–43.
- [70] M. SUSSMAN, P. SMEREKA, AND S. OSHER, *A level set approach for computing solutions to incompressible two-phase flow*, J. Comput. Phys., 114 (1994), pp. 146–159.
- [71] R. T. TRANQUILLO AND J. D. MURRAY, *Continuum model of fibroblast-driven wound contraction: inflammation-mediation*, J. Theor. Biol., 158 (1992), pp. 135–172.
- [72] R. T. TRANQUILLO AND J. D. MURRAY, *Mechanistic model of wound contraction*, J. Surg. Res., 55 (1993), pp. 233–247.
- [73] A. TREMEL, A. CAI, N. TIRTAATMADJA, B. D. HUGHES, G. W. STEVENS, K. A. LANDMAN, AND A. J. O’CONNOR, *Cell migration and proliferation during monolayer formation and wound healing*, Chem. Eng. Sci., 64 (2009), pp. 247–253.
- [74] X. TREPAT, M. R. WASSERMAN, T. E. ANGELINI, E. MILLET, D. A. WEITZ, J. P. BUTLER, AND J. J. FREDBERG, *Physical forces during collective cell migration*, Nat. Phys., 5 (2009), pp. 426–430.
- [75] J. P. TRINKAUS, *Cells Into Organs: The Forces That Shape The Embryo*, Prentice-Hall, Englewood Cliffs, NJ, 1984.
- [76] A. TOSELLI AND O. B. WIDLUND, *Domain Decomposition Methods – Algorithms and Theory*, Springer, New York, NY, 2000.
- [77] P. J. VAN HAASTERT AND P. N. DEVREOTES, *Chemotaxis: signalling the way forward*, Nat. Rev. Mol. Cell Biol., 5 (2004), pp. 626–634.

- [78] P. VITORINO AND T. MEYER, *Modular control of endothelial sheet migration*, *Genes Dev.*, 22 (2008), pp. 3268–3281.
- [79] M. VON DASSOW AND L. A. DAVIDSON, *Physics and the canalization of morphogenesis: a grand challenge in organismal biology*, *Phys. Biol.*, 8 (2011), 045002.
- [80] H. J. WEARING AND J. A. SHERRATT, *Keratinocyte growth factor signalling: a mathematical model of dermal-epidermal interaction in epidermal wound healing*, *Math. Biosci.*, 165 (2000), pp. 41–62.
- [81] G. F. WEBER, M. A. BJERKE, AND D. W. DESIMONE, *A mechanoresponsive cadherin-keratin complex directs polarized protrusive behavior and collective cell migration*, *Dev. Cell*, 22 (2012), pp. 104–115.
- [82] C. XUE, A. FRIEDMAN, AND C. K. SEN, *A mathematical model of ischemic cutaneous wounds*, *Proc. Natl. Acad. Sci. USA*, 106 (2009), pp. 16782–16787.